

AD-A162 032

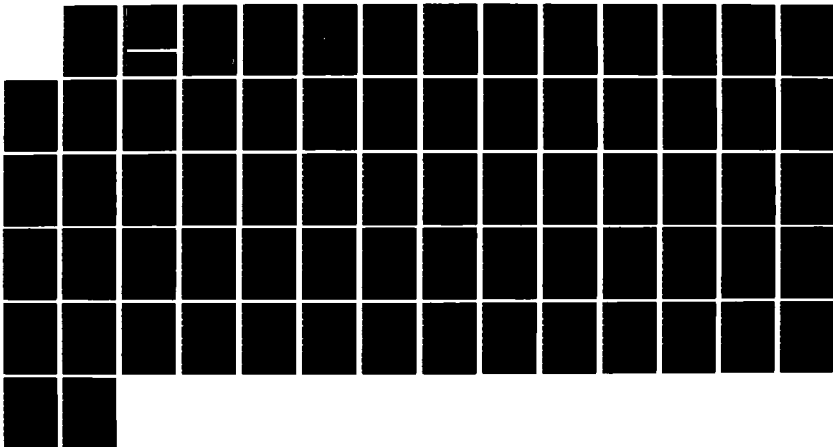
EXPERIMENTAL AND THEORETICAL STUDIES OF RADIATIVE AND
NONRADIATIVE PROCESSES IN SEMICONDUCTORS(U) CALIFORNIA
INST OF TECH PASADENA T C MCGILL 1984 N00014-81-K-0305

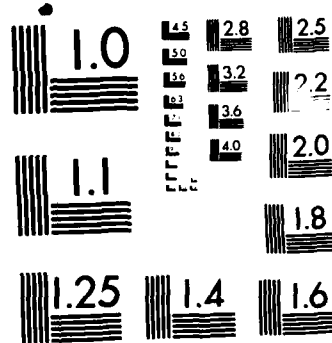
1/1

UNCLASSIFIED

F/G 20/12

NL





MICROCOPY RESOLUTION TEST CHART
NATIONAL BUREAU OF STANDARDS-1963-A

AD-A162 032

FINAL REPORT

TO

DEPARTMENT OF NAVAL RESEARCH

CALIFORNIA INSTITUTE OF TECHNOLOGY

PASADENA, CALIFORNIA

DTIC FILE COPY

This document has been approved
for public release and sale; its
distribution is unlimited.

A
DTIC
ELECTE
S DEC 05 1985 D
E

85 10 18 036

FINAL REPORT

TO

DEPARTMENT OF NAVAL RESEARCH

CONTRACT NO: N00014-81-K-0305

Date: 02/01/81 - 07/31/84

Title: "EXPERIMENTAL AND THEORETICAL STUDIES
OF RADIATIVE AND NONRADIATIVE PROCESSES
IN SEMICONDUCTORS"

This document has been approved
for public release and sale; its
distribution is unlimited.

SUBMITTED

BY

T. C. McGill

California Institute of Technology

Pasadena, California 91125


DTIC
ELECTE
S DEC 05 1985 D
E

ABSTRACT

The study of impurities and defect levels in semiconductors is of major scientific and technological interest. In many cases, the phenomena associated, particularly with deep levels, are not well understood even in this day. In the programs supported under this contract, a number of major contributions were made in this broad area of research. We developed a new form of spectroscopy which allows one to explore some of the excited states of various centers. We were the first to identify and study in detail a change in the structure of a defect due to a radiation with a laser, the so-called non-radiative induced defect reaction process. We studied the properties of some very interesting deep levels in silicon and, in particular, attempted to develop an understanding of the origin of these deep levels which are thought to be associated with clusters of one of the classic shallow acceptors and iron. We developed a new theory of the undulation spectra that occurs in them and donor acceptor pair luminescence. Finally, we developed a theory of the vibrational properties of

7

defects in semiconductors and applied it to the study of oxygen and gallium phosphide, one of the better known systems and the one studied in our experiments on defect reactions.

Accession For	
NTIS	<input checked="" type="checkbox"/>
DTIC TAB	<input type="checkbox"/>
Unannounced	<input type="checkbox"/>
Justification	<i>per</i>
<i>etc</i>	
By	
Distribution/	
Availability Codes	
Dist	Avail and/or Special
<i>A-1</i>	

1. INTRODUCTION

One of the key theoretical and experimental problems in modern semiconductor physics is the identification and description of the properties of deep levels. Deep levels are typically associated with chemical or structural defects which may be inadvertently introduced into a perfect crystal during growth or processing. Many of the unsolved problems in semiconductor technology revolve around our ability to identify and control these dopants.

In the program we made a number of major contributions in a generic sense to this subject.

II. MAJOR RESULTS

We developed a new form of spectroscopy called selective excitation spectroscopy in which one uses a dye laser system to selectively pump the semiconductor below band gap and then detect the radiation emitted by the semiconductor. This

spectroscopic technique allows one to selectively pump one or more of the defect levels in the semiconductor and, hence, obtain a very sensitive determination of their properties. This new technique is described in detail in publications number 1 and 2. (The references for these publications are contained at the end of this report, and an appendix to the report includes a copy of the manuscript.)

One of the major problems in electro-optical devices is the degradation of the light output during the operation of the device due to changes in the defect structure in the semiconductor which have been induced by the presence of electrons and holes. While this process has been speculated as being the origin of a number of degradation mechanisms for lasers and light emitting diodes, no detailed basic scientific study has been carried out in the past to show that such a process can actually occur for a well-known center and an attempt to identify its mechanism. In a series of papers, see publications numbers 3 and 4, we carried out the first study of such a defect reaction. We chose to study the well-known center and GaP associated with $(\text{Zn},0)$ pairs. This center has been extensively studied in the past and, hence, is a likely candidate for

analysis for this kind of phenomena. By pumping the luminescence from this system and studying the changes and the line shape we were able to show that defect reactions did in fact occur.

Nearest-neighbor (Zn,O) pairs were found to be broken up by the pumping of the above-band-gap radiation. To our knowledge, this is the first such clear indication that defect reactions could in fact occur.

One of the more interesting topics in modern semiconductor defectology is the question of whether defects and clusters together can be broken up in various processes, such as the one described above. One of the centers that has attracted a great deal of interest recently is one originally observed at Caltech, which occurs in indium doped silicon samples and is thought to be due to the presence of indium complexed with iron. As part of this program, we carried out a study of the role of iron in the formation of these clusters and silicon doped with indium and silicon doped with thallium. We found that the introduction of iron led to the formation of the cluster defect that was responsible for the luminescence, and, hence, gave the first clear indication that these centers actually involved iron. The results of this study are

reported in publication number 5. Two other projects included the first theoretical explanation of undulation spectra that did not involve in detail calculations of the crystal structure. We showed that periodicities in the luminescence spectra would result from a simple mathematical argument that is applicable any time you have a periodic structure. This is reported in publication number 6. We also studied the properties of the photoluminescence from Si-rich SiGe alloys to try to track the deep levels occurring in this system. The result of this study is published in publication number 7.

Finally, we developed a new vibrational theory of oxygen in GaP. Green's function techniques were used to calculate the local mode properties of this important defect center. After careful calculation, we were able to identify many of the modes that appeared in the luminescence experiments that we carried out. The details of these modes assisted us in our understanding of the defect reaction for zinc oxygen pairs in GaP which are the results of highly heating some of the local modes of this center. The results of this study are reported in publications number 8 and 9.

In summary, this program was a very successful one

in treating some of the important theoretical and
experimental problems associated with deep levels.

III. PERSONNEL SUPPORTED UNDER THIS PROGRAM

The financial support provided by this contract supported the research activity of Professor T. C. McGill. During this period two postdoctoral fellows were supported in part under this program, plus, partial financial support was provided for six graduate students.

Postdoctoral Fellows

C. Mailhiot	Xerox Research Ctr. Rochester, NY
-------------	--------------------------------------

G. Mitchard	Benson Printers Palo Alto, Calif
-------------	-------------------------------------

Graduate Students

R. Feenstra	Member Technical Staff IBM T. J. Watson
-------------	--

Research Center

A. Hunter

Member Technical Staff
Hughes Research Lab

R. Hauenstein

Graduate Student
Caltech

S. Hetzler

Graduate Student
Caltech

T. Schlesinger

Assistant Professor of
Electrical Engineering
Carnegie-Mellon Univ.

G. Wu

Graduate Student
Caltech

IV. PUBLICATIONS SUPPORTED BY THIS CONTRACT

1. A. T. Hunter and T. C. McGill, "Selective excitation luminescence in bulk-grown GaAs", Appl. Phys. Lett. 40, 169(1982).
2. S. R. Hetzler and T. C. McGill, "Selective excitation luminescence and electronic Raman scattering study of the 78-meV acceptor in GaAs", Appl. Phys. Lett. 44, 793(1984).
3. R. M. Feenstra and T. C. McGill, "Defect Reactions in GaP:(Zn,0)", Phys. Rev. Lett. 47, 13(1981).
4. R. M. Feenstra and T. C. McGill, "Reaction kinetics in GaP:(Zn,0)", Phys. Rev. B25, 10(1982).
5. T. E. Schlesinger and T. C. McGill, "Role of Fe in new luminescence lines in Si:Ti and Si:In", Phys. Rev. B25, 12(1982).
6. R. M. Feenstra and T. C. McGill, "Periodicity

in the undulation spectra of GaP:N", Phys. Rev. B26, 1(1982).

7. G. S. Mitchard and T. C. McGill,
"Photoluminescence of Si-rich Si-Ge alloys",
Phys. Rev. B25, 8(1982).
8. R. M. Feenstra, R. J. Hauenstein, and T.C.
McGill, "Vibrational modes of oxygen in GaP
including nearest-Neighbor interactions", Phys.
Rev. B28, 10(1983).
9. R. J. Hauenstein and T. C. McGill, "Vibrational
modes of oxygen in GaP including
second-nearest-neighbor interactions", Phys.
Rev. B29, 4(1984).

Selective excitation luminescence in bulk-grown GaAs

A. T. Hunter and T. C. McGill

California Institute of Technology, Pasadena, California 91125

(Received 6 July 1981; accepted for publication 2 October 1981)

We have measured the excited state levels of two different shallow acceptors in bulk-grown GaAs, using selective excitation luminescence. The $1S-2S$ energy differences were measured to be 21.5 and 18.5 meV, respectively. By comparing these values to those measured by two-hole transition luminescence in high quality epitaxial GaAs [Ashen *et al.*, J. Phys. Chem. Solids 36, 1041 (1975)], the acceptors were identified as Zn and C. The measured $1S-2P$ energy differences also support the identification. These studies demonstrate that selective excitation luminescence can be used to identify shallow acceptors in bulk-grown semi-insulating GaAs, and hence can be used as a diagnostic tool for bulk-grown samples.

PACS numbers: 78.55.Ds, 71.55.Fr, 78.60. — b

The identification of shallow acceptors in GaAs by the use of straightforward photoluminescence is fairly well advanced for high quality epitaxial samples.¹ However, there are additional problems in bulk-grown GaAs such as high defect concentrations and low luminescence intensity that limit the usefulness of these methods. Selective excitation luminescence,²⁻⁵ in which a tunable, below band-gap laser is used to selectively excite the shallow impurities of interest, seems to overcome the problems in identifying these impurities in bulk-grown GaAs. This technique has been used successfully in bulk-grown InP,^{2,3} and also has been used in ZnTe (Ref. 2) and ZnSe.^{4,5}

In this letter, we report for the first time results for GaAs. We were able to conclusively identify the principal acceptor in two bulk-grown samples, neither of which were intentionally doped with shallow acceptors. Both samples studied were grown by the liquid encapsulated Czochralski method.⁶ Sample 1 was chrome doped, and is semi-insulating.⁶ Sample 2 was not intentionally doped, and is p type with $N_A - N_D \sim 10^{16} \text{ cm}^{-3}$.⁶ We have identified the accep-

tor as Zn for the first sample, and C for the second, as will be shown below.

The experiment is essentially that used for ZnSe in Refs. 4 and 5. A tunable laser is used to create an electron on a donor and a hole on an adjacent acceptor, with the hole in an excited state. In principle, pairs should be created with donor electrons in excited states as well, but lines due to this process are not observed. The first excited state of the donor is only ~ 1.5 meV from the band edge, and these weakly bound states may be thermally ionized with high probability. Also, the very extended wavefunction of the excited donor may be substantially broadened by interaction with other defects. This could lead to a line breadth which is too wide to resolve against background luminescence. The energy required to create the pair with an excited hole is $\hbar\omega_{\text{laser}} = E_g - E_A^* - E_D + e^2/\epsilon R + J^*(R)$, where E_g is the band gap, E_A^* the energy of the excited hole with respect to the valence band, E_D the energy of the electron with respect to the conduction band, $e^2/\epsilon R$ is the Coulomb attraction of the ionized centers at distance R from one another, and $J^*(R)$ represents the interaction of the donor and excited acceptor wave functions. This is illustrated in Fig. 1, where the energy of the occupied pair is plotted against the inverse of the pair separation with $J^*(R)$ taken to be zero. The laser will create pairs with the hole in the first excited state at pair separation R_1 , and holes in the second excited state at separation R_2 . The holes very quickly relax to their respective ground state, then recombine with the electrons, emitting light at $\hbar\omega = E_g - E_A - E_D + e^2/\epsilon R + J(R)$, where E_A is now the energy of the ground state of the hole with respect to the valence band, and $J(R)$ is the interaction between the donor and the ground state acceptor wave function. The energy difference between the laser and emitted light consists of two terms in this experiment: $\Delta E = (E_A - E_A^*) + [J^*(R) - J(R)]$. Both $J(R)$ and $J^*(R)$ go to zero for sufficiently separated pairs, and in this limit ΔE is just the difference between the ground and excited state energy of the acceptor wave functions.

The equipment and experimental procedure used are as follows. A Coherent CR-3000K ion laser was used to pump a Coherent model 590 dye laser, with a carbo-cyanine dye. The dye laser was tuned with a 3-plate birefringent filter

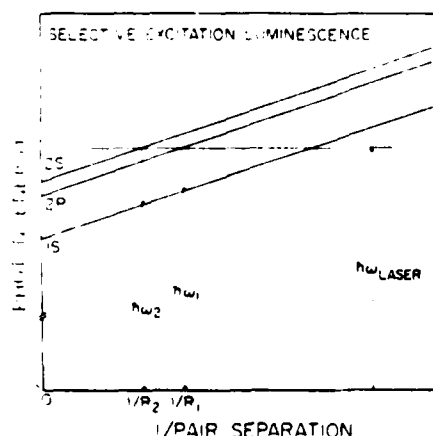


FIG. 1. Schematic of the selective excitation luminescence process.^{2,4} Energy required to create a donor-acceptor pair is plotted against the inverse to the pair separation. The dye laser creates pairs with the hole in an excited state. The hole quickly relaxes to the $1S$ ground state, then radiatively recombines with the electron. The difference between the energy of the laser and that of the emitted light provides the ground-state-excited state energy difference.

placed in the dye-laser cavity. This tuning element allowed linewidths of between 0.1 and 0.2 meV, which allowed energy resolution of better than 0.1 meV in most cases, because the line shapes were symmetric Gaussians, the peaks of which could be determined with high accuracy. The wavelength of light used for the experiments was such that the ground-state emission was near the peak of the donor-acceptor band. The laser light was then focused onto a sample, which was immersed in liquid helium pumped below the lambda point in a Janis cryogenic dewar. The emitted light was analyzed by scanning a Spex 1404 double grating spectrometer and detected with a GaAs photomultiplier tube. The gratings used were replica gratings, but ghost and background intensity proved to be insignificant at the wavelength differences of interest in this experiment. Luminescence background was not insignificant, but could be easily distinguished from the scattering processes we wished to observe. This was done by taking additional spectra with the pump laser at slightly different wavelengths. Those features described above shifted in energy with the laser, while background luminescence did not.

Figure 2 shows luminescence spectra for the two bulk-grown GaAs samples used in this study. In the upper spectrum, the signal-to-noise ratio is not large enough to resolve the bound-exciton line. In the bottom spectrum, it can just barely be resolved on an expanded scale at 1512 meV. The two-hole transition^{7,8} of the bound-exciton line (which leaves the remaining hole in an excited state) cannot be resolved at all. In principle, the donor-acceptor pair luminescence bands centered at 1490 meV can be used to identify the acceptor involved in the transition.¹ However, this line has a rather high intrinsic width, as does the free-electron to bound-hole band seen at higher temperatures. It is difficult to differentiate between acceptors with ionization energies that differ by only a few milli-electron volts, especially when the signal-to-noise ratio is as poor as it is in the upper spectrum. Even with sufficiently good signal-to-noise, line shifts due to high impurity concentrations, which are quite possible in bulk-grown material, make identification by the position of the donor-acceptor band questionable.¹

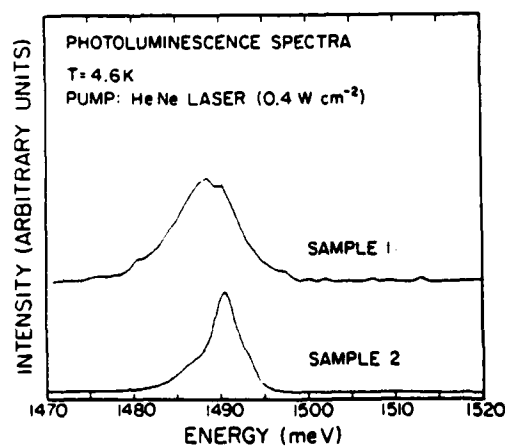


FIG. 2. Photoluminescence spectra for two samples of bulk-grown GaAs, with above band-gap excitation. Intensity of emitted light is plotted on the vertical scale, against photon energy on the horizontal scale.

Selective excitation luminescence data, however, provides an unambiguous identification of the acceptors. The top three spectra in Fig. 3 are from sample 1, each taken with the dye laser at different photon energy. The spectra show intensity of luminescence plotted against energy difference between the laser and luminescence. This means the zero of energy in each case is the laser energy indicated above the spectrum at the right. Four peaks are apparent which remain at an almost constant energy from the laser. The most intense peak is located ~ 21.5 meV below the laser line, and is seen in all three spectra. The line does shift slightly as the energy of the pump laser is changed, which was determined by carefully measuring the energy differences for the spectra shown here, as well as for other spectra. This shift is due to the interaction between the donor and acceptor wave functions described earlier, and causes the energy difference to decrease as the pair separation is decreased. The shift is less than 0.1 meV (which is the uncertainty of the energy separation measurement for this sample) for pump laser energies of 1509.7 meV and smaller. This pump energy creates pairs with approximately 200-Å pair separation. At a pump energy of 1512.6 meV, corresponding to ~ 130 -Å pair separations, the energy shift is 0.5 meV. In addition to this fairly intense peak, three other less intense peaks can be resolved, though not in all the spectra. They occur at 19.2, 21.5, and 25.0 meV. Interpreting the data as was done in Refs. 2 and 3, the principal line is assigned to the $1S-2S$ energy difference, and the less intense lines are assigned to the $1S-2P$ differences.

These results can now be compared to theoretical calculations,⁹ and to measurements made on epitaxial GaAs by other methods. These earlier results, and the results of this study, are tabulated in Table I. The two-hole shift measured for Zn-doped epitaxial samples is 21.8 meV^{1,8} and is very close to the 21.5-meV $1S-2S$ difference measured for sample 1. The position of the less intense peaks line up well with the

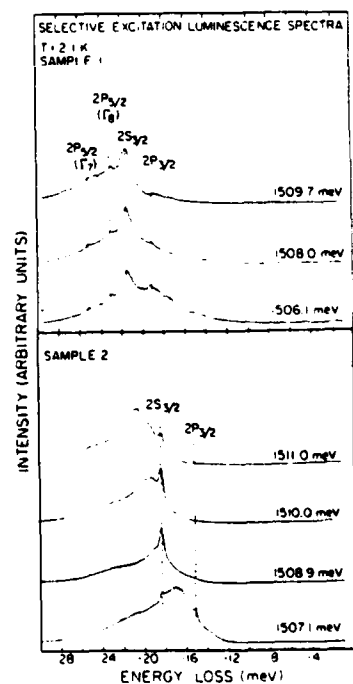


FIG. 3. Selective excitation luminescence spectra for two samples of bulk-grown GaAs. Intensity of emitted light is plotted against the difference in photon energy of emitted light and that of the laser. Photon energy of the laser for each spectrum is given over the spectrum at the right. The top three spectra are for sample 1, the bottom four for sample 2. The labels for the acceptor levels are those used in Ref. 9.

TABLE I. Ground state to excited state splittings for the shallow acceptors C and Zn in GaAs. The labels for the acceptor levels are those used in Ref. 9.

	$1S_{1/2}-2P_{1/2}$ (meV)	$1S_{1/2}-2S_{1/2}$ (meV)	$1S_{1/2}-2P_{3/2}(F_H)$ (meV)	$1S_{1/2}-2P_{3/2}(F_V)$ (meV)
Zn				
Theory ^a	19.3	23.1	23.5	25.4
Photoconductivity ^b	19.4	...	23.2	25.0
"Two-hole" shift ^c	...	21.8
This work	19.2	21.5	23.1	25.0
C				
Theory ^a	14.6	18.4	18.8	20.7
Photoconductivity ^b	15.2	...	19.3	21.3
"Two-hole" shift ^c	...	18.5
This work	15.1	18.5

^aDeduced from theoretical values quoted in Ref. 9 by replacing the calculated $1S$ position (25.7 meV) with that measured in Ref. 1: 26.0 meV for C and 30.7 meV for Zn.

^bMeasured on epitaxial GaAs from Ref. 10.

^cMeasured on epitaxial GaAs from Ref. 1.

$1S-2P$ differences measured using photoconductivity¹⁰ on epitaxial GaAs. Also included in the table, for reference, are the energy differences deduced from the effective mass calculation of Baldereschi and Lipari,⁹ by replacing the calculated $1S$ position with that measured by Ashen *et al.*¹ The matchup between our results and both theory and earlier results indicate that the acceptor in this sample is Zn. It also demonstrates that selective excitation luminescence provides an unambiguous method of determining the identity of shallow acceptors in bulk-grown semi-insulating GaAs.

We have also used this method to identify the acceptor in the second sample as carbon. The bottom half of Fig. 3 shows four spectra taken on this sample, each at a different laser energy. Only two peaks are visible on these spectra, but they are sufficient to identify the acceptor. The principal line in this case is 18.5 meV below the laser energy (and is somewhat narrower than the principal line in sample 1). The 18.5-meV difference is again the energy difference extrapolated to the distant pair limit, which was determined by making the measurement for a wide range of pump energies. The 18.5-meV value is the two-hole shift measured for carbon-doped epitaxial samples,^{1,8} and identifies the dopant in our sample as carbon. The second line, at 15.2 meV, confirms the identification, because this is the $1S-2P_{3/2}$ shift measured for carbon using photoconductivity.¹⁰ These results are also tabulated in Table I.

Two points concerning line breadth and height could use further discussion. The increased linewidth in sample 1 could be indicative of much higher ionized impurity concentration. The electric fields of nearly charged impurities can inhomogeneously broaden the impurity levels through a second-order Stark shift.¹¹ In addition to shifting the impurity energy levels, the Stark effect also mixes S and P wavefunctions. Since the hole must undergo what is apparently a parity forbidden relaxation process² to reach the ground state from a P -like excited state, this mixing would enhance the relaxation from the $2P$ excited states to the $1S$ ground state.

Therefore, both the breadth of the lines and the increased intensity of the $1S-2P$ lines in sample 1 could be explained by a much higher ionized impurity concentration in this sample than in sample 2.

In conclusion, we have measured the excited-state levels of shallow acceptors in bulk-grown GaAs, using selective excitation luminescence. While these levels have been measured in GaAs before, it was done using different methods in high quality, epitaxial layers. This is the first time the levels have been measured in bulk-grown GaAs, where the other methods are not as useful. In doing so, selective excitation luminescence has been shown to be useful in identifying the shallow acceptors in bulk-grown GaAs.

We would like to acknowledge the support from the Office of Naval Research under Contract No. N00014-81-K-0305. The authors also gratefully acknowledge H. Kimura, O. J. Marsh, and H. V. Winston of Hughes Research Laboratories for providing the samples and the results of Hall-effect measurements on the samples.

¹D. J. Ashen, P. J. Dean, D. T. J. Hurle, J. B. Mullin, A. M. White, and P. D. Greene, *J. Phys. Chem. Solids* **36**, 1041 (1975).

²P. J. Dean, D. J. Robbins, and S. G. Bishop, *Solid State Commun.* **32**, 379 (1979).

³P. J. Dean, D. J. Robbins, and S. G. Bishop, *J. Phys. C* **12**, 5567 (1979).

⁴H. Tews and H. Venghaus, *Solid State Commun.* **30**, 219 (1979).

⁵H. Tews, H. Venghaus, and P. J. Dean, *Phys. Rev. B* **19**, 5178 (1979).

⁶H. V. Winston (private communication).

⁷W. Schairer and T. O. Yep, *Solid State Commun.* **9**, 421 (1971).

⁸A. M. White, P. J. Dean, D. J. Ashen, J. B. Mullin, M. Webb, B. Day, and P. D. Greene, *J. Phys. C* **6**, L 243 (1973).

⁹A. Baldereschi and N. O. Lipari, *Phys. Rev. B* **9**, 1525 (1974).

¹⁰R. F. Kirkman, R. A. Stradling, and P. J. Lin-Chung, *J. Phys. C* **11**, 419 (1978).

¹¹D. M. Larsen, *Phys. Rev. B* **8**, 535 (1973).

Selective excitation luminescence and electronic Raman scattering study of the 78-meV acceptor in GaAs

S. R. Hetzler and T. C. McGill

California Institute of Technology, Pasadena, California 91125

A. T. Hunter

California Institute of Technology, Pasadena, California 91125 and Hughes Research Laboratories, Malibu, California 90265

(Received 3 January 1984; accepted for publication 7 February 1984)

We observe for the first time two excited states of the 78-meV acceptor in liquid encapsulated Czochralski GaAs with excitation energies of 62.9 and 66.9 meV above the ground state, respectively. These levels were observed in two different samples using selective excitation luminescence and electronic Raman scattering. We conclude that these levels could correspond to transitions from the $1s^2$ ground state to the split $1s^1 2s^1$ excited state of a double acceptor.

PACS numbers: 71.55.Fr, 78.50.Ge, 78.30.Gt, 78.55.Ds

Recently there has been considerable interest in using semi-insulating GaAs as a substrate for device fabrication. Presently such material is grown undoped by the liquid encapsulated Czochralski (LEC) method. It has been observed that if the melt stoichiometry becomes Ga-rich during the growth process, the material is p type.¹ Such material also possesses an acceptor level at 78 meV above the valence band which is not present in the semi-insulating material.^{2,3} It has been suggested that the center is a double acceptor, with first and second ionization energies of 78 and 200 meV, respectively.⁴⁻⁶ Although some p -like excited states have been observed,³ they do not give a strong indication of the valency of an acceptor since p -like excited states are nearly identical for simple single and double acceptors, as is the case in germanium.⁷ The s -like excited states, however, give a better indication of the valency. In this letter we report the observation of two previously unknown excited states of the 78-meV acceptor using two techniques sensitive to the detection of s -like excited states: selective excitation luminescence and electronic Raman scattering. Our results from both experiments indicate that this level is due to a double acceptor.

Three different LEC samples were used for this study. Samples 1 and 2 were both grown p type from As-deficient melts. Temperature-dependent Hall effect measurements on sample 1 indicated $1.1 \times 10^{15} \text{ cm}^{-3}$ donor, $5.3 \times 10^{15} \text{ cm}^{-3}$ carbon, and $8.1 \times 10^{15} \text{ cm}^{-3}$ 78-meV acceptor concentrations. Sample 2, taken from a crystal similar to sample 1, was neutron transmutation doped and annealed at 580 °C for 1 h. Neutron transmutation doping added $3.8 \times 10^{15} \text{ cm}^{-3}$ Se and Ge donors, plus additional damage related donors. Temperature-dependent Hall effect measurements on an unirradiated sample adjacent to sample 2 given the same anneal gave concentrations of $2.6 \times 10^{15} \text{ cm}^{-3}$ donors, $7.4 \times 10^{15} \text{ cm}^{-3}$ carbon, and $3.6 \times 10^{16} \text{ cm}^{-3}$ 78-meV acceptors. Measurements on the unirradiated samples showed the slope for carbon below 4.2 K, indicating that the 78-meV level was fully occupied.⁸ Temperature-dependent Hall measurements on a sample transmutation doped and annealed in a manner identical to sample 2 showed an 0.07-eV slope however, indicating that the 78-meV acceptor was partially compensated in the transmutation doped and annealed samples.

The 78-meV acceptor was also identified by band-acceptor photoluminescence in samples 1 and 2. Sample 3 was chromium-doped, semi-insulating GaAs, and photoluminescence experiments did not detect the presence of a level at 78 meV in this sample. The setup is nearly identical for both experiments. The below band-gap excitation was provided by a Coherent model 590 tunable dye laser containing a carbocyanine dye, using a Coherent CR3000K krypton ion laser to optically pump the dye. Tuning the dye laser was accomplished via a three-plate quartz birefringent filter. The sample was mounted in a Janis cryogenic dewar and immersed in liquid helium pumped below the lambda point. The luminescence from the sample was analyzed by a Spex 1404 scanning spectrometer, using a cooled S1 photomultiplier as a detector.

The excited states of the 78-meV acceptor were measured using two different techniques: selective excitation luminescence (SEL) and electronic Raman scattering (ERS). The SEL experiment is essentially that which was described in Ref. 9. A below band-gap photon is used to create a donor-acceptor pair by exciting an electron from an ionized acceptor to an ionized donor, leaving the resulting hole on the acceptor in an excited state. The excited hole rapidly relaxes to the acceptor ground state, and eventually recombines with the electron on the donor, emitting a photon. If we ignore any non-Coulombic interaction between the donor and acceptor, the energy difference between the incident and emitted photons is the difference between the ground state and excited state binding energies. Changing the laser energy alters only the separation of the donor and acceptor, enabling us to identify the excited states since they remain at fixed energy separation from the laser. Since this technique requires both the donor and acceptor to be ionized, it is useful for studying compensated material. Occupied acceptors are best studied using ERS. In this experiment a below band-gap photon can create a virtual electron-hole pair. The electron-hole pair can then recombine, raising a hole bound to an acceptor to an excited state and emitting a photon with the remaining energy. The energy difference between the incident and emitted photons is the difference between the ground state and excited state binding energies.

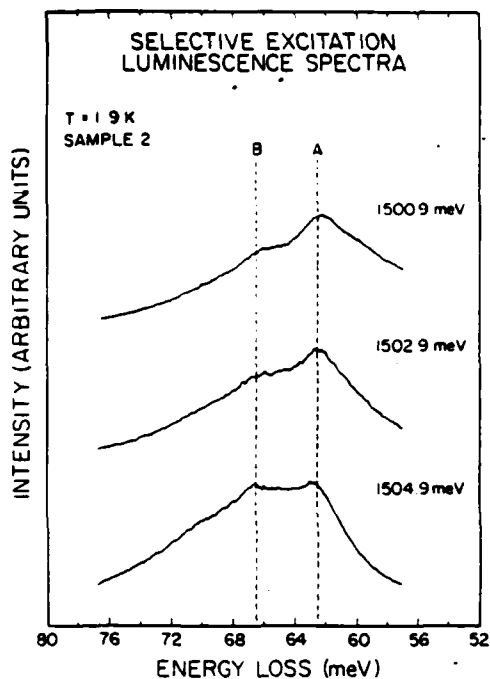


FIG. 1. Selective excitation luminescence spectra from sample 2. Intensity of emitted light is plotted against the difference between the emitted photon energy and that of the laser. Three different laser energies were used to distinguish between SEL features and background processes. The laser photon energy for each spectrum is at the right.

The SEL results for sample 2 for three different exciting laser frequencies are shown in Fig. 1, and the ERS results for sample 1 for two different exciting laser frequencies are shown in Fig. 2. Two transitions are evident in the SEL data, one at 62.5 meV (line A) and one at 66.5 meV (line B). The broad background in the spectra is due to donor-acceptor

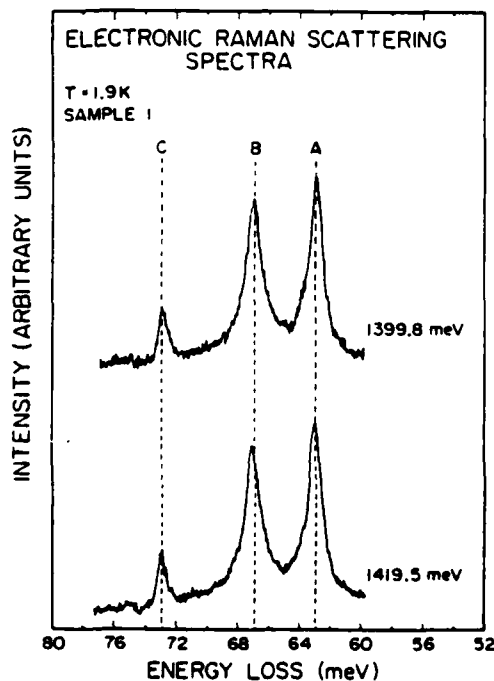


FIG. 2. Electronic Raman scattering spectra from sample 1. Intensity of emitted light is plotted against the difference between the emitted photon energy and that of the laser. Two different laser energies were used to distinguish between ERS features and background processes. The laser photon energy for each spectrum is at the right.

TABLE I. Observed line positions and interpretations.

	A	B	C (meV) ^a	ΔE (meV) ^b
SEL	62.5 meV	66.5 meV	...	4.0
ERS	62.9 meV	66.9 meV	72.9	4.0
Single acceptor ^c	63.4 meV ^d $1S_{1/2} \rightarrow 2S_{1/2}$	66.6 meV $1S_{1/2} \rightarrow 2P_{1/2}$...	3.2
Double acceptor ^e	$1s^2 \rightarrow 1s \ 1'2s^1$ ($1S, 7S$)	$1s^2 \rightarrow 1s \ 1'2s^1$ ($1S, 5S$)	...	2.6

^a We believe that line C is due to Raman scattering from 2 LO (Γ) phonons, and that it is not related to the 78-meV level.

^b Energy separation of lines A and B.

^c Based on work done by Baldereschi and Lipari (Refs. 12 and 13).

^d This estimate is obtained by including the observed central cell shift for the 78-meV acceptor (see Ref. 14).

^e Based on the helium-atom-like approximation discussed in the text.

luminescence. Three peaks are visible in the ERS data: line A at 62.9 meV, line B at 66.9 meV, and line C at 72.9 meV. Lines A and B appear shifted about 0.4 meV toward greater energy loss in the ERS experiment than in SEL. This may be expected since any non-Coulombic interaction between the donor and acceptor wave functions in SEL would tend to shift the measured energy from the actual binding energy. Therefore, the energies obtained in ERS should be more accurate measurements of the excited state energies. Line C was not seen in the SEL experiment. The observed line positions are summarized in Table I.

The two lines A and B show up only in material containing the 78-meV acceptor. Figure 3 compares ERS spectra from sample 1 with spectra from sample 3, which does not contain the 78-meV level. There is no indication of lines A or B in sample 3. This suggests that they are both due to the 78-meV level. Although they lie in the energy region for

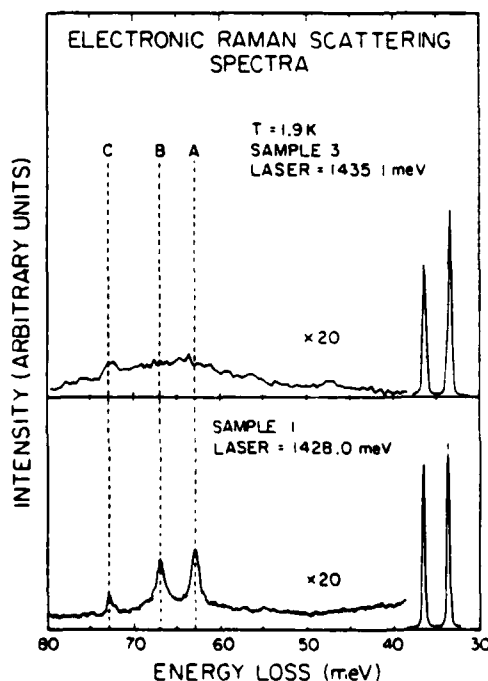


FIG. 3. Electronic Raman scattering spectra from samples 1 and 3. Intensity of emitted light is plotted against the difference between the emitted photon energy and that of the laser. Narrow lines at 36.5 and 33.6 meV are the LO (Γ) and TO (Γ) phonons, respectively.

two-phonon Raman scattering, we can be sure that they are electronic in nature since the excitation intensity in SEL is too low to observe even single-phonon Raman scattering. There is evidence of a line at 73 meV in sample 3, which may correspond to line C seen in sample 1. Since we do not observe line C in the SEL experiment, and it appears to be present in sample 3, we believe that it is due to 2 LO (Γ) phonons (room-temperature Raman scattering measurements give a value of 72.9 meV for this transition¹⁰) and not related to the 78-meV acceptor.

We believe lines A and B are due to the split $1s\ ^12s^1$ (using atomic single particle notation) state of a double acceptor. The s -like excited states of a double acceptor will be split into two levels by the exchange interaction. A simple model of a double acceptor in GaAs can be obtained by analogy to the single acceptor effective mass approximation. We consider the holes to be $j = 3/2$ particles, with mass equal to the heavy hole effective mass, and that the electric fields are screened by the static dielectric constant. For a heliumlike acceptor in this approximation, we obtain two $1s\ ^12s^1$ levels: a tenfold degenerate ($^3S, ^7S$) level (with symmetric spins), and a sixfold degenerate level ($^1S, ^5S$) (with antisymmetric spins). We can scale the energy splitting in helium to GaAs in this model by multiplying the energy in helium by the ratio of the Bohr radii divided by the dielectric constant. The experimentally observed magnitude of the splitting in helium is 0.79 eV,¹¹ which scales to 2.6 meV in GaAs. Including the effects of the crystal field and the spin-orbit interaction with the valence band will not change the splitting to first order, since they will only affect the wave functions used, not the potential. The observed splitting between lines A and B is 4.0 meV, which is in good agreement with the estimate (see Table I).

Another possible interpretation of lines A and B is the following: line A could be the $1S_{3/2} \rightarrow 2S_{3/2}$ transition and line B could be the $1S_{3/2} \rightarrow 2P_{3/2}$ transition of a simple acceptor. Theoretical estimates based on work done by Baldereschi and Lipari,^{12,13} using the observed value of 78 meV for the $1S_{3/2}$ binding energy, yield values for these transitions of 63.4 meV (including the central cell shift¹⁴) and 66.6 meV, respectively. We obtain good agreement between lines A and B and these estimates. However, there is evidence that line B is not due to a p -like final state, but rather an s -like final state. Previous SEL measurements on carbon and zinc in GaAs reveal s -like states with approximately two to five times the intensity of p -like states.⁹ Carbon has also been observed by ERS in GaAs,¹⁵ and the p -like transitions were observed to be at least ten times less intense than the s -like transitions. In the experiments conducted here, the intensities of the A and B lines are nearly identical (see Figs. 1 and 2). Also, neither experiment shows evidence of the p -like excited states seen in IR absorption.³ (In both SEL and ERS, all p -like states are seen with roughly the same intensity.) Finally, IR absorption measurements heavily favor p -like excited states over s -like excited states since the latter are forbidden to first order.

Thus, one would not expect to see s -like states in IR absorption. If line B were actually p -like, it should have been observed in the IR absorption experiment.³ This leads to the conclusion that lines A and B are both s -like.

We also have evidence of a line at 4.8 meV in ERS data from sample 1. This line was not seen in any other samples, and might be related to the 78-meV acceptor. This line is not donor related since the donors are ionized in this sample. This line could correspond to a transition between two levels of a split $1s^2$ ground state. Such splittings have been observed for mercury and zinc in germanium.^{7,16} [The ground state of a double acceptor in the effective mass approximation is sixfold degenerate ($^1S, ^5S$), and can be split by interaction with the valence band.¹⁷]

In conclusion, we have observed two excited states of the 78-meV acceptor in GaAs, at 62.9 and 66.9 meV. We believe that these lines correspond to transitions from the ground state to s -like excited states of this acceptor. It is likely that the excited states involved are the $1s\ ^12s^1$ ($^3S, ^7S$) and $1s\ ^12s^1$ ($^1S, ^5S$) states of a double acceptor. Our results show that SEL and ERS are good techniques for determining the valency of acceptors since they are sensitive to the s -like excited states.

We would like to acknowledge the support from the Office of Naval Research under contract No. N00014-81-K-0305. The authors also gratefully acknowledge M. H. Young of Hughes Research Laboratories for providing the samples used in this study.

¹D. E. Holmes, R. T. Chen, K. R. Elliott, and C. G. Kirkpatrick, *Appl. Phys. Lett.* **40**, 46 (1982).

²P. W. Yu and D. C. Reynolds, *J. Appl. Phys.* **53**, 1263 (1982).

³K. R. Elliott, D. E. Holmes, R. T. Chen, and C. G. Kirkpatrick, *Appl. Phys. Lett.* **40**, 898 (1982).

⁴A. T. Hunter, R. Baron, J. P. Baukus, H. Kimura, M. H. Young, H. Winston, and O. J. Marsh, in *Semi-Insulating III-IV Materials*, Evian 1982, edited by S. Makram-Ebeid and B. Tuck (Shiva, Cheshire, England, 1982), p. 396.

⁵P. W. Yu, W. C. Mitchel, M. C. Mier, S. S. Li, and W. L. Wang, *Appl. Phys. Lett.* **41**, 532 (1982).

⁶K. R. Elliott, *Appl. Phys. Lett.* **42**, 274 (1983).

⁷R. A. Chapman, W. G. Hutchinson, and T. L. Estle, *Phys. Rev. Lett.* **17**, 132 (1966).

⁸A. T. Hunter, M. H. Young, and R. Baron, Hughes Research Laboratories (unpublished).

⁹A. T. Hunter and T. C. McGill, *Appl. Phys. Lett.* **40**, 169 (1982).

¹⁰T. Sekine, K. Uchinokura, and E. Matsuura, *J. Phys. Chem. Solids* **38**, 1091 (1977).

¹¹A. R. Strigono and N. S. Sventitskii, *Tables of Spectral Lines of Neutral and Ionized Atoms*, (IFI/Plenum, New York, 1968), Vol. I, p. 79.

¹²A. Baldereschi and N. O. Lipari, *Phys. Rev. B* **9**, 1525 (1974).

¹³A. Baldereschi and N. O. Lipari, *Phys. Rev. B* **8**, 2697 (1973).

¹⁴The probability of finding the hole at the impurity site has been calculated in Ref. 13. Using the value $\mu = 0.767$ for GaAs given there, the $2S$ state experiences a central cell shift of 0.133 times that of the $1S$ state. Here, that yields a shift of 7.0 meV.

¹⁵A. T. Hunter, Ph. D. thesis, California Institute of Technology, 1981.

¹⁶H. Nakata, T. Yodo, and E. Otsuka, *Solid State Commun.* **45**, 55 (1983).

¹⁷A. P. Silin, *Sov. Phys. Solid State* **13**, 2625 (1972).

Defect Reactions in GaP:(Zn,O)

R. M. Feenstra and T. C. McGill

California Institute of Technology, Pasadena, California 91125

(Received 6 July 1981)

We have observed photoinduced reactions between pairs of zinc and oxygen impurities in gallium phosphide. From photoluminescence studies we find that the nearest-neighbor (Zn, O) pairs are dissociating, after which they re-form as further separated pairs. The activation energy for the dissociation is found to be 0.60 ± 0.07 eV for the photoinduced reaction, and 2.6 ± 0.6 eV for the purely thermal reaction. We tentatively identify the photoinduced reaction as being due to excitation of local phonon modes by nonradiative electron-hole recombination.

PACS numbers: 66.30.Jt, 63.20.Pw, 78.55.Ds

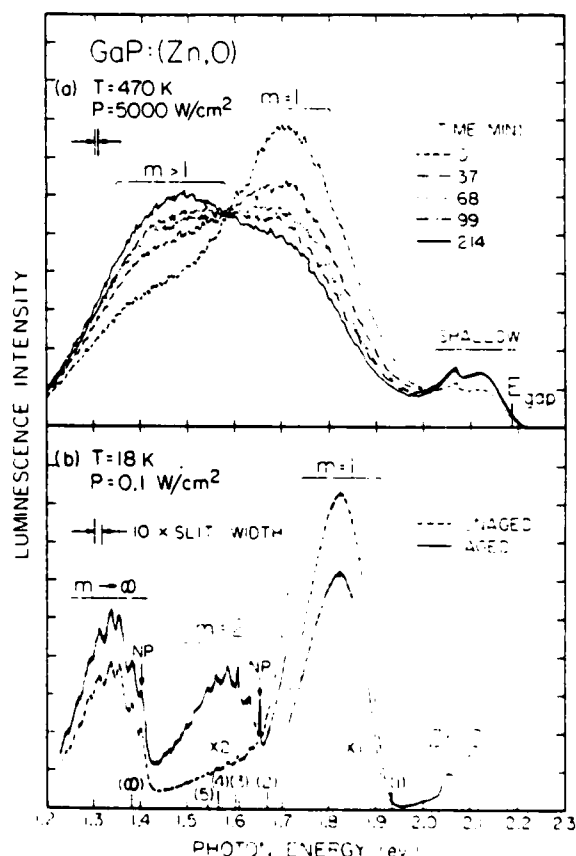
Defect complexes in semiconductors can play a very important role in determining the electrical and optical characteristics of the material. One simple complex which commonly occurs is a pair of donor and acceptor impurities. The energy of the luminescence emitted from donor-acceptor (DA) pairs depends on the separation of the impurities,¹ and so a luminescence spectrum provides information about the number of pairs of each possible separation.

In this work we use photoluminescence to monitor the relative positions of Zn_{Ga} and O_P impurities in GaP. When the GaP is subjected to laser excitation at high temperatures, we observe reactions in which the impurities diffuse through the lattice to occupy new substitutional sites. This is the first time DA luminescence has been used as a microscopic probe of defect reactions. From low-temperature studies we identify these reactions as being the dissociation of nearest-neighbor (Zn, O) pairs and the formation of further separated pairs. Such a dynamic process of reactions among lattice defects of known initial and final chemical type has not previously been observed in a semiconductor. The photoluminescence spectra reported here provide valuable information about those phonon modes which are likely to be responsible for the (Zn, O) dissociation. Most other studies of defect reactions in semiconductors have not included any observations of the vibrational modes of the defect.

The samples used in this work were liquid-phase-epitaxially grown *pn* junctions on *n*-type GaP (single crystal). The growth technique is described by Saul, Armstrong, and Hackett.² The exposed 50- μ m-thick layer of the junction is *p* type, doped with Zn and O. The (substitutional) O concentration is about 10^{18} cm⁻³ and the Zn concentration is about 3×10^{17} cm⁻³ (based on the crystal-growth conditions). Other impurities include N and S. The photoluminescence spectra were obtained using above-band-

gap Ar⁺ laser excitation and a liquid-N₂-cooled S-1 type photomultiplier.

Figure 1 shows several high- and low-temperature photoluminescence spectra. In Fig. 1(a) the



time between successive scans is about 30 min. We see that the spectra are changing with time. This is a direct observation of a reaction in progress. We refer to this reaction as an "aging" process. The initial and final spectra shown are similar to those seen by Dapkus and Henry.³ These authors showed that the aging reaction is due to photoinduced destruction of nearest-neighbor (Zn,O) pairs, and they speculated that these pairs were in fact dissociating and forming further separated pairs. Here, we prove that this speculation is correct.

To identify the luminescence bands we go to the low-temperature spectra shown in Fig. 1(b). From the work of previous authors⁴⁻⁷ we identify the band centered at 1.82 eV as being due to nearest-neighbor pairs (Zn,O)_{m=1}, and the band centered at 1.35 eV as due to far-separated pairs (Zn,O)_{m=∞}. The breadth of these bands is due to phonon-assisted radiative transitions. The (Zn,O) DA luminescence at about 2.05 eV is constant in intensity between the unaged and aged material, which indicates that the low-temperature minority carrier concentration is also constant. Thus, the reduced intensity of the $m=1$ band in the aged material must be due to a reduction of the (Zn,O)₁ concentration.³ Similarly, the (Zn,O)_{m=∞} concentration has increased. Centered at 1.59 eV is a luminescence band which is seen in the aged sample, but barely visible in the unaged material. The breadth of this band is similar to those of (Zn,O)₁ and (Zn,O)_{m=∞} and the resolved phonon structure is characteristic of a complex involving

O. Furthermore, if we compare the no-phonon transition location with theoretical predictions,^{1,8} we see that the position of this new band is as expected for (Zn,O)₂. We thus identify the new luminescence as being due to second-nearest-neighbor (Zn,O)₂ pairs. The reduction in $m=1$ pair concentration has been accompanied by an increase in concentration of $m>1$ pairs. From the observed luminescence intensities, and calculations (following Ref. 9) of the initial distribution of pair separations, we find that the increase in concentration of $m>1$ pairs is roughly equal to the decrease in concentration of $m=1$ pairs. We also note that in Fig. 1(a) the $m>1$ band is increasing at the same rate as the $m=1$ band is decreasing. Thus, we conclude that the nearest-neighbor pairs are dissociating and forming further separated pairs.

In Fig. 2 the discrete DA lines for second nearest neighbor and further separated pairs are resolved. All except the $m=2$ and $m=3$ lines have previously been reported,⁷ although we reidentify a few of the lines as phonon-assisted transitions. Replicas of the $m=2$ line are seen involving phonons of energies 9.2, 21.7, 27.2, and 46.8 meV. The 46.8-meV mode is probably very similar to a bulk optical (O) mode and we have labeled it as such. The lower energy modes are local modes (resonances) of the (Zn,O) complex. These modes form a broad band at ~20 meV from the no-phonon band in the $m=\infty$ DA luminescence [Fig. 1(b)]. Similar localized phonons of energy ~25 meV are seen for the isolated neutral O don-

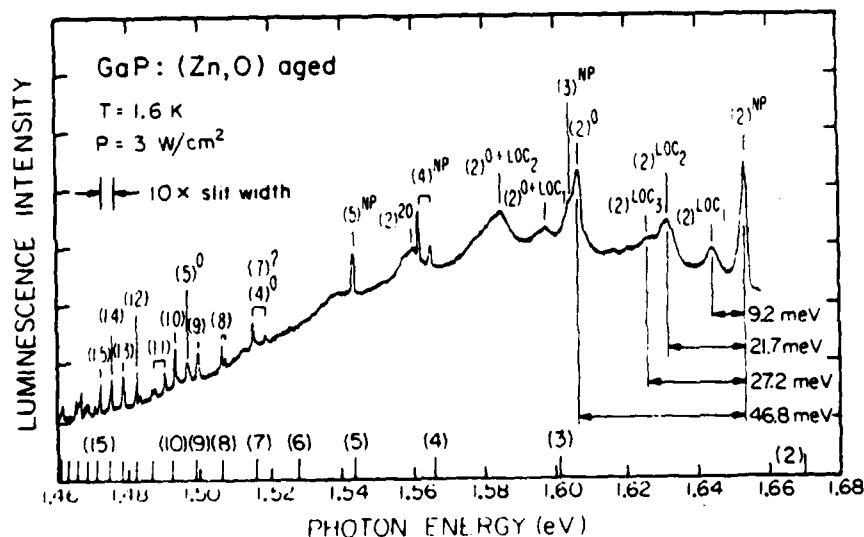


FIG. 2. Low-temperature donor-acceptor pair luminescence. The lines are labeled by (m) for mth-nearest-neighbor pairs with a superscript indicating the type of phonon involved in the transition (O=optical, LOC=local, NP=no-phonon). Those labels with no superscripts refer to no-phonon transitions.

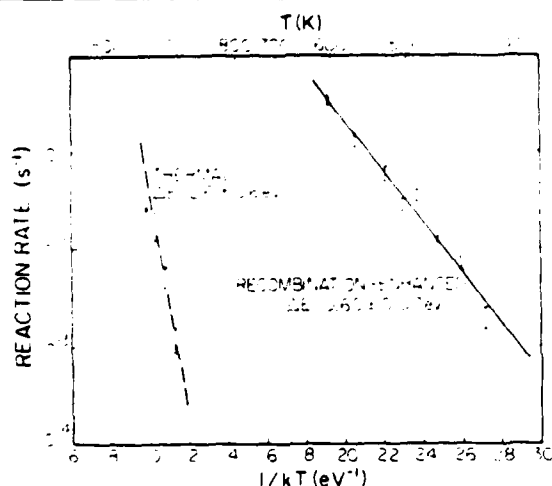


FIG. 3. The dissociation rates of nearest-neighbor (Zn, O) pairs. The rates labeled "recombination-enhanced" are for photoinduced dissociation of the pairs, in the limit of high incident light intensity. The rates labeled "thermal" are for pair dissociation by purely thermal means.

or.¹⁰ For a defect with small mass, a localized low-energy phonon mode implies a reduced spring constant. From the phonons observed here, we estimate that the O-Ga spring constant is about 30% of the P-Ga spring constant. This certainly implies a reduction in the O-Ga bond strength compared to that of P-Ga. A weak O-Ga bond seems reasonable considering the small size and large electronegativity of O compared to P.

The mechanism responsible for the (Zn, O)_i dissociation can be identified by measuring the activation energies for the photoinduced and purely thermal reactions.^{11,12} We have performed these measurements and a complete account of them will be given elsewhere. The results are shown in Fig. 3. We find activation energies of 0.60 ± 0.07 eV for the photoinduced dissociation and 2.6 ± 0.6 eV for thermal dissociation of the pairs. The difference between these activation energies is roughly equal to the recombination energy (~ 1.9 eV). Thus, we identify the (Zn, O)_i dissociation to be a "recombination-enhanced" reaction in which the energy available from electron-hole recombination is transferred to localized vibrational modes which leads to a reaction. The strong phonon coupling which is required for recombination-enhanced reactions is clearly evident in the photoluminescence spectrum, Fig. 1(b). The broad (Zn, O)_i band is primarily composed of a series of 6.0-meV phonon replicas,^{4,5} and multiple occupation of this 6.0-meV

mode probably provides the "critical reaction path" for the dissociation to proceed.

In conclusion, we have observed photoinduced dissociation of nearest-neighbor (Zn, O) pairs in GaP, and the formation of further separated pairs. As a result of the strong electron-phonon coupling in the (Zn, O)_i system, it is possible that the dissociation proceeds by the oxygen (or zinc) ion jumping from a substitutional to an interstitial site and migrating away. The ion is then captured by a vacancy to form a further separated pair with the nearest zinc (or oxygen) ion. From the local phonon-mode energies it seems that the oxygen ion is weakly bound in the GaP lattice, and so we suggest that it may be the oxygen (rather than the zinc) ion which makes the jump in the dissociation. The GaP:(Zn, O) system has provided us a unique opportunity for studying molecular defect reactions occurring in an ordered lattice.

The authors thank C. H. Henry for the GaP samples used in this study, and we gratefully acknowledge discussions with D. L. Smith, J. J. Lambe, A. T. Hunter, and G. S. Mitchard. One of us (RMF) is a recipient of a postgraduate scholarship from the National Sciences and Engineering Research Council of Canada. This work was supported in part by the U. S. Office of Naval Research under Contract No. N00014-81-K-0305.

¹J. J. Hopfield, D. G. Thomas, and M. Gershenzon, *Phys. Rev. Lett.* **10**, 162 (1963).

²R. H. Saul, J. Armstrong, and W. H. Hackett, Jr., *Appl. Phys. Lett.* **15**, 229 (1969).

³P. D. Dapkus and C. H. Henry, *J. Appl. Phys.* **47**, 4061 (1976).

⁴T. N. Morgan, B. Welber, and R. N. Bhargava, *Phys. Rev.* **166**, 751 (1968).

⁵C. H. Henry, P. J. Dean, and J. D. Cuthbert, *Phys. Rev.* **166**, 754 (1968).

⁶J. S. Jayson, R. N. Bhargava, and R. W. Dixon, *J. Appl. Phys.* **41**, 4972 (1970), and references contained therein.

⁷P. J. Dean, C. H. Henry, and C. J. Frosch, *Phys. Rev.* **168**, 812 (1968).

⁸Our calculations use $E_g = 2339$ meV, $E_A = 64$ meV, $E_D = 893$ meV, $\epsilon = 11.1$, $a_0 = 5.45$ Å for type-II geometry, and a van der Waals coefficient of zero.

⁹J. S. Prener, *J. Chem. Phys.* **25**, 1294 (1956).

¹⁰P. J. Dean and C. H. Henry, *Phys. Rev.* **176**, 928 (1968).

¹¹P. J. Dean and W. J. Choyke, *Adv. Phys.* **26**, 1 (1977).

¹²L. C. Kimerling, *Solid-State Electron.* **21**, 1391 (1978).

Reaction kinetics in GaP:(Zn,O)

R. M. Feenstra and T. C. McGill

California Institute of Technology, Pasadena, California 91125

(Received 8 December 1981)

Photoinduced reactions in which pairs of Zn_{Ga} and O_{P} ions in GaP dissociate and subsequently re-form are studied. The decay of nearest-neighbor (Zn,O) pair luminescence is measured versus laser power and temperature. The dissociation rate of the pairs is deduced with the use of a model for the electron-hole recombination kinetics which includes the effects of saturation and spatially dependent carrier generation. The activation energy for the photoinduced dissociation is found to be 0.60 ± 0.07 eV. Dissociation of the nearest-neighbor pairs by purely thermal mechanisms is also observed, with an activation energy of 2.6 ± 0.6 eV. From these activation energies and the observed pre-exponential factors, the photoinduced dissociation is determined to be a recombination-enhanced defect reaction. The dissociated nearest-neighbor pairs tend to re-form as pairs with small inter-ion separation.

I. INTRODUCTION

The properties of gallium phosphide doped with zinc and oxygen have been extensively studied, primarily because of the use of this material in light-emitting diodes. These diodes are observed to degrade under forward-bias operation.¹⁻³ In a previous paper,⁴ we have shown that this degradation is due to the dissociation of nearest-neighbor $(\text{Zn,O})_{m=1}$ pairs. When the GaP is subjected to laser excitation, we observe luminescence from radiative electron-hole recombination at the $(\text{Zn,O})_m$ pairs, where m refers to an m th-nearest-neighbor pair. At elevated temperatures, the nearest-neighbor pair luminescence intensity decreases with time due to the dissociation of the pairs. After the nearest-neighbor pair dissociates, it re-forms as a further separated pair. In this paper, we will examine the kinetics of this reaction. The word "kinetics" here has a twofold meaning: First, we will discuss the electron-hole recombination kinetics in order to relate the observed photoluminescence intensities with the impurity concentrations. Second, we will study some aspects of the kinetics of the atomic diffusion process in which the $(\text{Zn,O})_{m=1}$ pair dissociates and later re-forms as a further separated pair $(\text{Zn,O})_{m>1}$.

The major result of this work is that the $(\text{Zn,O})_{m=1}$ dissociation is a "recombination-enhanced" reaction in which energy available from electron-hole recombination is transferred to localized vibrational modes which leads to the dissociation. This type of reaction has not previously been

observed in a system which is as well characterized as GaP:(Zn,O). Thus, this system provides a good opportunity for studying the strong electron-phonon interaction which is often present at "deep-level" defects in semiconductors. The understanding of this interaction is important since it significantly affects the performance of semiconductor devices.^{5,6}

Photoluminescence (optical emission) data will be presented throughout this paper, and some experimental details are summarized in Sec. II. In Sec. III, equations are written describing the electron-hole recombination kinetics. We explicitly include the effects of saturation of the $(\text{Zn,O})_m$ electron occupation, and of spatially varying electron-hole generation. Several limits of these equations that are applicable to the experiments described here will be discussed. Simple relations between the observed photoluminescence intensities and the defect concentrations are derived. Using these relations, we present in Sec. IV of this work an analysis of the decay rates of the $(\text{Zn,O})_{m=1}$ luminescence intensities. The observed decay rates are shown to be proportional to the electron occupation of the pairs. At high laser powers the decay rates saturate and equal the dissociation rate of the pairs. From the temperature dependence of the dissociation rates, activation energies for the reactions are deduced. We show that the $(\text{Zn,O})_{m=1}$ pairs can dissociate by a recombination-enhanced process, or by purely thermal mechanisms.⁷ In Sec. V, data are presented on the distribution of $m > 1$ pairs that are formed by the dissociation of

the $m = 1$ pairs. A brief discussion is given of the process by which the Zn and O impurities diffuse through the lattice to form the $(\text{Zn},\text{O})_m$ pairs. The observed degradation rates are shown to be dependent on the details of this diffusion process. The conclusions which can be drawn from this work are presented in Sec. VI.

II. EXPERIMENTAL

The samples used in this work were liquid-phase-epitaxially grown p - n junctions on n -type GaP (single crystal). The growth technique is described by Saul, Armstrong, and Hackett.⁸ The exposed 50- μm thick layer of the junction is p type, doped with Zn and O. The (substitutional) O concentration is about 10^{16} cm^{-3} and the Zn concentration is about $3 \times 10^{17} \text{ cm}^{-3}$ (based on crystal-growth conditions). Other impurities include N and S. The photoluminescence spectra were obtained using a liquid-N₂-cooled S-1-type photomultiplier and a SPEX 1269 spectrometer with a 1200 lines/mm grating blazed at 1 μm . For the low-temperature work ($T < 100 \text{ K}$) reported here the sample was mounted in a variable-temperature cryostat and illuminated with the 4545- \AA line of an Ar⁺ laser. The sample was moved vertically to permit observation of different regions of the crystal and the change in photon collection efficiency between these runs was very small. For the high-temperature work ($300 \text{ K} < T < 700 \text{ K}$) the sample was mounted on a heating block and illuminated with the 4880- \AA line of an Ar⁺ laser, focused to a beam diameter of 55 μm full width at half maximum (FWHM). The maximum sample heating ΔT can be estimated from

$$\Delta T = \frac{P}{2\pi k \sigma} \quad (1)$$

where P is the absorbed laser power, k is the thermal conductivity [$k = 0.4 \text{ W/cm K}$ at 473 K for GaP (Ref. 9)], and σ is the beam width [FWHM equal to $2\sigma\sqrt{2\ln 2}$]. This formula is derived by solving the heat-diffusion equation in an infinite slab of thickness l with one side at a constant temperature and the other side exposed to a surface heat source with a Gaussian profile in the limit $\sigma \ll l$. For a typical power level of $P = 200 \text{ mW}$ we find $\Delta T = 35 \text{ K}$. For the results reported here the sample was in air, although similar results were obtained when the sample was in a He environment. Annealing studies ($T > 1000 \text{ K}$) were per-

formed in a furnace purged with He. Following each anneal the sample was quenched in water and etched for 3 min in 3:1:1 $\text{H}_2\text{SO}_4\text{:H}_2\text{O}_2\text{:H}_2\text{O}$ at 60°C.

III. ELECTRON-HOLE RECOMBINATION KINETICS

The kinetics of electron-hole recombination in GaP:(Zn,O) have been extensively studied.¹⁰⁻¹⁶ It is not the purpose of this work to obtain a detailed understanding of the recombination kinetics. Rather, we wish to arrive at approximate values for some of the kinetic parameters. From these values we will determine the regime of carrier concentrations in which our experiments lie, and this will enable us to make a reasonable interpretation of the data to be presented in Secs. IV and V.

We use a simple but accurate model which is similar to that used for nearest-neighbor pairs by Henry, Bachrach, and Schumaker.¹⁶ Each $(\text{Zn},\text{O})_m$ center is considered to be a single-electron trap, with an associated electron release rate R_m , capture rate C_m , and a total recombination rate $1/\tau_m$. For $m \rightarrow \infty$, i.e., isolated oxygen, a second electron level has been observed.⁵ Here we will be considering centers with $m < 50$ for which this level has not been observed and so we will ignore it. For the present discussion, the hole occupation of the $(\text{Zn},\text{O})_m$ centers will be implicitly included in the electron recombination rate $1/\tau_m$. Later, we will consider the dependence of $1/\tau_m$ on the various hole concentrations. The concentration n_m of $(\text{Zn},\text{O})_m$ centers which are occupied by electrons is given by

$$\frac{dn_m}{dt} = -\frac{n_m}{\tau_m} - R_m n_m + C_m (N_m - n_m) n_0, \quad m = 1, 2, 3, \dots, \quad (2)$$

where N_m is the total concentration of $(\text{Zn},\text{O})_m$ centers and n_0 is the free-electron concentration. In steady state, the concentration of occupied $(\text{Zn},\text{O})_m$ centers is found by equating Eq. (2) to zero to yield

$$f_m \equiv \frac{n_m}{N_m} = \frac{n_0/n_{1m}}{1 + n_0/n_{1m}}, \quad (3a)$$

where

$$n_{1m} \equiv \frac{1/\tau_m + R_m}{C_m}. \quad (3b)$$

Here, f_m represents the fractional electron occupation of the centers. The intensity of luminescence emitted from an m th-nearest-neighbor pair is given by

$$I_m = \frac{1}{\tau_m^{\text{rad}}} n_m = \frac{1}{\tau_m^{\text{rad}}} N_m f_m, \quad (4)$$

where $1/\tau_m^{\text{rad}}$ is the radiative decay rate. Later in this work we will discuss processes in which the impurity concentrations N_m vary with time. However, these time variations are very slow compared with those expressed in Eq. (2); therefore Eq. (3) is still valid at each point in time.

Let us consider the minority-carrier (electron) concentration n_0 . The variables of interest in these experiments are the laser power P , the temperature T , and the impurity concentrations N_i . The impurities labeled N_i include the $(\text{Zn}, \text{O})_m$ centers as well as various intrinsic impurities that could be undergoing photoinduced reactions.^{3,17} In steady state n_0 is in general a function of T , P , and N_i . Neglecting spatial diffusion of the carriers we write

$$n_0 = G\tau_0, \quad (5)$$

where G is the electron-hole generation rate and τ_0 is defined by this equation to be the steady-state minority-carrier lifetime. We will assume that τ_0 has no spatial dependence. This neglects effects such as surface recombination. The spatial dependence of G is derived by considering the incident laser beam that is perpendicular to the surface (x, y plane) of the crystal. The photon density has a Gaussian dependence on $\rho = [(x^2 + y^2)]^{1/2}$ and varies exponentially with z (the direction into the crystal). Thus, the generation rate can be expressed

$$G = \frac{\alpha P}{h\nu_i 2\pi\sigma^2} \exp \left[\frac{-\rho^2}{2\sigma^2} - \alpha z \right], \quad (6)$$

where P is the absorbed laser power, $1/\alpha$ is the absorption depth, σ is the beam radius, and $h\nu_i$ is the incident photon energy. The minority-carrier lifetime τ_0 is determined by all of the various recombination channels in the material. In our experiments we observe quantities which are independent of τ_0 , and so we do not need to know its precise value. The minority-carrier concentration can be estimated by observing the luminescence intensity as a function of laser power.¹¹ For the nearest-neighbor pairs at $T = 500$ K we observe a significant saturation effects ($f_1 \approx 0.5$) to begin at

$P = 100$ mW (FWHM = 55 μm). At this temperature $1/\tau_1 \approx 10^6 \text{ s}^{-1}$ (Ref. 16) $< R_1 \approx 10^8 \text{ s}^{-1}$ (Ref. 14). The maximum minority-carrier concentration is then given by $n_0 \approx n_{t1} \approx R_1/C_1 \approx 5 \times 10^{15} \text{ cm}^{-3}$. This also equals the concentration of majority carriers (holes) introduced by the laser. From Eqs. (5) and (6) this value of n_0 corresponds to a lifetime of $\tau_0 \approx 1$ ns, which seems quite reasonable.

Much of the complicated electron-hole recombination kinetics has been hidden in the rates $1/\tau_0$, $1/\tau_m$, and $1/\tau_m^{\text{rad}}$. The rate of $1/\tau_m$ is the sum of nonradiative and radiative rates. There are two nonradiative decay channels: Auger decay¹⁴ and multiphonon-emission (MPE) recombination.⁵ There are also two radiative decay channels: The bound electron can recombine with a hole bound onto the same $(\text{Zn}, \text{O})_m$ center, or with a hole bound onto a distant impurity, namely, a Zn acceptor.^{10,18} The rates $1/\tau_m$ and $1/\tau_m^{\text{rad}}$ are therefore functions of the temperature and various hole concentrations. The concentration of holes introduced by the laser is small compared with the free-hole concentration of $p \approx 10^{17} \text{ cm}^{-3}$ for $T \geq 300$ K. Furthermore, at these temperatures the shallowly bound holes are in equilibrium with the free holes.^{15,16} Thus, $1/\tau_m$ and $1/\tau_m^{\text{rad}}$ will be functions only of temperature and will have very little spatial or time dependence.

Now let us specialize to the experiments described here. For ease of discussion we separate these into two cases. First we consider the high-temperature results which will be presented in Sec. IV. In these experiments the sample is exposed to the laser at some temperature $300 \text{ K} < T < 700 \text{ K}$ and some laser power P . The intensity of $(\text{Zn}, \text{O})_{m=1}$ luminescence is observed to decrease with time, presumably due to some changing impurity concentration N_i . The luminescence intensity is given by

$$I_1(t) = \frac{1}{\tau_1^{\text{rad}}} \int dV N_1(\rho, z, t) f_1(\rho, z, t), \quad (7)$$

where the spatial dependence of f_1 is given by Eqs. (3a), (5) and (6). At low power levels the electron occupation f_1 is proportional to the minority-carrier concentration n_0 . In general, n_0 changes with N_i and results in changes in the $(\text{Zn}, \text{O})_{m=1}$ luminescence intensity. We have observed these effects. At low powers a change in n_0 will cause the entire luminescence spectrum to change uniformly. However, at high powers the luminescence band saturates; $f_1 \rightarrow 1$ for most of the centers contribut-

ing to the band. In that case the luminescence intensity is independent of n_0 . The observed decreasing intensity is due to a decreasing concentration of $(\text{Zn},\text{O})_1$ pairs, and the intensity is directly proportional to the pair concentration. The data presented in Sec. IV is in this high-power regime.

The second case to discuss are the low-temperature results presented in Sec. V. Here we observe luminescence from different regions of a sample which have different pair concentrations N_m . Care was taken to keep the temperature, laser power, and photon collection efficiency constant between the different regions. The luminescence intensity from various shallow impurities is observed to be identical in the regions, so that the electron and hole concentrations are probably constant. This implies that f_m and $1/\tau_m^{\text{rad}}$ are constant. Therefore, from Eq. (4), the ratio of luminescence intensities equals the ratio of pair concentrations in the different regions.

IV. REACTION RATES

In Fig. 1 we show several high-temperature photoluminescence spectra. As discussed in our previous publication⁴ these spectra consist of a band centered at 1.7 eV due to nearest-neighbor $(\text{Zn},\text{O})_{m=1}$ pairs, and a band centered at 1.5 eV due to further separated pairs $(\text{Zn},\text{O})_{m>1}$. There is also luminescence at 2.1 eV due to various shallow

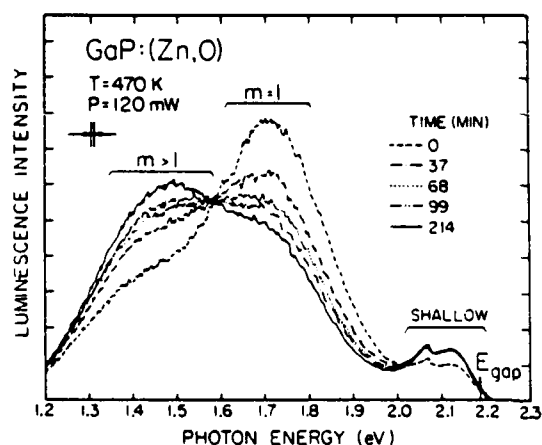


FIG. 1. High-temperature photoluminescence spectra from (Zn,O) donor-acceptor pairs. The labels m denote luminescence from an m th-nearest-neighbor pair. Several successive scans are shown. The luminescence intensities are changing with time, indicating defect reactions in progress.

impurities and possibly free-exciton or band-to-band recombination. In Fig. 1 the time between successive scans is about 30 min. We see that the intensity of the $(\text{Zn},\text{O})_{m=1}$ luminescence is decreasing and the intensity of the $(\text{Zn},\text{O})_{m>1}$ luminescence is increasing. For the high laser power used in Fig. 1 the $m=1$ and $m>1$ bands are saturated (at least initially, see below), and so their changing intensities are due to changing pair concentrations. Clearly the nearest-neighbor pairs are dissociating at some rate, and further-separated pairs are forming at the same rate. We refer to this reaction as an "aging" process. This reaction was first studied in luminescence by Dapkus and Henry² and was identified in our previous paper.⁴

The $(\text{Zn},\text{O})_{m=1}$ dissociation reaction is not a thermal one, since the temperature in Fig. 1 is only 470 K (sample heating due to the laser is about 20 K), and the $(\text{Zn},\text{O})_{m=1}$ pairs are thermally stable up to 800 K. Rather, the reaction is photoinduced.² The incident light creates electron-hole pairs in the material, and the electrons and holes may be captured and may recombine at the (Zn,O) centers. The energy to dissociate the $(\text{Zn},\text{O})_{m=1}$ pairs comes from some electron (or hole) capture or recombination event at the defect. In our previous work⁴ we identified this event to be electron-hole recombination. Here, we will give a detailed

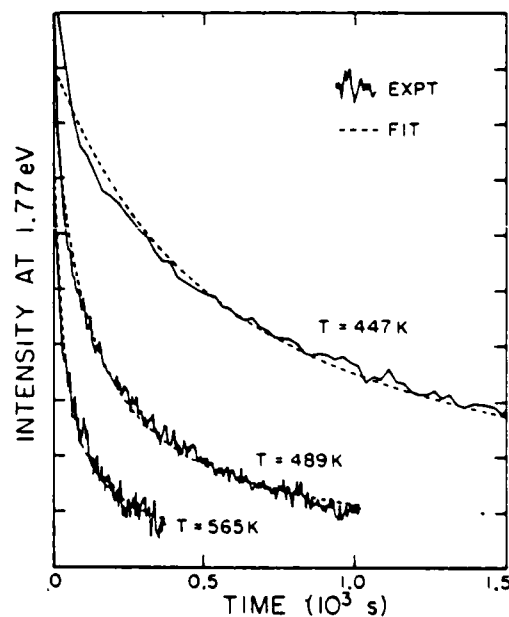


FIG. 2. Decay of the nearest-neighbor $(\text{Zn},\text{O})_{m=1}$ luminescence at various temperatures T . The data were fitted to a theoretical form corresponding to the $f(0,0) \rightarrow 0$ curve shown in Fig. 3.

account of how we arrived at this identification.

The decay (intensity versus time) of the $(\text{Zn}, \text{O})_{m=1}$ luminescence is nonexponential. Figure 2 shows several decay curves. Typically, the luminescence intensity initially changes relatively fast, then it slows down to a long-lived tail. We attribute this nonexponential behavior to a nonuniform minority-carrier (electron) density in the material. This nonuniformity is due to the Gaussian profile of the incident laser beam and the exponential dropoff of its intensity into the sample. A nonuniform electron density results in a nonuniform electron occupation of the $(\text{Zn}, \text{O})_1$ centers. Those centers with high occupation ($f_1 \rightarrow 1$) dissociate at some rate, and those centers with low occupation ($f_1 \rightarrow 0$) dissociate at a much slower rate. The observed decay curves are integrals over the sample of all the individual exponential decays. The result is a nonexponential decay. For high laser powers the observed luminescence is initially due almost entirely to the saturated centers. In that case the luminescence intensity is proportional to the pair concentration and independent of n_0 , as discussed in Sec. III. At later times we observe those centers whose occupation is lower. Then, the luminescence intensity may depend on n_0 . We can monitor n_0 by observing the intensity of luminescence from the shallow impurity levels. As shown in Fig. 1, the variation in n_0 occurs over a much shorter time period than the $(\text{Zn}, \text{O})_{m=1}$ decay time. We observe that this is true for $P \geq 100$ mW at all of the temperatures discussed here. Thus, the final part of the decay curves are not affected by n_0 because it is a constant. Therefore, we need not further concern ourselves with the time dependence of n_0 or f_1 .

The degradation observed by Henry and Dapkus³ is also reported to be nonexponential. In their case the degradation was accomplished using forward biased p - n junctions in which the minority-carrier concentration varies exponentially with distance from the junction. This produces nonexponential degradation characteristics similar

to those reported here. Another example of nonexponential behavior is seen in carrier capture or emission rates as observed in deep-level transient spectroscopy (DLTS).^{19,20} The carrier capture rate is proportional to the free-carrier density. This density is spatially varying at the edge of the depletion region. The resulting capture curves are nonexponential with a long-lived tail on them.²¹ However, with a large enough reverse bias, the size of the depletion region is large compared with the edge region, and these effects can be minimized. In our experiments the laser power is never large enough to produce an essentially uniform excitation region, and so the nonexponential effects are always significant.

Let us now derive a functional form for the observed decay curves. From Eqs. (2)–(6) we find that the electron occupation of the $(\text{Zn}, \text{O})_1$ centers is given by

$$f(\rho, z) = \frac{f(0,0) \exp \left[\frac{-\rho^2}{2\sigma^2} - az \right]}{1 + f(0,0) \left[\exp \left[\frac{-\rho^2}{2\sigma^2} - az \right] - 1 \right]}, \quad (8)$$

where we have dropped the subscript 1. We assume that the dissociation rate of a given center is proportional to its occupation. This assumption is justified below. Thus, the concentration of $(\text{Zn}, \text{O})_1$ centers at (ρ, z) varies with time according to

$$N(\rho, z, t) = N(0) \exp[-f(\rho, z)rt], \quad (9)$$

where r is the reaction rate and $N(0)$ is the spatially uniform impurity concentration at $t=0$. We are now ready to derive the main theoretical result of this paper: the time dependence of the $(\text{Zn}, \text{O})_1$ luminescence intensity in a model where the pairs are dissociating at a rate proportional to their spatially dependent electron occupation. From Eqs. (7)–(9) the total intensity of $(\text{Zn}, \text{O})_1$ luminescence is evaluated to be

$$I(t) = \frac{N(0)f(0,0)\sigma^2}{\tau_1^{\text{rad}}\alpha} \int_0^1 du \ln \left[\frac{1}{u} \right] \frac{\exp \left[\frac{-f(0,0)urt}{1 + f(0,0)(u-1)} \right]}{1 + f(0,0)(u-1)}. \quad (10)$$

Figure 3 shows several examples of Eq. (10) for various values of $f(0,0)$. For $f(0,0) \rightarrow 1$ the decay is purely exponential. This corresponds to an infinitely large excitation region with uniform occu-

pation of all the centers. For $f(0,0) \rightarrow 0$ the decay follows an exponential integral form. In our experiments $f(0,0) < 0.9$. From Fig. 3 we see that Eq. (10) is quite well approximated by its $f(0,0) \rightarrow 0$

limit,

$$I(t) \approx \frac{a}{r_0 t} [\gamma + \ln(r_0 t) + E_1(r_0 t)] + b, \quad (11)$$

where a is a constant, γ is Euler's constant, $r_0 = f(0,0)r$ is the observed decay rate, and E_1 is an exponential integral of the first kind. To this form we have added another constant b to account for the background intensity due to $(\text{Zn},\text{O})_{m>1}$. Equation (11) provides a good fit to all of the observed decay curves. This is the real justification for using it.

The data shown in Fig. 2 were fitted to the functional form Eq. (11). The decay curves shown in the figure have a background intensity b (determined from the fit) subtracted from them. The decay rates determined from the fits are plotted in Fig. 4 versus the incident laser power. At low powers the rates increase linearly with power; at high powers the rates approach some limit: the saturated decay rate. The decay rates saturate when the electron occupation saturates. This justifies the above assumption that the dissociation rate is proportional to the electron occupation. The saturation power level increases with temperature as expected from Eq. (3b). The fact that the decay rates do indeed saturate provides evidence that sample heating and large hole concentrations due to the laser excitation are not significantly affect-

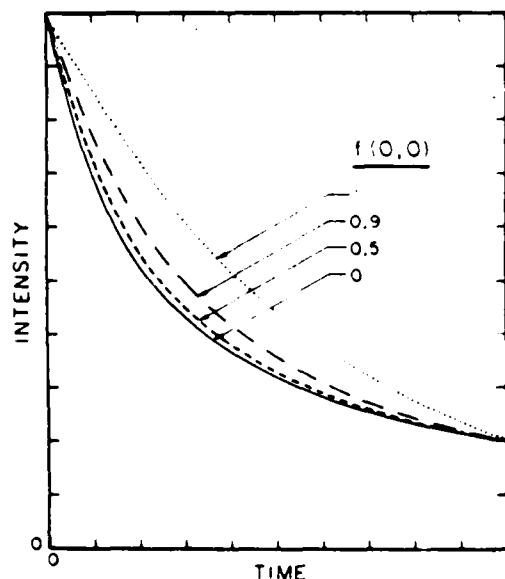


FIG. 3. Theoretical curves for the decay of the $(\text{Zn},\text{O})_{m=1}$ luminescence. $f(0,0)$ is the maximum electron occupation of the centers. $f(0,0) \rightarrow 1$ for very large laser powers and $f(0,0) \rightarrow 0$ for small laser powers. For the experiments described here, $f(0,0) < 0.9$.

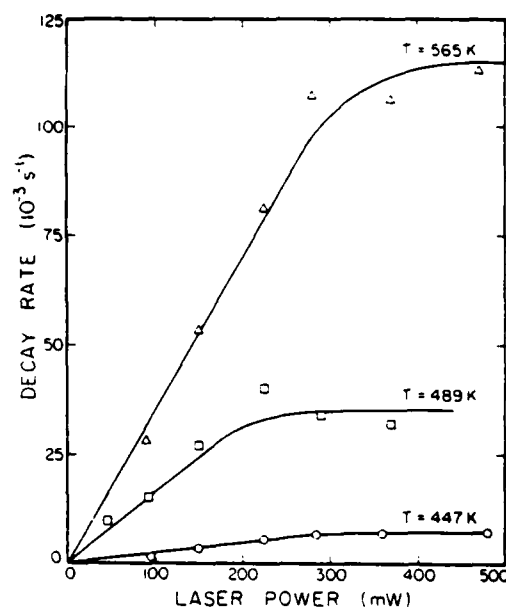


FIG. 4. Decay rates of the $(\text{Zn},\text{O})_{m=1}$ luminescence vs the laser power. For high powers the decay rates saturate due to saturation of the electron occupation of the centers. The solid lines are drawn as a guide to the eye.

ing our results.

The saturated decay rates are plotted versus temperature in Fig. 5. We find an activation energy of 0.60 ± 0.07 eV with a preexponential factor of approximately $3 \times 10^4 \text{ s}^{-1}$. Similar activation energies have been observed in other GaP:(Zn,O) degradation studies.^{1,3} For the data in Fig. 5 we have

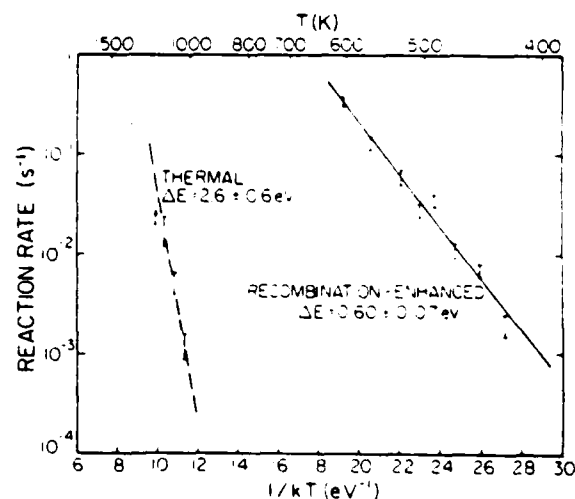


FIG. 5. Dissociation rates of $(\text{Zn},\text{O})_{m=1}$ pairs. The rates labeled "recombination-enhanced" are for photoinduced dissociation of the pairs, in the limit of high laser power. The rates labeled "thermal" are for pair dissociation by purely thermal means.

not included any corrections to the temperature due to sample heating since these corrections produce a negligible change to the activation energy within the quoted uncertainties. In addition to measuring the activation energy for the photoinduced reaction, we have also measured the barrier for the nearest-neighbor dissociation to proceed by purely thermal means. The procedure consisted of observing the absolute intensity of luminescence (at 1.77 eV) from a sample, putting it in a furnace for some amount of time, removing, quenching, and etching the sample, and finally observing again the luminescence intensity. The annealing temperatures were greater than 600°C (the initial state of the crystal⁸) and so the luminescence intensity decreased with annealing time due to dissociation of the nearest-neighbor pairs.⁷ The resulting exponential decay rates are shown in Fig. 5. The activation energy is 2.6 ± 0.6 eV with a preexponential factor of approximately 10^{10} s^{-1} . This activation energy represents the barrier for dissociation of $(\text{Zn},\text{O})_1$ without a bound electron on the center (let us call this the ground state of the complex).

Now let us consider what mechanisms may be responsible for the photoinduced dissociation reaction. From the literature^{6,22} we identify two mechanisms which have been observed in other systems. First, the $(\text{Zn},\text{O})_1$ dissociation could be a "recombination-enhanced" defect reaction (REDI) in which energy available from electron-hole recombination is transferred to localized vibrational modes which leads to a reaction. This is the mechanism we believe to cause the reactions observed here. The activation energy of 0.60 eV we identify roughly as the difference between the thermal barrier (2.6 ± 0.6 eV) and the recombination energy (~ 1.9 eV). Since all of the recombination energy is used in surmounting the barrier, the reaction is the result of nonradiative recombination by multiphonon emission (MPE). Although MPE recombination has not been reported for $(\text{Zn},\text{O})_1$ it has been reported⁵ for isolated O and it seems likely that it also occurs for $(\text{Zn},\text{O})_1$. The fraction of MPE recombination events which lead to a pair dissociation is estimated to be 10^{-4} (roughly, this is the value of η as defined in Ref. 6).

The second mechanism that must be considered is a "charge-state" reaction in which the $(\text{Zn},\text{O})_1$ dissociation would occur thermally from the excited state of the complex in which the bound electron is present. At high laser powers the pairs are almost always in this state. The observed 0.60 eV would be identified as the thermal reaction barrier

for this excited state. This is rather different than the ground-state barrier of 2.6 eV. A nearest-neighbor Coulomb attraction of 0.55 eV cannot completely account for this difference. Furthermore, the observed $3 \times 10^4 \text{ s}^{-1}$ is about 9 orders of magnitude less than a phonon frequency. This implies a multijump process in which the (Zn,O) pair dissociates and recombines 10^9 times before permanently dissociating, or in which a third particle is needed for the reaction and must diffuse to the site. Although we cannot prove that these processes are not occurring, we consider them to be unlikely and we prefer the simpler explanation of the recombination-enhanced reaction.

V. KINETICS OF ATOMIC DIFFUSION

In this section we will consider some aspects of the (Zn,O) pair dissociation and subsequent reformation. The strong electron-phonon coupling required for a REDR is clearly evident in the $(\text{Zn},\text{O})_1$ photoluminescence spectra.⁴ This strong coupling suggests that the reaction may proceed without the presence of any additional defects. Thus, it seems quite likely that the oxygen (or zinc) simply jumps from its substitutional site to an interstitial site and migrates away. The mobile ion is subsequently captured by a vacancy to form a $(\text{Zn},\text{O})_m$ pair with the nearest zinc (or oxygen) ion. The observed activation energy of 0.60 eV will in general contain contributions from each of the processes: dissociation, diffusion, and reformation. From Fig. 5 it is clear that the observed reaction is a first-order kinetic process. Also, as shown in Fig. 1 the $(\text{Zn},\text{O})_{m>1}$ pairs form at exactly the same rate as the $(\text{Zn},\text{O})_{m=1}$ pairs dissociate. Thus, the rate limiting process is the dissociation, and the observed rates are indeed the rates for dissociation. We emphasize that it is the dissociation of the pairs which we believe to be a photoinduced reaction. The subsequent diffusion and reformation can probably occur thermally at the temperatures considered here.

We have studied the pair re-formation process by measuring the number of pairs of a given shell number m which are produced by the aging process. Figure 6 shows low-temperature spectra in an unaged and an aged sample. The discrete lines in the spectra are $(\text{Zn},\text{O})_m$ donor-acceptor (DA) luminescence. The broad background is due to radiative processes involving mainly recombination of electrons bound to $m=1$ and 2 pairs with holes bound to distant acceptors. The pairs responsible

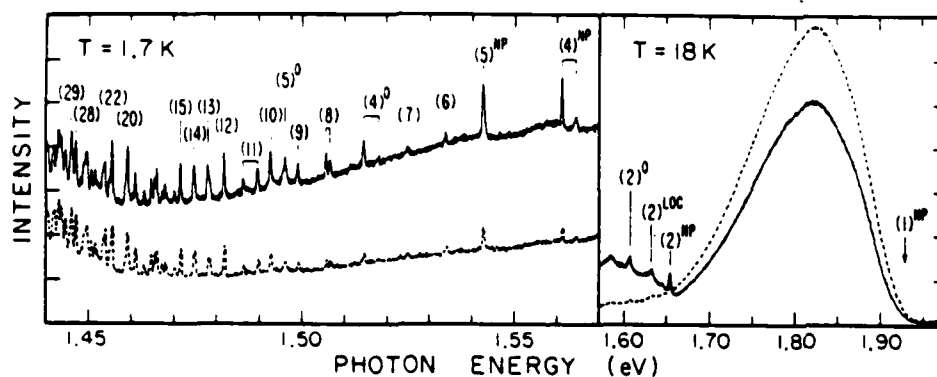


FIG. 6. Low-temperature donor-acceptor luminescence from an aged (solid line) and an unaged (dashed line) sample. The lines are labeled by m for m th-nearest-neighbor pairs with a superscript indicating the type of phonon involved in the transition (O is optical, LOC is local, NP is no-phonon). Those labels with no superscripts refer to no-phonon transitions. Note the intensity and energy scale change at 1.57 eV. The data on the left had a flat background subtracted from it.

for the discrete DA lines are labeled in accordance with previous identifications.^{4,23} As discussed in Sec. III, the ratio of line intensities is equal to the ratio of pair concentrations in the samples. In the aged material, the line intensity is the sum of that from the new centers produced by the aging and that from the centers which existed prior to the aging. Thus, the concentration of centers produced by the aging is given by

$$N'_m = N_m \left[\frac{I'_m}{I_m} - 1 \right], \quad (12)$$

where I_m and I'_m are the luminescence intensities in the unaged and aged sample, respectively, and N_m is the pair concentration in the unaged material. N_m can be computed²⁴ by considering equilibrium between oppositely charged ions at the growth temperature of the crystal. For small m this is a very crude model, but it has been shown to give reasonable results.⁷

The concentration of new $m > 1$ centers produced by the aging process is dependent on the sample conditions prior to aging. Figure 7 shows typical results, based on the integrated DA line intensities of Figure 6. We see that the dissociated nearest-neighbor pairs tend to re-form as pairs with low m . The distribution of new centers contains some information about the pair re-formation process. At present we do not have a theory which allows us to uniquely identify the re-formation mechanism. In general, it appears that the mobile ion and/or the vacancy tend to stay in the vicinity of a dissociated center (i.e., an isolated Zn or O). In any case, we always observe that for $1 < m \leq 10$ the distribution of new centers increases sharply with decreasing m . In fact, we feel that this distri-

bution can be extended to include $m = 1$. This extension is reasonable since we cannot think of any physical process which would allow the formation of $m > 1$ pairs while prohibiting the formation of $m = 1$ pairs. Thus, we conclude that a significant number of the dissociated $m = 1$ pairs re-form as

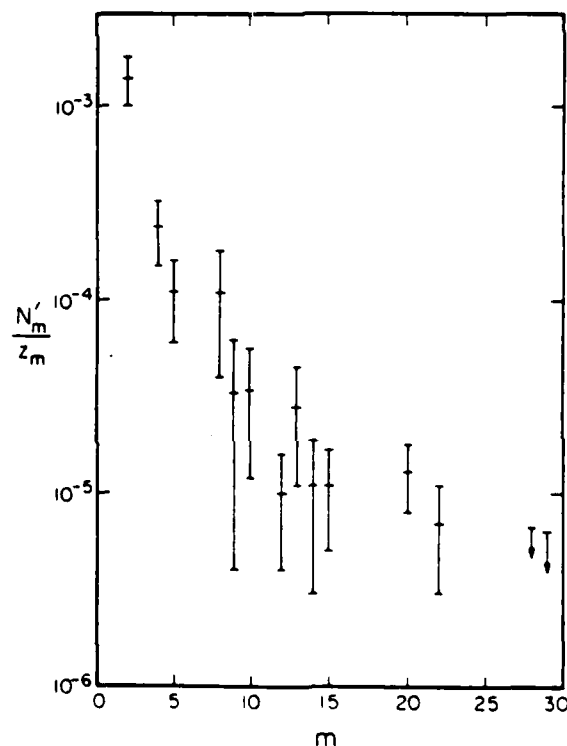


FIG. 7. The distribution of new pairs formed by the aging process. N'_m is the concentration of the m th-nearest-neighbor pairs, normalized to the total concentration of pairs (estimated) in the sample. z_m is the number of equivalent m th-nearest-neighbor sites.

other $m = 1$ pairs. These pairs are subsequently dissociated and the entire aging process stops when all of the dissociated $m = 1$ pairs re-form as $m > 1$ pairs.

Clearly the observed aging rates will be proportional to the probability of not re-forming as a $m = 1$ pair. In order to minimize the device degradation rate, the probability for $m = 1$ re-formation should be maximized. This probability is dependent on the sample conditions. For example, Bergh¹ found that the presence of Cu in GaP:(Zn,O) produces an increase in the observed degradation rates. We would interpret this as being due to the formation of complexes between the dissociated, mobile ion(s) and the Cu impurity, thereby eliminating the chance of producing another $m = 1$ pair. The net dissociation rate can be affected by many other similar processes. The rates of these processes must be controlled in order to produce devices with the longest lifetime.

VI. CONCLUSIONS

In this paper we have given a detailed description of photoinduced reactions between nearest-neighbor zinc and oxygen impurities in gallium phosphide. These reactions were first observed by Henry and Dapkus.^{2,3} In a previous work⁴ we demonstrated that the $(\text{Zn},\text{O})_1$ pairs were dissociating and subsequently re-forming as further separated pairs. Here, we report measurements of the dissociation rates. The observed luminescence decay

curves are analyzed by a model of the electron-hole recombination kinetics which includes the effects of saturation and a spatially dependent generation rate. From the resulting dissociation rates, in the limit of high laser power, the activation energy for the photoinduced dissociation is found to be 0.60 ± 0.07 eV. We also report observations of the purely thermal dissociation of the pairs, with an activation energy of 2.6 ± 0.6 eV. From these activation energies along with the observed preexponential factors, we conclude that the dissociation is a recombination-enhanced defect reaction. A nonradiative electron-hole recombination event puts the $(\text{Zn},\text{O})_1$ center into a highly excited vibronic state, resulting in the dissociation. The atomic motion in the dissociation and re-formation is not well understood. However, we propose that in the dissociation the oxygen (or zinc) ion jumps to an interstitial site. This interstitial ion then diffuses thermally some short distance and is captured by a vacancy to form a pair with the nearest zinc (or oxygen) ion.

ACKNOWLEDGMENTS

The authors thank C. H. Henry for the GaP samples used in this study. One of us (R.M.F.) is the recipient of a postgraduate scholarship from the Natural Sciences and Engineering Research Council of Canada. This work was supported in part by the U. S. Office of Naval Research under Contract No. N00014-81-K-0305.

¹A. A. Bergh, IEEE Trans. Electron Devices **18**, 166 (1971).

²P. D. Dapkus and C. H. Henry, J. Appl. Phys. **47**, 4061 (1976).

³C. H. Henry and P. D. Dapkus, J. Appl. Phys. **47**, 4067 (1976).

⁴R. M. Feenstra and T. C. McGill, Phys. Rev. Lett. **47**, 925 (1981).

⁵C. H. Henry and D. V. Lang, Phys. Rev. B **15**, 989 (1977).

⁶L. C. Kimerling, Solid State Electron **21**, 1391 (1978).

⁷A. Onton and M. R. Lorenz, Appl. Phys. Lett. **12**, 115 (1968).

⁸R. H. Saul, J. Armstrong, and W. H. Hackett, Jr., Appl. Phys. Lett. **15**, 229 (1969).

⁹H. F. Wolf, *Semiconductors* (Wiley, New York, 1971), p. 84.

¹⁰J. D. Cuthbert, C. H. Henry, and P. J. Dean, Phys. Rev. **170**, 739 (1968).

¹¹J. S. Jayson, J. Appl. Phys. **41**, 3854 (1970).

¹²R. N. Bhargava, J. Appl. Phys. **41**, 9 (1970).

¹³J. M. Dishman, M. DiDomenico, Jr., and R. Caruso, Phys. Rev. B **2**, 1988 (1970).

¹⁴J. S. Jayson, R. N. Bhargava, and R. W. Dixon, J. Appl. Phys. **41**, 4972 (1970).

¹⁵J. S. Jayson and R. Z. Bachrach, Phys. Rev. B **4**, 477 (1971).

¹⁶C. H. Henry, R. Z. Bachrach, and N. E. Schumaker, Phys. Rev. B **8**, 4761 (1973).

¹⁷D. V. Lang and L. C. Kimerling, Appl. Phys. Lett. **28**, 248 (1976).

¹⁸C. H. Henry, P. J. Dean and J. D. Cuthbert, Phys. Rev. **166**, 754 (1968).

¹⁹D. V. Lang, J. Appl. Phys. **45**, 3014 (1974).

²⁰D. V. Lang, in *Topics in Applied Physics*, edited by P. Braunlich (Springer, Berlin, 1979), Vol. 37, p. 93.

²¹Reference 20, p. 122.

²²P. J. Dean and W. J. Choyke, Adv. Phys. **26**, 1 (1977).

²³P. J. Dean, C. H. Henry, and C. J. Frosch, Phys. Rev. **168**, 812 (1968).

²⁴J. S. Prener, J. Chem. Phys. **25**, 1294 (1956).

Role of Fe in new luminescence lines in Si:Tl and Si:In

T. E. Schlesinger and T. C. McGill

California Institute of Technology, Pasadena, California 91125

(Received 28 December 1981)

We report on the experimental results which indicate that complexes of Fe with Tl are likely to be the origin of the recently observed *A, B, C* lines. We have also confirmed that diffusion of Fe produces substantial increase in similar lines, labeled *P, Q, R*, observed in Si:In.

The luminescence spectra of Si:In have been studied in much detail.¹⁻⁴ In particular long-lived lines were observed in the work of Lightowlers and Vouk² and by Mitchard *et al.*,⁵ who labeled these lines *P, Q, R*. Weber *et al.* suggested that these lines were a result of an Fe-In complex with a $\langle 100 \rangle$ axial symmetry.⁶ More recently a similar set of luminescence lines were observed by Thewalt *et al.* in Si:Tl.⁷ In this Report we present evidence that the luminescence observed by Thewalt *et al.* in Si:Tl is created by the introduction of Fe into Tl-doped Si samples. We confirm the observations of Weber *et al.* that the long-lived lines observed in Si:In are also enhanced upon the introduction of Fe into those samples.

Iron is introduced into the samples as follows. A layer of iron is evaporated onto the surface of the sample after it has been cleaned using a chemical etch ($3\text{HNO}_3:1\text{CH}_3\text{COOH}:0.4\text{HF}$). The iron is then diffused into the sample by annealing it at 1100°C for 1 h and then quickly quenching the sample in distilled water. The surface is then cleaned again using the same chemical etch. We estimate that this procedure results in an iron concentration of 10^{15} cm^{-3} .⁸ The photoluminescence spectra were obtained using a Coherent Model CR 3000 K krypton-ion laser for above-band-gap excitation. The laser was operated in cw mode at a peak output power of 4 W. The luminescence was then collected from the edge of the sample and directed through the entrance slits of a Spex Model 1404 spectrometer and measured with a Ge detector.

In Fig. 1, we present the spectrum of Si:Tl before (upper panel) and after (lower panel) Fe diffusion. The spectra were taken at 4.2 K and are labeled with the notation used by Thewalt *et al.* The spectrum in the top half of Fig. 1 is plotted on a different arbitrary intensity scale than that in the lower panel. The large peak is the thallium

bound-exciton line and the smaller peaks at lower energies are probably due to donor-acceptor luminescence resulting from the unintentional presence of P in the samples. This same spectrum is presented in the bottom half of the figure along with the spectrum from the sample diffused with iron. To indicate the intensities of the various lines relative to the bound-exciton line for Si:Tl, the two spectra in this panel have been scaled so that the Tl bound-exciton line is of the same intensity in both.⁹ These spectra show that after the

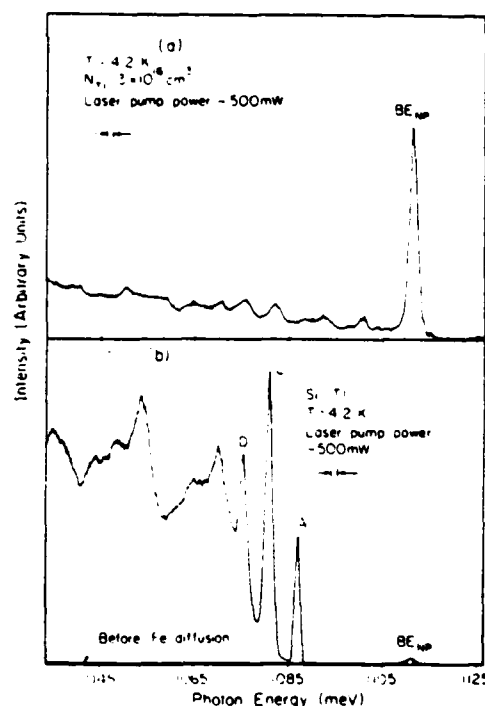


FIG. 1. (a) Photoluminescence spectrum of Si:Tl (a) before Fe diffusion, and (b) after Fe diffusion at 4.2 K taken using a Ge detector. The line labeled BE is the Tl bound-exciton line.

diffusion of Fe the *A, C, D* lines in Si:Tl are increased in intensity from not being observable in the spectra before diffusion to dominating the spectrum after diffusion. When some care was taken not to contaminate the samples and when we subjected them to the same cleaning and annealing procedure without iron this luminescence did appear. The luminescence was, however, more than an order of magnitude less intense relative to the Tl bound-exciton line than in samples into which iron was diffused. We attribute the appearance of the luminescence to the presence of iron in the as-grown material or to slight contamination during the processing. This result is consistent with the work of Mitchard *et al.*⁵ in Si:In in which *P, Q, R* luminescence was observed without intentionally introducing iron into their samples.

In Fig. 2 we present the spectrum of Si:In before and after iron diffusion and following the labeling scheme of Mitchard *et al.*⁵ Again the spectra were taken at 4.2 K and are presented so that the In bound-exciton line has the same intensity in both. The spectra show that after the diffusion of Fe the *P, Q, R* lines in Si:In are increased in intensity from being barely observable to dominating the spectra. We have also observed in the case of Si:In that the luminescence can be diminished by annealing the samples at high temperatures (1100°C) and allowing them to cool slowly. This can be attributed to the iron precipitating out of the samples.⁸

In summary, we have shown that the introduction of Fe in Si:Tl produces the luminescence reported by Thewalt *et al.*, implying that this luminescence is due to an Fe-Tl complex. We have also made observations which confirm the conclusions

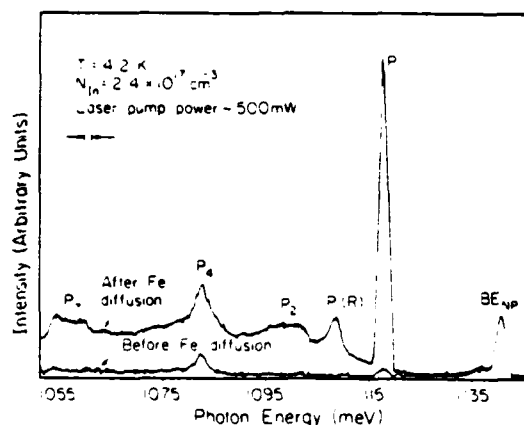


FIG. 2. Photoluminescence spectra of Si:In before and after Fe diffusion (as labeled) at 4.2 K taken using a Ge detector. The line labeled BE is the In bound-exciton line.

of Weber *et al.*⁶ that the *P, Q, R* luminescence observed in Si:In is due to an Fe-In complex.

The authors are pleased to acknowledge useful technical discussions with R. M. Feenstra and thank J. Weber for providing copies of unpublished work reporting the results at Stuttgart. Measurements of the carrier concentration were carried out at Hughes Research Laboratories where H. Kumura and F. Harvey have provided us with the samples. This work was supported in part by Office of Naval Research under Contract No. NO0014-81-C-0285. One of us (T.E.S) received financial assistance from the Natural Sciences and Engineering Research Council of Canada.

¹P. J. Dean, J. R. Haynes, and W. F. Flood, *Phys. Rev.* **161**, 711 (1967).

²M. A. Vouk and E. C. Lightowers, *J. Lumin.* **15**, 357 (1977).

³M. A. Vouk and E. C. Lightowers, *Proceedings of the Thirteenth International Conference on the Physics of Semiconductors, Rome, 1976*, edited by F. G. Fumi (Tipografia Marves, Rome, 1977), p. 1098.

⁴S. A. Lyon, D. L. Smith, and T. C. McGill, *Phys. Rev. B* **17**, 2620 (1978).

⁵G. S. Mitchard, S. A. Lyon, K. R. Elliott, and T. C. McGill, *Solid State Commun.* **29**, 425 (1979).

⁶J. Weber, R. Sauer, and P. Wagner, in *Proceedings of the International Conference on Luminescence, Berlin, 1981*, edited by I. Broser (North-Holland, Amsterdam, 1981).

⁷M. L. W. Thewalt, U. O. Ziemelis, and R. R. Parsons, *Phys. Rev. B* **24**, 3655 (1981).

⁸K. Graff and H. Pieper, *J. Electrochem. Soc.* **128**, 669 (1981).

⁹The process of introducing Fe into the Si is not likely to result in any change in the Tl concentration since Tl is such a large atom that diffusion is unlikely at the temperature used in the Fe diffusion.

Periodicity in the undulation spectra of GaP:N

R. M. Feenstra and T. C. McGill

California Institute of Technology, Pasadena, California 91125

(Received 22 March 1982)

The approximately periodic undulations observed in luminescence spectra of GaP:N are shown to arise from the long-range order of the crystal lattice. The period of the oscillations is equal to the separation of the lattice planes.

The luminescence spectra of GaP:N codoped with acceptors displays approximately periodic undulations.¹ A variety of explanations have been proposed for this undulatory behavior.²⁻⁵ Finally, it was shown by Street and Wiesner⁵ that the luminescence is due to a series of zero-phonon lines of excitons bound to N-acceptor pairs. The undulatory behavior of the spectra results from the properties of $N(r)$, the distribution of acceptor sites located at distance r from the donor site. Street and Wiesner observed that fluctuations in $N(r)$ existed, and they speculated that these fluctuations were purely random in origin. In this paper, we show that $N(r)$ is composed of a series of functions which are approximately periodic in r . The period of oscillations is given by $2\pi/|\vec{G}|$, where \vec{G} is a reciprocal-lattice vector. This period equals the perpendicular separation of those lattice planes labeled by \vec{G} . This leads us to the following geometrical interpretation for the periodic behavior: Consider a sphere of radius r centered at the donor site. As r increases the sphere intersects new lattice planes. The total number of points $L(r)$ enclosed by the sphere will show a sharp increase each time a new plane is intersected, and $N(r) = dL(r)/dr$ will show a corresponding peak. Thus, $N(r)$ will show oscillatory behavior with period given by the lattice plane spacing. In particular, the low-frequency oscillations in $N(r)$ result from lattice planes of high symmetry [(100), (110), etc.].

It is straightforward to numerically compute $N(r)$, where $N(r)dr$ is the number of acceptor sites located a distance between r and $r + dr$ from the donor site. At zero temperature, $N(r)$ will be a series of δ functions, one for each donor-to-acceptor shell. Experimentally, these discrete lines are broadened. To simulate this line broadening we replace each δ function by a Gaussian of width σ . The averaged number of sites $\bar{N}(r)$ is then computed by summing each Gaussian weighted by the number of sites in each shell. Figure 1 shows $\bar{N}(r)$ for a type-II spectrum in a zinc-blende lattice (donor and acceptor ions on different sublattices). For a broadening of $\sigma = 0.3$ Å the results are basically identical with those of Street and Wiesner.⁵ The approximately periodic behavior of $N(r)$ is clearly seen. For $\sigma = 0.8$ Å the period of

the oscillations as measured from Fig. 1 is 2.73 Å $= a_0/2$ where a_0 is the lattice constant. This period will be theoretically justified below.

Let us now derive an analytic form for $N(r)$. Consider a lattice composed of all possible acceptor sites. For simplicity, assume that this lattice has only one atom per unit cell. The acceptor sites are then specified by

$$\vec{T} = n_1 \vec{a}_1 + n_2 \vec{a}_2 + n_3 \vec{a}_3, \quad (1)$$

where \vec{a}_1 , \vec{a}_2 , and \vec{a}_3 are the primitive translation vectors and n_1 , n_2 , and n_3 run over all integer values. Let V_c denote the volume of the unit cell, and let the reciprocal-lattice vectors be labeled by \vec{G} . Let the donor position be specified by \vec{R}_d . The total number of lattice points enclosed by a sphere of radius r , centered at \vec{R}_d , can be expressed as

$$L(r, \vec{R}_d) = \sum_{\vec{T}} \Theta(r - |\vec{T} - \vec{R}_d|), \quad (2)$$

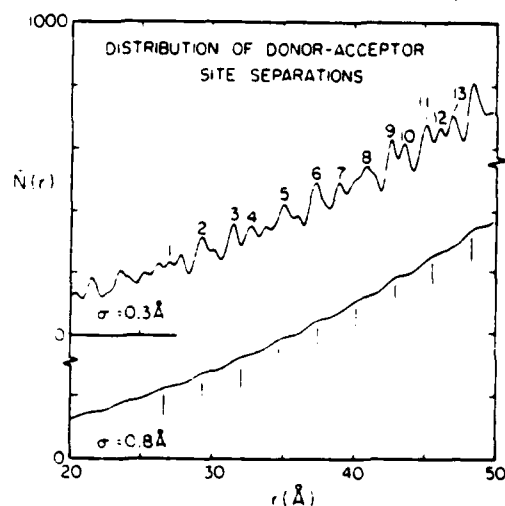


FIG. 1. Broadened distribution $\bar{N}(r)$ of acceptor sites located a distance r from donor site for (N, acceptor) pairs in GaP. Upper curve: $\sigma = 0.3$ Å broadening with the peaks labeled as in Ref. 5. Lower curve: $\sigma = 0.8$ Å broadening showing the lowest frequency oscillations with period 2.73 Å $= a_0/2$.

where Θ is a unit step function. The function $L(r, \bar{R}_d)$ is periodic in \bar{R}_d and so it can be expanded in a Fourier series,

$$L(r, \bar{R}_d) = \sum_{\bar{G}} c(\bar{G}) \exp(i\bar{G} \cdot \bar{R}_d) \quad (3)$$

Following Kendall and Rankin,⁶ the coefficients $c(\bar{G})$ are given by

$$\begin{aligned} c(\bar{G}) &= \frac{1}{V_c} \int_{\text{cell}} L(r, \bar{R}_d) \exp(-i\bar{G} \cdot \bar{R}_d) d\bar{R}_d \\ &= \frac{1}{V_c} \sum_{\bar{r}} \int_{\text{cell}} \Theta(r - |\bar{r} - \bar{R}_d|) \exp(-i\bar{G} \cdot \bar{R}_d) d\bar{R}_d \\ &= \frac{1}{V_c} \int_{|\bar{r}| \leq r} \exp(i\bar{G} \cdot \bar{r}) d\bar{r} \\ &= \frac{1}{V_c} \frac{4\pi r^2}{|\bar{G}|} j_1(|\bar{G}|r) \end{aligned}$$

where j_1 is a spherical Bessel function of the first kind. The distribution of acceptor sites located a distance r from the donor can now be evaluated to be

$$\begin{aligned} N(r) &= \frac{dL(r, \bar{R}_d)}{dr} \\ &= \frac{4\pi r^2}{V_c} \left(1 + \sum_{\bar{G} \neq 0} \frac{\sin(|\bar{G}|r)}{|\bar{G}|r} \exp(i\bar{G} \cdot \bar{R}_d) \right) \end{aligned} \quad (4)$$

It is clear from Eq. (4) that $N(r)$ is approximately periodic in r with frequencies given by $|\bar{G}|/2\pi$. Depending on the value of \bar{R}_d some frequencies may not be observed. In particular, if $\cos(\bar{G} \cdot \bar{R}_d) = 0$ then the frequency $|\bar{G}|/2\pi$ is forbidden. The above discussion can easily be generalized to include more than one type of acceptor site (i.e., more than one atom per unit cell in the lattice). $N(r)$ then contains a summation of the form Eq. (4) for each inequivalent type of acceptor site. Inequivalent donor sites can be handled in a similar manner. Finally, we note that the role of acceptors and donors in the above discussion can be interchanged and the results are the same.

These results can be applied to the problem of

GaP:(N, acceptor). The acceptor ions are located on a face-centered-cubic lattice with $V_c = a_0^3/4$ where $a_0 = 5.45 \text{ \AA}$ is the lattice constant. The frequencies of oscillation are found to be $\sqrt{3}/a_0$, $2/a_0$, $2\sqrt{2}/a_0$, ... The donor is located at $\bar{R}_d = a_0(\frac{1}{4}, \frac{1}{4}, \frac{1}{4})$ so that the frequency $\sqrt{3}/a_0$ is forbidden. Therefore, the lowest frequency will be $2/a_0$ as observed in the numerical calculation shown in Fig. 1 for $\sigma = 0.8 \text{ \AA}$. For a broadening of $\sigma = 0.3 \text{ \AA}$ some of the higher-frequency components are observed.

Now that we have a mathematical reason for the observed undulations, it is interesting to seek some simple geometrical interpretation of the results. From the form of Eq. (4) this interpretation is obvious. The reciprocal-lattice vectors label lattice plane in real space. The period of oscillation $2\pi/|\bar{G}|$ is simply equal to the perpendicular distance between lattice planes. Consider the number of lattice points contained in a sphere of radius r . As r increases, the sphere will intersect new lattice planes. Each time such an intersection occurs there will be a sharp increase in $L(r)$ and a corresponding peak in $N(r)$. Thus, the frequency $|\bar{G}|/2\pi$ is associated with those lattice planes labeled by \bar{G} . As a corollary, we note that those acceptor ions which contribute to the $|\bar{G}|/2\pi$ fluctuations in $N(r)$ will be concentrated around the directions from the donor which are parallel to \bar{G} .

In conclusion we have shown that the apparent periodicity of GaP:(N, acceptor) luminescence spectra is the result of long-range order in the crystal lattice. In principal the crystal symmetry could be deduced from the spectra, but in practice this may be difficult since it would require detailed knowledge of the relationship between luminescence energy and the donor-acceptor separation.

ACKNOWLEDGMENTS

This work was supported in part by the Office of Naval Research under Contract N00014-81-K-0305. One of us (R.M.F.) is the recipient of a postgraduate scholarship from the Natural Sciences and Engineering Research Council of Canada.

¹Reported by J. J. Hopfield, in *Proceedings of the International Conference on II-VI Semiconducting Compounds*, edited by D. G. Thomas (Benjamin, New York, 1968), p. 786.

²J. J. Hopfield, H. Kukimoto, and P. J. Dean, *Phys. Rev. Lett.* **27**, 129 (1971).

³T. N. Morgan, M. R. Lorenz, and A. Onton, *Phys. Rev. Lett.* **28**, 906 (1972).

⁴C. H. Henry and M. D. Sturge, *Bull. Am. Phys. Soc.* **18**, 415 (1973).

⁵R. A. Street and P. J. Wiesner, *Phys. Rev. Lett.* **34**, 1569 (1975).

⁶D. G. Kendall and R. A. Rankin, *Quart. J. Math. (Oxford)* **4**, 178 (1953).

Photoluminescence of Si-rich Si-Ge alloys

G. S. Mitchard and T. C. McGill

California Institute of Technology, Pasadena, California 91125

(Received 27 July 1981)

A detailed study of the photoluminescence spectrum of $\text{Si}_{1-x}\text{Ge}_x$ is presented for $x \approx 0.1$. Undoped and In-doped alloy samples are investigated. Spectral features are identified, and the effects of the disordered nature of the alloy on the luminescence spectrum are discussed. In particular, mechanisms for the observed broadening of bound-exciton luminescence are discussed, and the shift in alloy luminescence energy is obtained. At low temperatures a luminescence feature is observed which may result from recombination of excitons bound to local fluctuations in alloy composition.

I. INTRODUCTION

The properties of alloy semiconductors have been of general interest for some time. Such alloys provide a convenient system with which to experimentally and theoretically study the effects of disorder, which can be varied with alloy composition. The band gap can also be varied with alloy composition, and for this reason considerable effort has been directed towards the development of intrinsic and extrinsic alloy optoelectronic devices. The study of the luminescence properties of alloy semiconductors can provide useful and relatively easily interpreted information regarding the properties of the alloys and the consequences of their disordered nature. Most attention has been directed towards the III-V ternary alloys, where luminescence processes have been studied extensively.¹⁻³ Luminescence of II-VI ternary alloys has also been studied, most notably $\text{Hg}_{1-x}\text{Cd}_x\text{Te}$ (Ref. 4) where ir detector applications are particularly important.

Another alloy material of interest is the binary alloy $\text{Si}_{1-x}\text{Ge}_x$. The luminescence properties of $\text{Si}_{1-x}\text{Ge}_x$ are not particularly well known, although free- and bound-exciton,⁵ donor-acceptor,⁶ and electron-hole droplet⁷ recombination has been observed in Ge-rich alloys. In this paper we report the first detailed measurements of luminescence from Si-rich alloys, in particular alloys for which $x \approx 0.1$. Intrinsic and impurity-related luminescence is discussed, as well as certain properties of the luminescence which arise as a result of the compositional disorder of the alloy. In particular, we have been able to identify the luminescence features which result from free-exciton and bound-exciton recombination in the alloy. Also,

mechanisms for the observed bound-exciton luminescence broadening are discussed. Comparison of the luminescence energies from Si and the alloy samples results in values for the band-gap shift and free-exciton binding energy for the values of the composition parameter x which we were able to study. Finally, some evidence is presented which suggests that we observe at low temperatures luminescence which is the result of recombination of excitons bound to local fluctuations in alloy composition.

The remainder of this paper is organized in the following way. In Sec. II, we discuss the $\text{Si}_{1-x}\text{Ge}_x$ alloy samples studied, and the general features of the experimental technique. In Sec. III, the results of measurements on the undoped $\text{Si}_{1-x}\text{Ge}_x$ samples are presented and discussed. In Sec. IV, we consider the results obtained for one In-doped $\text{Si}_{1-x}\text{Ge}_x$ sample. In Sec. V, we discuss the general mechanisms for luminescence line broadening in the alloy, compare the alloy luminescence energies with those observed in Si, and consider the evidence for excitons bound to composition fluctuations. Finally, in Sec. VI, the results are summarized.

II. EXPERIMENTAL CONSIDERATIONS

A. Si-Ge alloy samples

In this paper, we present measurements of the photoluminescence properties of three $\text{Si}_{1-x}\text{Ge}_x$ samples, two of which were not intentionally doped and the third of which was doped with In. The crystals were grown by the Czochralski technique.

Impurity concentrations and alloy compositions were determined at Hughes Research Laboratories, where the crystals were grown. Impurity concentrations were established on the basis of Hall-effect measurements. These measurements show that residual concentrations of B and P impurities are present in all the samples. Alloy compositions were obtained from a variety of techniques; results of the electron microprobe, density, and x-ray diffraction measurements were in excellent agreement. The samples studied, their impurity concentrations, and their alloy compositions are given in Table I.

B. Experimental technique

The Si-Ge alloy samples described above were mechanically etched, and then mounted in a Janis variable-temperature cryostat. The luminescence resulted from above band-gap optical excitation by a Spectra-Physics Model 166 Ar⁺ laser, which could be operated in pulsed or cw mode. The luminescence was collected from the edge of the sample, wavelength-analyzed with a Spex Model 1269 spectrometer, and detected with an RCA 7102 S-1 photomultiplier cooled to liquid-nitrogen temperature. The photomultiplier output was processed with standard photon-counting electronics, acquired on a Nuclear Data ND-60 multichannel analyzer, and finally passed to a PDP 11/34 computer for analysis and storage.

III. EXPERIMENTAL RESULTS AND DISCUSSION FOR UNDOPED Si_{1-x}Ge_x

In this section, the results of the application of the photoluminescence technique to the undoped samples are considered. Two undoped Si_{1-x}Ge_x samples were available, C077 ($x=0.11$) and C021-3 ($x=0.067$). As indicated in Table I, these samples

have low residual concentrations of B and P impurities, in spite of not being intentionally doped.

A. Typical photoluminescence spectrum and identification of phonon replicas

A typical low-temperature photoluminescence spectrum of sample C077 is shown in Fig. 1. Two broad features are visible at the high-energy end of the spectrum and are labeled FE (free exciton) and BE_P (bound exciton). Replicas of these lines, labeled FE(TO) and BE_P(TO), are observed approximately 58 meV lower in energy. Since this is the transverse-optical (TO) phonon energy in Si, the low-energy lines are interpreted as being due to TO phonon replicas of the higher-energy lines.

B. Identification of free-exciton luminescence

In this section we consider the effect of increasing the sample temperature on the photoluminescence spectrum of sample C077. In Fig. 2 we see that as the temperature is increased the line labeled BE_P thermalizes with respect to the line labeled FE. Above 10 K (Fig. 3), the line labeled BE_P is no longer visible, and the line labeled FE assumes a shape characteristic of free-exciton (FE) recombination in Si. In intrinsic Si, FE recombination luminescence has been fitted very accurately with a line shape,⁸

$$I(E) \propto \sqrt{E - E_0} \exp \left[\frac{E - E_0}{k_B T} \right], \quad (1)$$

where $I(E)$ is the luminescence intensity at photon energy E , E_0 is the FE threshold energy, and T is the temperature. In this expression we assume parabolic FE bands and a Boltzmann distribution of FE center-of-mass kinetic energies. The high-temperature luminescence from sample C077 can

TABLE I. Si_{1-x}Ge_x alloys studied using photoluminescence. The samples were grown and characterized at Hughes Research Laboratories.

Sample	N_B (cm ⁻³)	N_P (cm ⁻³)	x N_{In} (cm ⁻³)	Electron microprobe	Density	X-ray diffraction
C077	3.6×10^{13}	2.8×10^{13}		0.1115	0.113	0.113
C021-3	2.3×10^{14}	4.1×10^{14}		0.0677	0.0685	
C093	5.0×10^{13}	5.3×10^{14}	2.5×10^{16}			0.104

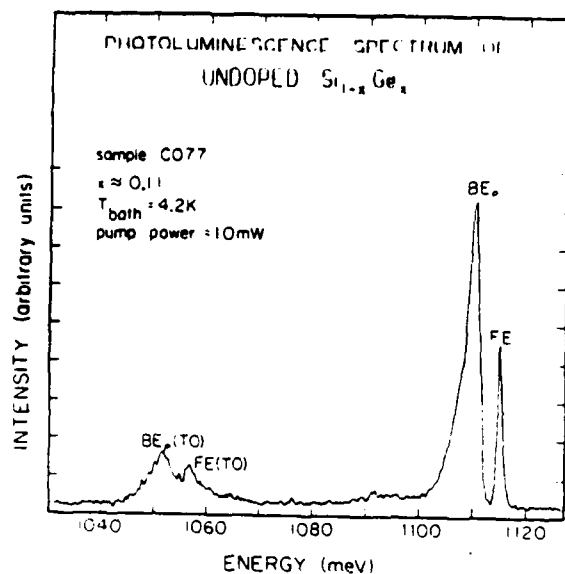


FIG. 1. Typical photoluminescence spectrum of undoped $\text{Si}_{1-x}\text{Ge}_x$ sample C077. Refer to the text for an explanation of the line assignments.

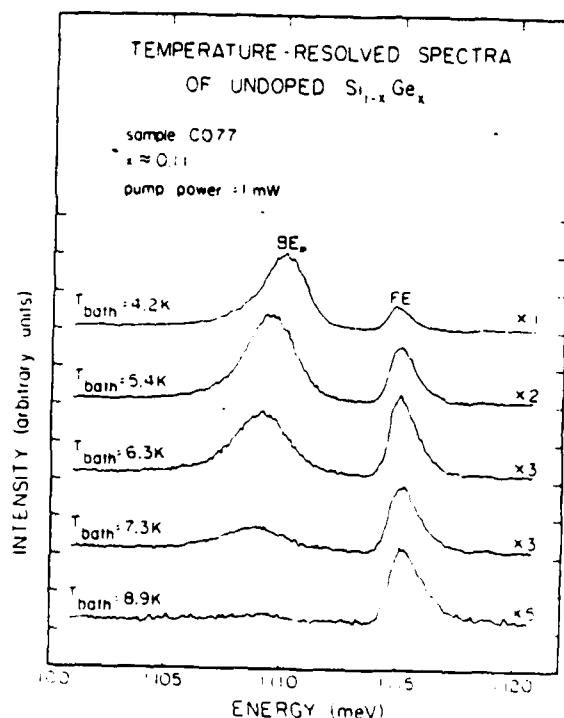


FIG. 2. Temperature-resolved spectra of undoped $\text{Si}_{1-x}\text{Ge}_x$ sample C077 from 4.2 to 8.9 K. The scale factors (e.g., $\times 2$) give the relative intensity magnification. Note that thermalization of the line labeled BE_p is observed. In addition, the BE_p peak position shifts to lower energy as the temperature is increased. At high temperatures, the luminescence of the line labeled FE assumes a shape characteristic of free-exciton luminescence in Si.

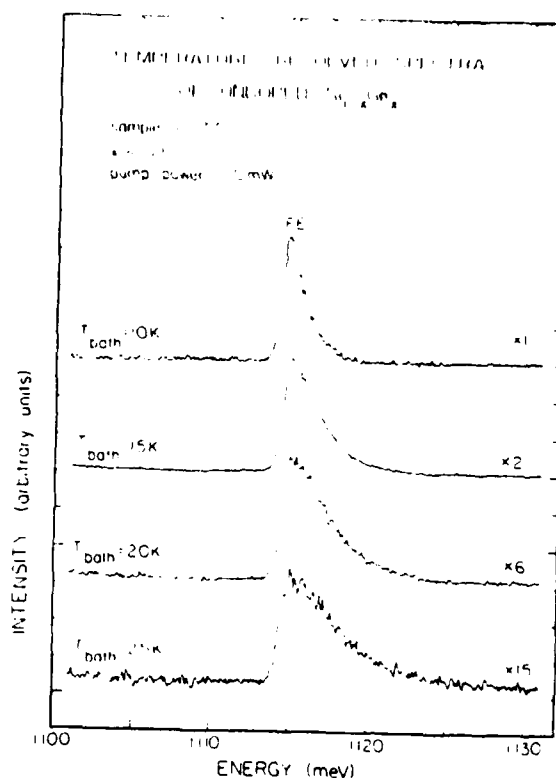


FIG. 3. Temperature-resolved spectra of undoped $\text{Si}_{1-x}\text{Ge}_x$ sample C077 from 10 to 25 K. The scale factors (e.g., $\times 2$) give the relative intensity magnification. Note that, at these temperatures, the luminescence of the line labeled FE assumes a shape characteristic of free-exciton luminescence in Si.

also be fitted very well with the line shape described by Eq. (1). An example of this fit is shown in Fig. 4. In all cases, the fit temperature obtained in this manner was within 1 K of the measured bath temperature. Also, the threshold energy remained constant within 0.05 meV. On the basis of this analysis, the line labeled FE is identified as resulting from no-phonon (NP) FE recombination. Note that this intrinsic NP luminescence is greatly enhanced in the alloy, since the Ge atoms can act as momentum-conserving scattering centers.⁵

C. Identification of bound-exciton luminescence

The identification of the FE line obtained in the preceding section, splitting between the FE threshold and the peak position of the line labeled BE_p , and the thermal behavior shown in Fig. 2, suggest that the line labeled BE_p is due to the NP recom-

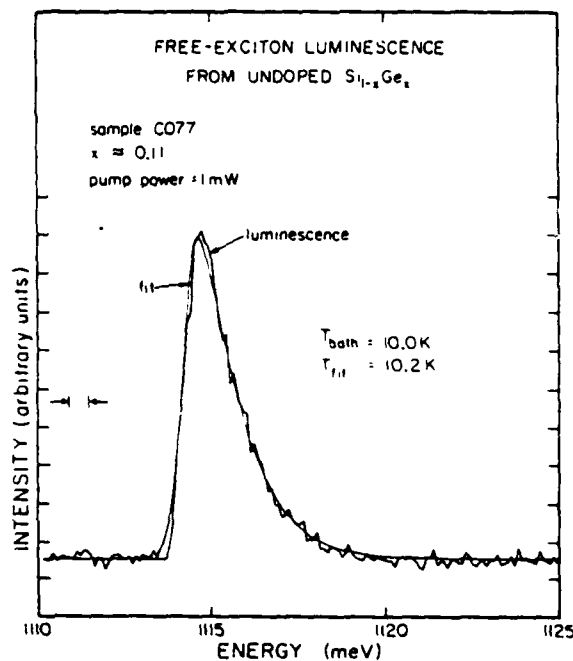


FIG. 4. Free-exciton luminescence from undoped $\text{Si}_{1-x}\text{Ge}_x$ sample C077 and least-squares fit of the theoretical line shape [Eq. (1)]. The sample temperature obtained as a result of the fit T_{fit} is shown with the measured bath temperature T_{bath} .

bination of excitons bound by about 4 meV to a shallow level. The pump-power dependence at low power shown in Fig. 5 supports this proposal. As this figure demonstrates, the FE to BE_p luminescence intensity ratio is independent of pump power.

Candidates for such a level are clearly B and P, which have binding energies in the neighborhood of 4 meV in Si (3.9 and 4.7 meV, respectively⁸), and which are the most common shallow impurities in the undoped material. Photoluminescence measurements of Si containing approximately equal background concentrations of B and P show that P bound-exciton (BE_p) luminescence is more intense than B bound-exciton (BE_B) luminescence in the NP region by at least an order of magnitude. It seems reasonable to conclude, therefore, that the line labeled BE in the luminescence from sample C077 is primarily due to NP BE_p recombination.

The high-power pump-power dependence presented in Fig. 6 supports this conclusion. In undoped Si, low-energy lines due to bound-multiexciton complexes (BMEC) appear as the pump power is increased. The splitting between the BE_p line and the first BMEC line is 2.2 meV for B and 3.6 meV for P.⁹ As shown in Fig. 6, in the luminescence spectrum of sample C077 the

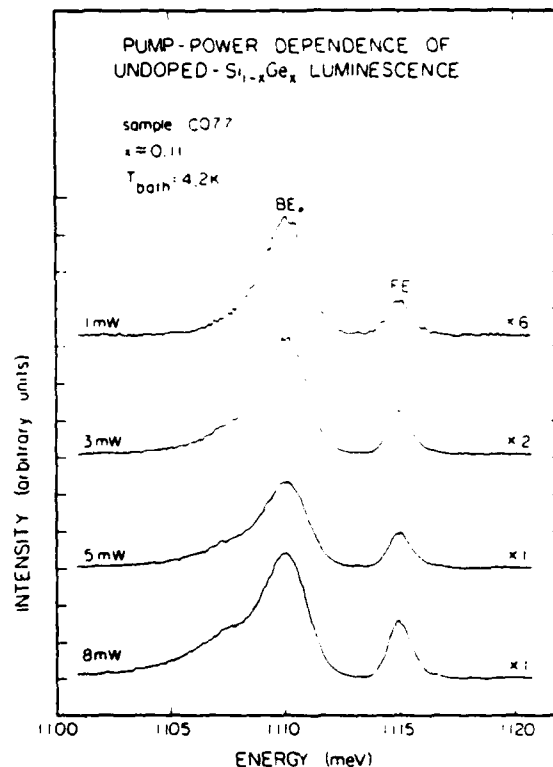


FIG. 5. Pump-power dependence of the luminescence from undoped $\text{Si}_{1-x}\text{Ge}_x$ sample C077 at low pump powers. The scale factors (e.g., $\times 6$) give the relative intensity magnification. Note that the BE_p to FE luminescence intensity ratio is independent of pump power at these power levels.

BE_p line develops a low-energy shoulder as the pump power is increased, which resolves into a separate line at high pump powers. The separation between this line and the BE_p line is about 3.8 meV, which is consistent with the splitting between the P BE and first BMEC in Si. Since no line is observed which would correspond to B BMEC luminescence, our conclusion regarding the origin of the BE_p line in the alloy seems justified.

D. Comparison of photoluminescence spectra

The interpretation of the photoluminescence spectrum of sample C077 developed in the previous sections is consistent with our investigation of the $x = 0.067$ sample, C021-3. In Fig. 7, the luminescence spectra of samples C077 and C021-3 are compared. We see that the ratio of BE_p to FE luminescence is considerably greater for sample C021-3. This is consistent with Table I, which in-

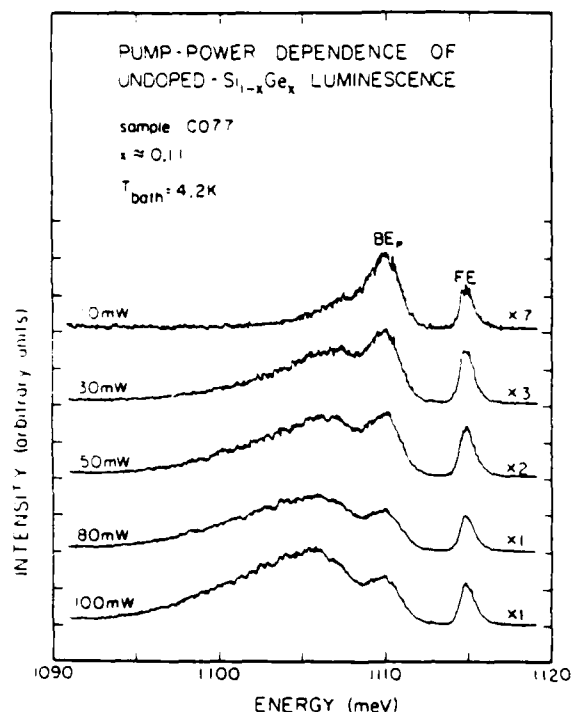


FIG. 6. Pump-power dependence of luminescence from undoped $\text{Si}_{1-x}\text{Ge}_x$ sample C077 at high pump powers. The scale factors (e.g., $\times 7$) give the relative intensity magnification. Note the new feature which appears on the low-energy side of the BE_p line at high pump powers. This feature is discussed in the text.

icates that impurity concentrations in sample C021-3 are approximately an order of magnitude higher. In addition, we see that the luminescence spectrum of sample C021-3 is shifted to higher energy. This feature will be discussed in detail below.

IV. EXPERIMENTAL RESULTS AND DISCUSSION FOR In-DOPED $\text{Si}_{1-x}\text{Ge}_x$

The subject of the investigations reported in this section was the In-doped $\text{Si}_{1-x}\text{Ge}_x$ sample C093, for which $x = 0.10$.

A. Typical photoluminescence spectra

Typical luminescence spectra obtained from $\text{Si}_{1-x}\text{Ge}_x$. In sample C093 are shown in Fig. 8. Spectra measured at various temperatures are shown. Two features are prominent in the spectra. The higher-energy luminescence, labeled FE, be-

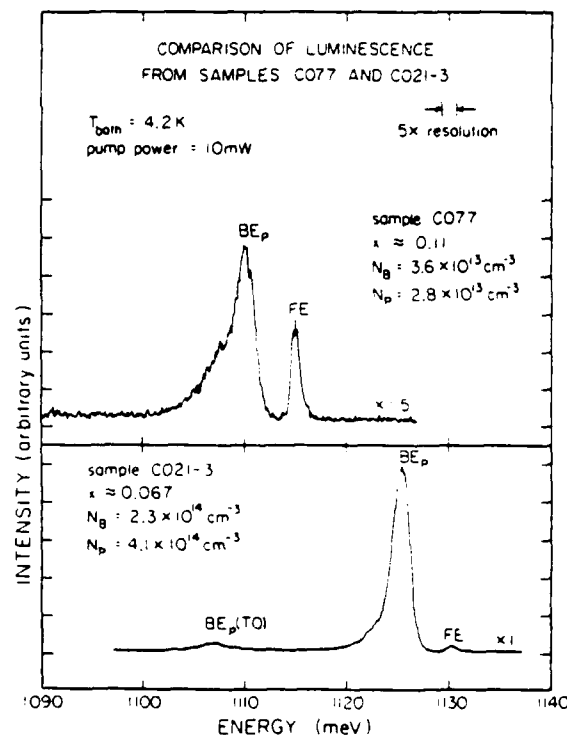


FIG. 7. Comparison of the luminescence spectra of samples C077 and C021-3. The scale factors (e.g., $\times 1.5$) give the relative intensity magnification. Note that BE_p luminescence is much more intense from sample C021-3 than from sample C077. Also, note that the luminescence from sample C021-3 is at higher energy than the luminescence from sample C077. These features are discussed in the text.

comes visible only at high temperatures. At somewhat lower energies a broad feature labeled L is visible, which moves to lower energy as the temperature is increased. The L luminescence develops a low-energy shoulder at high temperatures, which has been labeled $\text{FE}(\text{TO})$.

B. Identification of free-exciton luminescence

To begin with, we note that the luminescence labeled FE has a line shape and temperature dependence characteristic of NP FE recombination in Si, as described in detail in Sec. III. Equation (1), which describes the NP FE line shapes, can be fitted to the FE luminescence from sample C093 very accurately. The FE threshold energy obtained from such fits, 1115.8 meV, remained constant within about 0.3 meV. However, the fit temperatures T_{fit} were systematically higher than the mea-

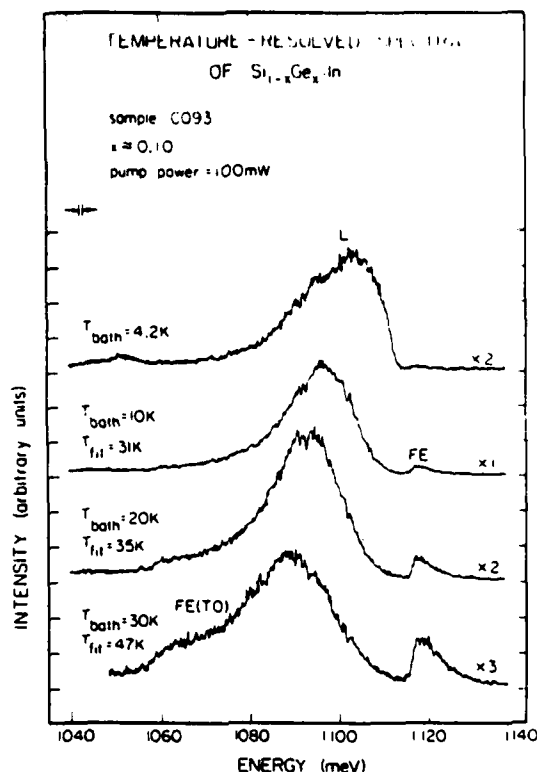


FIG. 8. Temperature-resolved spectra of $\text{Si}_{1-x}\text{Ge}_x\text{:In}$ sample C093 from 4.2 to 30 K. The scale factors (e.g., $\times 2$) give the relative intensity magnification. Refer to the text for a discussion of the line assignments shown in the figure. Where FE luminescence is observed, the sample temperature obtained from a least-squares fit to the FE line shape, T_{fit} , is shown with the measured bath temperature T_{bath} . The discrepancy between these results is discussed in the text.

sured bath temperatures T_{bath} . These temperatures are indicated in Fig. 8. It seems, therefore, that either the FE luminescence is subject to some broadening as a result of the disordered nature of the alloy, or the sample is being locally heated by the laser pump. Of these two possibilities, the second seems most likely. First, one would expect some broadening mechanism to affect the FE threshold behavior as well as generally broaden the line. That is, we would expect to see the FE threshold "smear out" and become less abrupt. However, this behavior is not observed. As previously mentioned, the line shape is described by Eq. (1) very well. Second, as indicated in Table I sample C093 has impurity concentrations which are about 3 orders of magnitude higher than those in sample C077. As a result, much higher pump powers are needed to observe FE luminescence at all in sample C093. At these laser intensities, sam-

ple heating must be considered a very likely cause of the observed FE broadening.

If this explanation is accepted, the luminescence labeled FE can be interpreted as resulting from NP-FE recombination in the $\text{Si}_{1-x}\text{Ge}_x\text{:In}$ alloy. Since the feature labeled FE(TO) is separated from the FE peak by approximately the Si TO phonon energy, we interpret this shoulder on L as being due to TO phonon-assisted FE recombination.

C. Identification of bound-exciton luminescence

Our interpretation of the luminescence labeled L is necessarily considerably more complicated than that of the FE luminescence. There are a number of processes which are undoubtedly contributing to the L line. Primarily, BE_B , BE_P , and BE_{In} luminescence must be considered. Indium, of course, is the majority dopant, and will dominate the NP-BE luminescence. The B concentration is about an order of magnitude greater than the P concentration. It follows from our discussion of BE luminescence from undoped $\text{Si}_{1-x}\text{Ge}_x$ that B and P will probably contribute equally to the NP-BE luminescence. In addition, the L luminescence is sufficiently broad that transverse-acoustic (TA) phonon replicas of the FE and BE lines may contribute as well. It is unlikely that NP-BMEC or electron-hole-droplet (EHD) luminescence will have any significant influence on the spectra presented here. The impurity concentrations in sample C093 preclude the observation of such effects at the pump powers utilized in this study.

1. Time-resolved spectra and isolation of B bound-exciton component

In an effort to separate the BE components which produce the L luminescence, the time evolution of the luminescence from sample C093 was measured at low pump power. The time-resolved spectra are shown in Fig. 9 for low-power laser excitation. As this figure demonstrates, the L luminescence is composed of a relatively sharp high-energy component with a long lifetime, and a broad low-energy component with a short lifetime. Consideration of the BE_B , BE_P and BE_{In} decay times in Si (1055, 272, and 2.7 nsec, respectively¹⁰) leads to the suggestion that the sharp, long-lifetime component is primarily a result of BE_B recombination. The broad, short-lifetime, low-energy shoulder is therefore probably due to BE_{In} recombination.

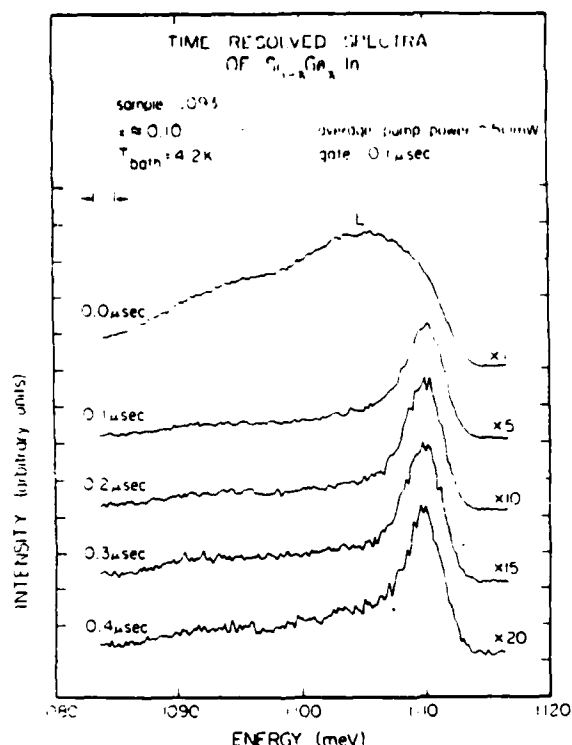


FIG. 9. Time-resolved spectra of $\text{Si}_{1-x}\text{Ge}_x\text{In}$ sample C093. The scale factors (e.g., $\times 5$) give the relative intensity magnification. At long times, a sharp, long-lifetime component of L luminescence is isolated.

2. Temperature-resolved spectra and isolation of In bound-exciton component

A further separation of the BE components which produce the L luminescence can be accomplished by measuring the temperature dependence of the photoluminescence spectrum. This measurement is shown in Fig. 8. We see that the high-energy side of the L luminescence thermalizes as the temperature is increased. This observation is consistent with the interpretation of L luminescence presented in the previous section. At high temperatures, only the lower-energy BE_{In} component is observed. The higher-energy BE_{B} component has thermalized.

This effect is seen clearly in Fig. 10, which shows the temperature dependence of L luminescence which is gated in time. At low temperatures, the BE_{B} peak is reasonably well isolated. At the high pump powers used for this measurement, however, a low-energy shoulder is clearly observed. We interpret this shoulder as being due to a BE_{In} component which has not been eliminated by the time resolution. As the temperature is increased,

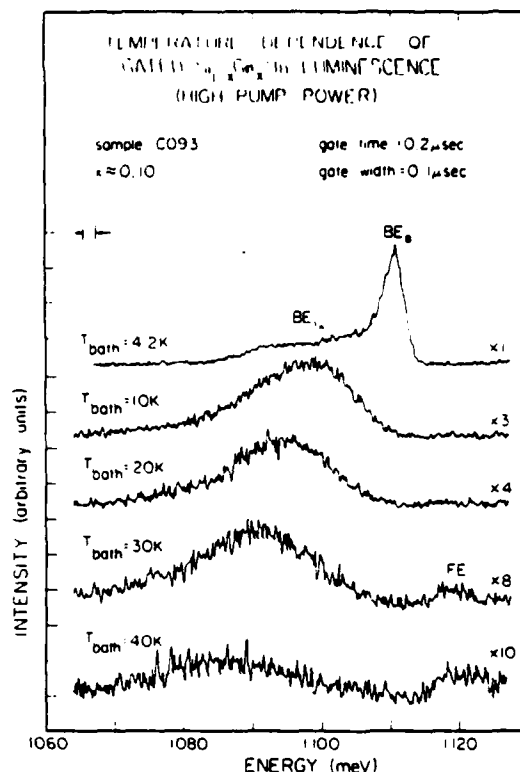


FIG. 10. Gated, temperature-resolved spectra of $\text{Si}_{1-x}\text{Ge}_x\text{In}$ sample C093 at high pump power. The scale factors (e.g., $\times 3$) give the relative intensity magnification. At high temperature, the BE_{B} luminescence component thermalizes, and the BE_{In} component is isolated. At high temperatures, weak FE luminescence is also observed.

we see the BE_{B} component thermalize with respect to the BE_{In} component. Above 10 K, only the BE_{In} component remains.

There is one difficulty with this interpretation which should be mentioned. As the temperature is raised above 10 K, the BE_{In} component peak position moves to lower energy, as expected from the behavior of BE_{p} luminescence in undoped $\text{Si}_{1-x}\text{Ge}_x$. This effect is observed in Fig. 8 and Fig. 10. However, the BE_{In} peak moves too far; at 30 K, it is already approximately 25 meV below the FE threshold, while the BE_{In} binding energy in Si is only 13.7 meV.¹¹ In spite of this, the bulk of the experimental evidence supports the interpretation that this high-temperature luminescence is due to BE_{In} recombination in the alloy. It may be that contributions from FE and BE TA-assisted luminescence combine to produce the anomalously low high-temperature BE_{In} peak position. However, this seems unlikely when the relative intensities of TA and NP luminescence in Si are considered.

It is also possible that the high-temperature BE_{in} binding energy in the alloy is increased as a result of some complicated effect which may involve the unusually large radii of the Ge and In atoms relative to the Si—Si bond length. Of course, this mechanism is also unlikely, practically by definition. Unfortunately, all we can state at this point is that the anomalous temperature dependence of the BE_{in} luminescence remains unexplained.

V. DISCUSSION

In the previous sections, we have presented the experimental photoluminescence data for the undoped and In-doped Si-Ge alloy samples, and have attempted to interpret the spectra qualitatively. In this section, we continue our qualitative discussion of the experimental results. In particular, we focus on some effects which result from the compositional disorder of the alloy.

A. Bound-exciton line broadening

To begin with, we see that the BE line is considerably broadened in the alloy. In fact, the BE line in the undoped $Si_{1-x}Ge_x$ samples is approximately ten times broader (~ 3 meV) than its counterpart in Si (~ 0.4 meV). In general, this broadening can be accounted for on the basis of the compositional inhomogeneity of the alloy material. The energy of the luminescence which results from the recombination of an exciton bound to a particular impurity will depend on the local configuration of Si and Ge atoms. This luminescence energy can be schematically written as

$$E_{PL}(\{c\}) = E_G(\{c\}) - E_{FE}(\{c\}) - E_{BE}(\{c\}), \quad (2)$$

where E_{PL} is the photon energy, E_G is the band-gap energy, E_{FE} is the free-exciton binding energy, and E_{BE} is the bound-exciton binding energy, and where $\{c\}$ denotes the particular configuration for the impurity being considered.

We can consider two simple limits to the general expression, Eq. (2). First, we assume that the local configuration does not affect the free-exciton binding energy or bound-exciton binding energy. Then Eq. (2) indicates that the BE-line broadening is the result of variations in band-gap energy produced by local fluctuations in the alloy composition x . This limit was first discussed by Alferov *et al.*¹²

We can roughly estimate this effect on the basis of the following argument. Given a volume $4\pi a^3/3$, there will be $4\pi a^3 \propto N/3$ atoms, where N is the density of lattice sites in the alloy, if the Ge atoms are distributed randomly the typical fluctuation in the number of Ge atoms in the volume will be $(4/3\pi a^3 x N)^{1/2}$. Therefore, the typical fluctuation in the composition parameter x will be

$$\Delta x \sim \frac{(\frac{4}{3}\pi a^3 x N)^{1/2}}{\frac{4}{3}\pi a^3 N} = \left[\frac{x}{\frac{4}{3}\pi a^3 N} \right]^{1/2}. \quad (3)$$

If $\Delta E = \alpha \Delta x$, where ΔE is the change in gap energy produced by a change in composition Δx , then Eq. (3) becomes

$$\Delta E \sim \alpha \left[\frac{x}{\frac{4}{3}\pi a^3 N} \right]^{1/2}. \quad (4)$$

N can be estimated for the alloy from the lattice-constant measurements of Dismukes *et al.*¹³ For $x=0.1$, we find $N \sim 6 \times 10^{21} \text{ cm}^{-3}$. From the absorption measurements of Braunstein *et al.*,¹⁴ we can estimate $\alpha \sim 600$ meV. Assuming that a is approximately an exciton Bohr radius in Si, i.e., about 40 Å, we obtain $\Delta E \sim 5$ meV, which is reasonable agreement for a crude calculation.

In spite of the agreement, this limit does not explain the temperature-dependence data presented in Figs. 2 and 8. The data clearly shows that the BE peak shifts to lower energy as the temperature increases. However, the band-gap fluctuation limit does not produce this behavior. In this limit, we expect that as the temperature increases excitons will thermalize to bound-exciton states in the regions where the band gap is larger, which produces a BE peak which moves to higher energy.

The second limit to Eq. (2) we will consider accounts for the observed temperature dependence. In this limit, we assume that the local configuration does not affect the band-gap energy or the FE binding energy. We assume that the gap energy and the FE binding energy are the bulk average values for the alloy. Then the BE line broadening is the result of variations in the BE binding energy caused by variations in the local configuration of Si and Ge atoms. It is possible, therefore, that the BE line is composed of several overlapping luminescence lines from BE's with slightly different binding energies. These binding energies will increase, in principle, from the BE binding energy in Ge to the BE binding energy in Si.

Qualitatively, this limit produces the temperature dependence observed in Figs. 2 and 8. At low

temperatures, we see luminescence from all BE's. As the temperature increases, though, we expect that luminescence from the most tightly bound BE's will dominate. As we have previously mentioned, these BE's will have the most Si-like local configuration. In addition to explaining the temperature-dependence data, this picture of BE-line broadening is consistent with time-resolved spectra of the alloy luminescence. An analysis of the relevant decay times shows that the decay of all components of BE luminescence is capture-limited in the cases studied here.¹⁵ This is consistent with our observation that all components of the BE line decay at the same rate — the line shape does not change and the peak position remains fixed.

B. Comparison of Si and Si-Ge luminescence energies

If we assume that, at high temperatures, the BE luminescence is dominated by components which have the most Si-like local configuration, then a procedure for directly comparing Si and $\text{Si}_{1-x}\text{Ge}_x$ luminescence energies presents itself. We propose that the difference in recombination energy between the high-temperature BE-peak position in the Si-Ge alloy and the corresponding BE-peak position in Si is just due to the shift in band gap of the alloy.

Figure 11 schematically illustrates the consequences of this proposal for the $x=0.11$ $\text{Si}_{1-x}\text{Ge}_x$ sample, C077. The high-temperature BE_P luminescence line position, 1108.71 meV, was obtained from the 8.0-K spectrum. This was the highest temperature at which BE_P luminescence could be reliably observed, and it was assumed that the luminescence was dominated by recombination of BE_P's in essentially a Si environment. The P luminescence line position in Si, 1150.11 meV, was obtained from direct measurement of lightly doped Si:P. If this change in line position is attributed solely to a change in gap energy, these measurements imply a band-gap decrease of 41.4 meV for $x=0.11$. This value fluctuated by about 0.6 meV due to large-scale inhomogeneities in the crystals being examined. If a rough graphical extrapolation of the absorption data published by Braunstein *et al.*¹⁴ is attempted, we obtain an alloy band-gap shift of approximately 60 meV for $x=0.11$, which is in reasonable agreement with the luminescence data.

SCHEMATIC COMPARISON OF UNDOPED Si AND UNDOPED $\text{Si}_{1-x}\text{Ge}_x$ LUMINESCENCE ENERGIES

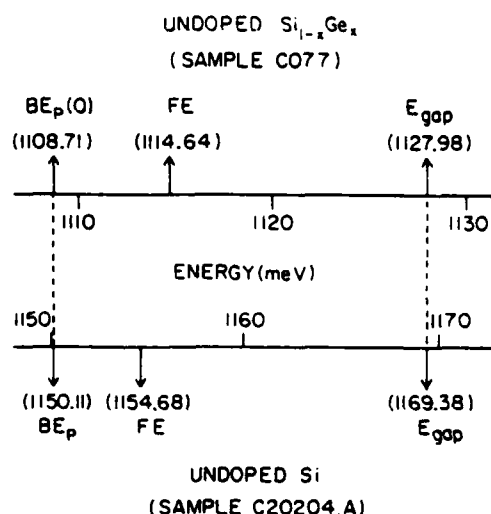


FIG. 11. Schematic line-position comparison between Si and $\text{Si}_{1-x}\text{Ge}_x$ sample C077. This comparison is based on the assumption that the difference between the energy of high-temperature BE_P alloy luminescence is equal to the difference in band-gap energies for Si and $\text{Si}_{1-x}\text{Ge}_x$ sample C077. This fixes the alloy gap energy. The spectra are then compared by lining up the Si and $\text{Si}_{1-x}\text{Ge}_x$ gap energies.

In addition to the high-temperature $\text{Si}_{1-x}\text{Ge}_x$ BE_P line position and the Si BE_P line position, Fig. 11 also shows the FE threshold and E_{gap} positions for Si and the $x=0.11$ alloy. The FE threshold position in the alloy, 1114.64 meV, was obtained by fitting Eq. (1) to the high-temperature FE luminescence spectra (Fig. 3), as illustrated in Fig. 4. The NP-FE threshold position in Si, 1154.68 meV, was obtained by fitting Eq. (1) directly to NP-FE luminescence from pure Si. The Si gap energy, 1169.38 meV, was determined from the NP-FE threshold energy by adding the FE binding energy, which is 14.7 meV. Then the alloy gap energy, 1127.98 meV, was obtained by subtracting the band-gap shift, 41.4 meV, from the Si gap energy.

As indicated in Fig. 11, this method implies that the FE dissociation energy in the $x=0.11$ alloy has decreased by 1.36 meV from its value in Si, to 13.34 meV. This compares favorably with a rough estimate based on a linear interpolation between the FE dissociation energies in Si and Ge, which are 14.7 and 4.15 meV, respectively. The linear in-

terpolation results in an estimate of 13.54 meV for the FE dissociation energy in the $x=0.11$ alloy.

A similar analysis has been applied to the $x=0.067$ sample, C021-3. As shown in Fig. 7, compared to sample C077 the luminescence from sample C021-3 is shifted to higher energy by 15.5 meV. This implies a band-gap decrease of 25.9 meV for the $x=0.067$ alloy. This result and the result previously obtained for sample C077 are consistent with the alloy-composition measurements presented in Table I if a linear relationship between the alloy composition and change in band gap is assumed. The composition ratio between the two samples is 0.609 while the ratio of the measured band-gap shifts is 0.626.

To compare the Si and $\text{Si}_{1-x}\text{Ge}_x$ luminescence energies for the In-doped sample, C093, we note that samples C077 and C093 differ in composition by only about 1%. We therefore assume that the FE binding energies in the two samples are the same. This leads to the comparison schematically illustrated in Fig. 12. The gap energy for sample C093, 1129.14 meV, was determined by adding the assumed FE binding energy, 13.34 meV, to the FE

threshold energy, 1115.8 meV. This results in a measured band-gap shift of 40.2 meV for the $x=0.104$ alloy. The band-gap shifts and alloy-composition measurements are reasonably consistent, assuming a linear relationship between the alloy composition and change in band gap. The composition ratio between samples C077 and C093 is 0.920 while the ratio of measured band-gap shifts is 0.971. Samples C021-3 and C093 agree exactly — the composition ratio and the ratio of measured band-gap shifts are both 0.644.

C. Excitons bound to composition fluctuations

One feature in the luminescence spectrum of sample C077 remains to be discussed. At high temperatures (Fig. 3), the FE line assumes a shape characteristic of FE recombination in Si and is well described by Eq. (1), as previously discussed. The FE threshold energy obtained by fitting Eq. (1) is independent of temperature, as expected. However, at low temperatures this is no longer the case. Spectra taken at various temperatures below 6 K are shown in Fig. 13. We see that as the temperature decreases, the line shifts to lower energy and assumes a shape which is no longer characteristic of FE recombination.

These measurements of low-temperature FE luminescence suggest that a low-energy shoulder appears on the FE luminescence at low temperatures. This shoulder may be due to the recombination of excitons bound by only about 0.1 meV to a very shallow level. This interpretation is supported by the temperature-resolved spectra, which show that the shoulder has completely thermalized by 6 K. Above 6 K, Eq. (1) correctly describes the line shape, and the threshold energy is independent of temperature. This behavior is consistent with a binding energy of tenths of meV. Also, the pump-power dependence at 1.6 K (Fig. 14) shows that the FE to BE_p intensity ratio is independent of pump power, as expected for independent exciton-binding centers in the absence of saturation.

These features, and the fact that there is no known defect or impurity in Si which binds an exciton by only 0.1 meV, leads us to suggest that the new feature may be due to the recombination of excitons weakly bound to local fluctuations in the alloy composition (BE_f). The possibility of such a state was first pointed out by Baranovskii and Efros,¹⁶ who extended the bulk fluctuation theory of Alferov *et al.*¹² to include excitons. A line

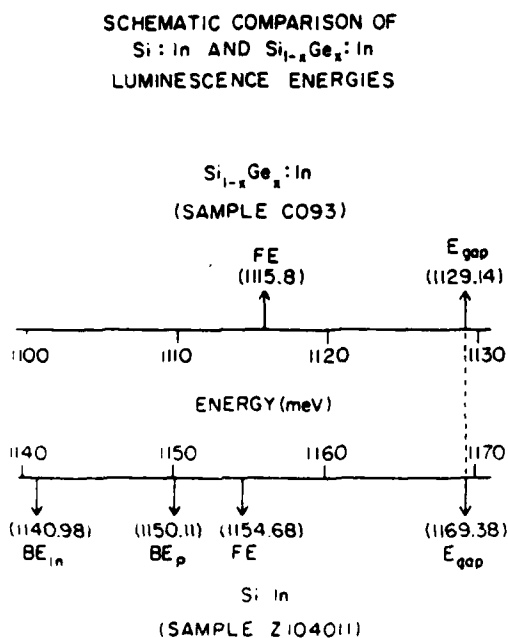


FIG. 12. Schematic line-position comparison between Si and $\text{Si}_{1-x}\text{Ge}_x$:In sample C093. This comparison is based on the assumption that the FE binding energy in sample C093 and sample C077 is identical. This fixes the alloy gap energy. The spectra are then compared by lining up the Si and $\text{Si}_{1-x}\text{Ge}_x$:In gap energies.

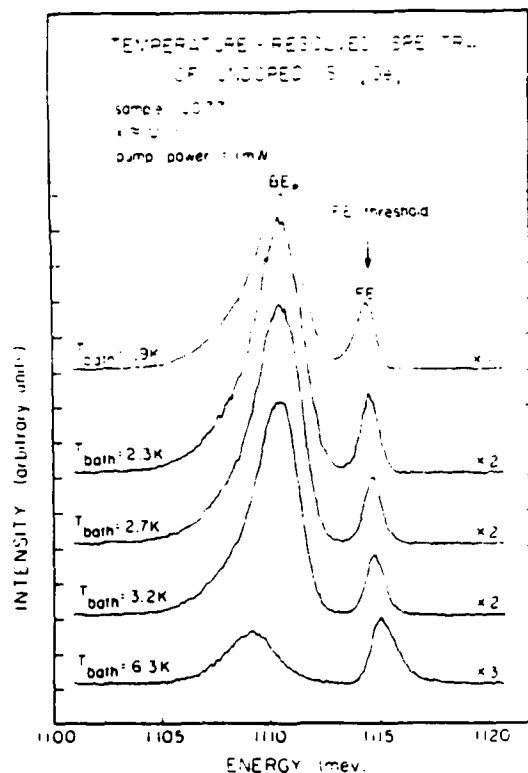


FIG. 13. Temperature-resolved spectra of undoped $\text{Si}_{1-x}\text{Ge}_x$ sample C077 at low temperatures. The scale factors (e.g., $\times 2$) give the relative intensity magnification. Note that the free-exciton line shifts and broadens as the temperature is decreased. For reference, the free-exciton threshold energy measured at high temperature is shown.

which may be due to fluctuation bound excitons has just recently been reported in $\text{GaAs}_{1-x}\text{P}_x$,¹⁷ and has characteristics which are similar to those of the line reported here.

One of the most important features of this model is the prediction that BE_F luminescence should have a very long lifetime. As indicated during the discussion of BE_P decay, the dominant decay mechanism for donor or acceptor BE 's in Si is the Auger process. This results in observed decay rates which can be orders of magnitude larger than the radiative rates obtained from measured oscillator strengths.^{10,18} For instance, the BE_P radiative decay rate is estimated to be $5 \times 10^2 \text{ sec}^{-1}$, whereas the observed Auger decay rate is $3.7 \times 10^6 \text{ sec}^{-1}$.¹⁰ When an exciton is bound to a local composition fluctuation, however, the Auger

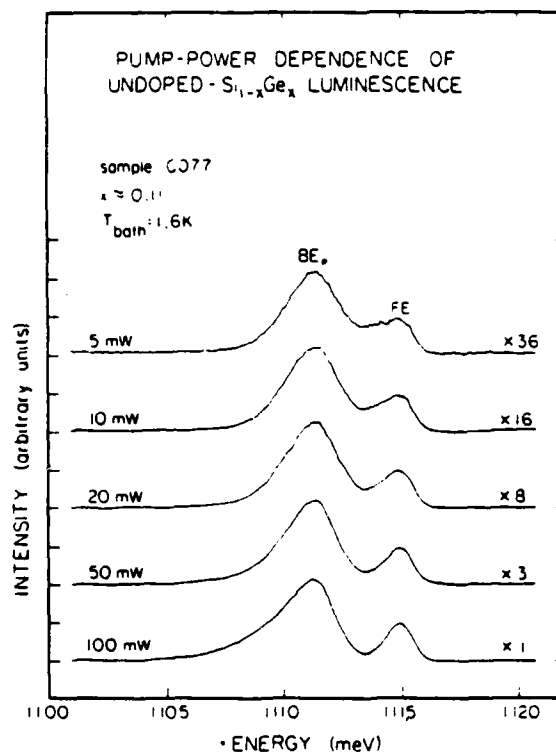


FIG. 14. Pump-power dependence of luminescence from undoped $\text{Si}_{1-x}\text{Ge}_x$ sample C077 at 1.6 K. The scale factors (e.g., $\times 36$) give the relative intensity magnification. Note that the BE_F -FE intensity ratio is independent of pump power.

process is not possible and long-lifetime luminescence is expected. Indeed, this was the case for the luminescence feature observed in $\text{GaAs}_{1-x}\text{P}_x$.¹⁶

Figure 15 presents the best low-temperature time-resolved spectra available for the $\text{Si}_{0.9}\text{Ge}_{0.1}$ alloy. Although the spectra are somewhat noisy, we see that the BE_F luminescence does not appear to have a particularly long lifetime compared to the BE_P luminescence line. This apparent discrepancy can be investigated by estimating the relevant decay times. These estimates show that in this case we are in a regime where the decays are capture limited,¹⁵ which explains why all components in the spectrum appear to decay with the same rate. Hence, while the low-temperature time-resolved spectra do not show long lifetimes for the BE_F luminescence, the data are not inconsistent with the model proposed above.

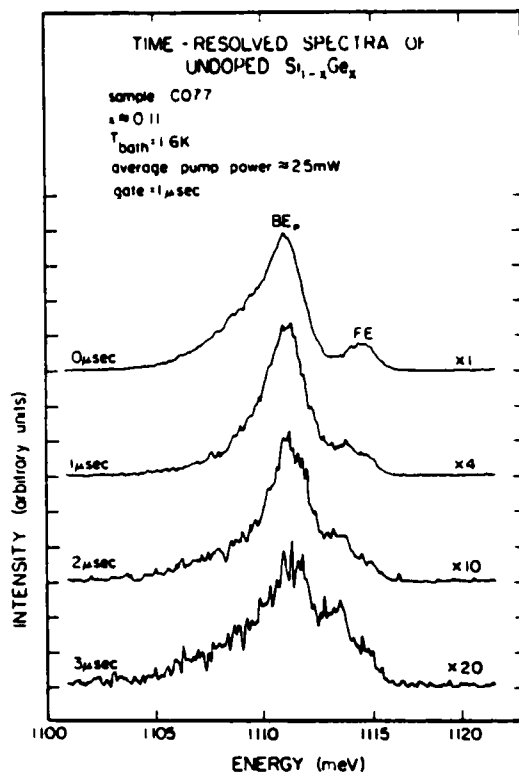


FIG. 15. Time-resolved spectra of undoped $\text{Si}_{1-x}\text{Ge}_x$ sample C077 at 1.6 K. The scale factors (e.g., $\times 4$) give the relative intensity magnification. Note that FE luminescence does not dominate the long-time spectrum.

VI. SUMMARY AND CONCLUSION

In this paper, we have presented the results of a study of the photoluminescence spectra of Si-rich $\text{Si}_{1-x}\text{Ge}_x$ alloy materials. Undoped and In-doped samples were considered in the range $0.067 \leq x$

≤ 0.11 . The luminescence features observed in the spectra were identified as free-exciton and bound-exciton luminescence. The free-exciton luminescence is described very accurately by the Si no-phonon free-exciton line shape, Eq. (1). As a result, a no-phonon free-exciton threshold energy was obtained for each sample.

In addition to this identification of the luminescence features, mechanisms for the observed bound-exciton luminescence broadening were discussed. On the basis of this discussion, the Si-Ge luminescence energies were compared with those from Si, and values for the alloy band-gap shift and change in free-exciton binding energy were obtained. Finally, evidence was presented which may indicate that luminescence from excitons bound to local composition fluctuations is observed in the low-temperature luminescence spectra.

ACKNOWLEDGMENTS

The authors would like to thank R. Baron, J. Baukus, O. J. Marsh, and H. Kimura of Hughes Research Laboratories for growing and characterizing the Si-Ge alloy samples. Also, we have appreciated valuable discussions with Y. C. Chang, A. T. Hunter, and R. M. Feenstra. Finally, we acknowledge the financial support of the Office of Naval Research under Contract No. N00014-81-C-0285, and the National Sciences and Engineering Research Council of Canada.

¹A. Onton, *J. Lumin.* **7**, 95 (1973), and references therein.

²D. J. Wolford, R. E. Anderson, and B. G. Streetman, *J. Appl. Phys.* **48**, 2442 (1977), and references therein.

³Zh. I. Alferov, V. I. Amosov, D. Z. Garbuzov, Yu. V. Zhilyaev, S. G. Konnikov, P. S. Kop'ev, and V. G. Trofim, *Fiz. Tekh. Poluprovodn.* **6**, 1879 (1972) [*Sov. Phys.—Semicond.* **6**, 1620 (1973)], and references therein.

⁴A. T. Hunter, D. L. Smith, and T. C. McGill, *Appl. Phys. Lett.* **37**, 200 (1980), and references therein.

⁵See, for example, E. F. Gross, N. S. Sokolov, and A. N. Titkov, *Fiz. Tverd. Tela (Leningrad)* **14**, 2004 (1972) [*Sov. Phys.—Solid State* **14**, 1732 (1973)].

⁶R. Rentzsch and I. S. Shlimak, *Fiz. Tekh. Poluprovodn.*

12, 713 (1978) [*Sov. Phys.—Semicond.* **12**, 416 (1978)].

⁷C. Benoit à la Guillaume and M. Voos, *Phys. Rev. B* **10**, 4995 (1974).

⁸S. A. Lyon, D. L. Smith, and T. C. McGill, *Phys. Rev. Lett.* **41**, 56 (1978).

⁹R. B. Hammond, D. L. Smith, and T. C. McGill, *Phys. Rev. Lett.* **35**, 1535 (1975).

¹⁰W. Schmid, *Phys. Status Solidi B* **84**, 529 (1977).

¹¹S. A. Lyon, D. L. Smith, and T. C. McGill, *Phys. Rev. B* **17**, 2620 (1978).

¹²Zh. I. Alferov, E. L. Portnoi, and A. A. Rogazhev, *Fiz. Tekh. Poluprovodn.* **2**, 1194 (1968) [*Sov. Phys.—Semicond.* **2**, 1001 (1969)].

¹³J. P. Dismukes, L. Ekstrom, and R. J. Paff, *J. Phys.*

- Chem. **68**, 3021 (1964).
- ¹⁴R. Braunstein, A. R. Moore, and F. Herman, Phys. Rev. **109**, 695 (1958).
- ¹⁵G. S. Mitchard, Ph. D. thesis, California Institute of Technology, 1981 (unpublished).
- ¹⁶S. D. Baranovskii and A. L. Éfros, Fiz. Tekh. Poluprovdn. **12**, 2233 (1978) [Sov. Phys.—Semicond. **12**, 1328 (1978)].
- ¹⁷S. Lai and M. V. Klein, Phys. Rev. Lett. **44**, 1087 (1980).
- ¹⁸G. C. Osbourn, S. A. Lyon, K. R. Elliott, D. L. Smith, and T. C. McGill, Solid State Electron. **21**, 1339 (1978).

Vibrational modes of oxygen in GaP including nearest-neighbor interactions

R. M. Feenstra,* R. J. Hauenstein, and T. C. McGill

California Institute of Technology, Pasadena, California 91125

(Received 10 March 1983; revised manuscript received 16 August 1983)

A theoretical treatment of the vibrational modes of substitutional defects in zinc-blende crystals is presented. The dynamics of the perfect lattice are described with the use of a two-parameter model including nearest-neighbor interactions only. The defect consists of an impurity atom with variable strength nearest-neighbor force constants. For the case of oxygen in GaP, the theoretical defect vibrational modes are compared with experiment. Agreement between theory and experiment is obtained for values of the defect force constants which are 15% of the bulk values for the O^0 and O^+ defects, indicating that the oxygen impurity is quite weakly bonded in the lattice.

I. INTRODUCTION

An oxygen atom on a P site in GaP is a defect with many interesting and controversial properties. The vibrational states of the defect are observed in phonon-assisted transitions appearing in a variety of optical spectra.¹⁻⁴ From the relatively low energy of those phonon modes which involve oxygen motion,² it seems that the oxygen impurity is quite weakly bonded in the lattice,⁵ and recent theoretical studies⁶ support this conclusion. In this paper, we theoretically examine the vibrational modes of an oxygen defect with T_d symmetry. We use a phenomenological model for the lattice dynamics with the force constants between the defect and neighboring atoms being treated as parameters in the theory. We compare our results with experiment for the O^0 and O^+ defects (with and without the first donor electron present, respectively). We find reasonable agreement between theory and experiment for defect force constants which are about 15% of the bulk values, thus supporting the current view that the O^0 and O^+ defects are weakly bonded in a T_d symmetric site.

In this paper the dynamics of the perfect lattice are described using a two-parameter model which includes nearest-neighbor interactions only. By symmetry, only two parameters are required for the most general description of the bulk phonons in this model,⁷ and these parameters are chosen to fit known phonon dispersion curves. A substitutional defect consists of an impurity atom of given mass with variable-strength nearest-neighbor force constants. The properties of a defect are thus determined by only two parameters. Therefore, we are able to obtain quite general results for defects within our very simplified model for the bulk crystal. More complicated models are available for the bulk phonons, and, in particular, the 15-parameter deformable-dipole model of Kunc⁸ seems to give a good description of many III-V compounds. However, within this model a substitutional defect is also described by 15 (or more) parameters, and the results for the defect vibrational modes may be somewhat dependent on the choice of parameter values. Thus, the complicated models yield specific results for a defect within a realistic model for the bulk. Because of this phenomenological nature of our calculations we feel that it is necessary to ex-

amine the results from both the simple and complicated dynamical models. In this paper we present results from the simple two-parameter model and results from the deformable-dipole model are planned to be the topic of a forthcoming publication.⁹

Previous workers^{5,6,10} have considered the vibrational states of the GaP:O defect using molecular-type models of the defect and its immediate neighbors. Here, we use the Green's-function technique,¹¹ which allows us to compute the vibrational states of the defect including the response of the entire lattice. The advantage of this technique is that it allows us to couple the vibrations of the defect into the bulk crystal and see which types of vibrational modes remain localized around the defect. The term "localized" will be used here to refer to both strictly localized vibrational modes and resonant vibrational modes in which the vibrational amplitude is relatively peaked near the defect. The quantity we will use to describe the vibrational modes of a defect is the local density of states (LDOS). Strictly localized modes show up as δ functions in the LDOS and resonant modes appear as peaks with some nonzero width.

In Sec. II we present the details of our computational technique. Our method is quite similar to other vibrational Green's-function computations.^{7,12} The results of our calculations are presented in Sec. III. We show the computed dispersion curves and density of states (DOS) for the bulk phonons in GaP. A model is used for the substitutional O defect in which the nearest-neighbor O-Ga force constants are all varied by the same amount. For various values of the defect force constant the LDOS for A_1 and T_2 defect vibrational modes are presented. We find basically one A_1 and one T_2 vibrational mode of the defect. In Sec. IV we compare our theoretical results with experiment. For defect force constants which are 15% of the bulk values, we identify our computed T_2 mode with the 24.7-meV resonance observed for the O^0 defect.² Our computed A_1 mode is identified with the 19-meV mode observed,^{1,3} for the O^0 and O^+ defects. We argue that these phonons are the most localized models of the defect. Other modes observed in the optical spectra are either bulklike phonons or relatively delocalized defect modes. The conclusions which can be drawn from this work are presented in Sec. V.

II. COMPUTATIONAL METHOD

A. Bulk phonons

The lattice dynamics of the perfect crystal are described using a two-parameter model consisting of nearest-neighbor interactions only. As shown by Grimm *et al.*,⁷ in the harmonic approximation, invariance of potential energy with respect to rigid-body translations, rotations, and symmetry operations of the crystal lattice result in only two parameters required to describe the bulk phonons. In this model the matrix of second derivatives of the potential energy with respect to atomic positions has diagonal Cartesian blocks of the form

$$\Phi(\text{Ga}; \text{Ga}) = \Phi(\text{P}; \text{P}) = \begin{bmatrix} 4A & 0 & 0 \\ 0 & 4A & 0 \\ 0 & 0 & 4A \end{bmatrix} \quad (1a)$$

and off-diagonal blocks typically of the form

$$\Phi(\text{Ga}; \text{P}) = \Phi(\text{P}; \text{Ga}) = - \begin{bmatrix} A & B & B \\ B & A & B \\ B & B & A \end{bmatrix}. \quad (1b)$$

where l and m label the N unit cells, a and b label atomic types, and α and β label Cartesian coordinates. $\omega_{n, \vec{k}}^2$ are the eigenvalues and $\xi_a^\alpha(n, \vec{k})$ are the eigenvectors of the (n, \vec{k}) th normal mode. The equilibrium position of an atom is denoted by \vec{R}_{la} , and m_a is the mass of the a th atom.

To evaluate the LDOS of a crystal containing a defect it is necessary to compute that portion of the Green's function which is in the space of the defect. The defects we consider here consist of a substitutional impurity atom in a zinc-blende crystal with bonds of variable strength connecting the impurity atom to its neighboring atoms. This defect consists of a five-atom cluster with T_d symmetry. The positions of the five atoms are specified by 15 Cartesian coordinates, which form a 15-dimensional representation of the T_d group. This reducible representation Γ can be decomposed into the irreducible representation of the T_d group according to

$$\Gamma = A_1 + E + T_1 + 3T_2. \quad (4)$$

This equation classifies the collective coordinates of the five-atom cluster. The A_1 coordinate consists of a "breathing" type of motion in which the central atom is stationary and the outer atoms move radially. The motion of the central impurity atom forms a basis for a T_2 representation of the T_d group. The other two sets of T_2 coordinates involve motion of the outer atoms. Similarly, the

For convenience we decompose the parameters A and B into bond-stretching and bond-bending components.¹³ The contribution to the potential energy of the system from a bond (spring) connecting atoms i and j is written as

$$V = \frac{1}{2} f_1 |(\vec{u}_i - \vec{u}_j) \cdot \hat{e}_{ij}|^2 + \frac{1}{2} f_2 |(\vec{u}_i - \vec{u}_j) \times \hat{e}_{ij}|^2, \quad (2a)$$

with

$$\hat{e}_{ij} = \frac{\vec{R}_i - \vec{R}_j}{|\vec{R}_i - \vec{R}_j|} \quad (2b)$$

where \vec{u}_i is the displacement of the i th atom from its equilibrium position \vec{R}_i . The parameters f_1 and f_2 are defined as bond-stretching and bond-bending force constants, respectively, and are related to A and B by $A = (f_1 + 2f_2)/3$ and $B = (f_1 - f_2)/3$.

B. Green's functions

From the eigenvalues and eigenvectors of the dynamical matrix we compute the perfect crystal Green's function G^0 . Maradudin¹¹ has shown that the matrix elements of G^0 can be expressed as

$$G_{lmab}^{0\alpha\beta}(\omega^2) = \frac{1}{N\sqrt{m_a m_b}} \lim_{\epsilon \rightarrow 0^+} \sum_{n, \vec{k}} \frac{\xi_a^\alpha(n, \vec{k}) \xi_b^\beta(n, \vec{k}) \exp[i\vec{k} \cdot (\vec{R}_{la} - \vec{R}_{mb})]}{\omega^2 + i\epsilon - \omega_{n, \vec{k}}^2}, \quad (3)$$

E and T_1 coordinates involve motion of the outer atoms with the inner atom stationary. The definition of all the collective coordinates is given in Appendix A.

To produce a Green's function suitable for computation we apply two coordinate transformations. The first transformation is quite trivial and its effect is to drop the masses m_a and m_b from Eq. (3) and to absorb them into the defect perturbation matrix δL . This corresponds to expressing G^0 with respect to the reduced coordinates $q_i = \sqrt{m_i} u_i$ where u_i are Cartesian coordinates. Secondly, we transform to the collective coordinates Q_i defined in Appendix A. In this coordinate system (s) and (r) label the irreducible representation, σ and ρ label the occurrence of the representation, and μ and ν label the row or column of the representation. The Green's function in the space of the defect can now be expressed as

$$G_{(s)(r)\sigma\rho}^{0\mu\nu}(\omega^2) = \frac{1}{N} \lim_{\epsilon \rightarrow 0^+} \sum_{n, \vec{k}} \frac{Q_{(s)\sigma}^\mu(n, \vec{k}) Q_{(r)\rho}^\nu(n, \vec{k})}{\omega^2 + i\epsilon - \omega_{n, \vec{k}}^2}. \quad (5)$$

The summation on \vec{k} extends over the entire first Brillouin zone. This can be divided into a sum over the irreducible wedge W of the zone and a sum over the group elements R which define the star of \vec{k} . Since the Q coordinates form bases for irreducible representations of the T_d group, they are orthogonal when summed over R , and we find that

$$G_{(s)(r)\sigma\rho}^{0\mu\nu}(\omega^2) = \frac{1}{N} \lim_{\epsilon \rightarrow 0^+} \sum_{n, \vec{k} \in W} \delta_{\mu\nu} \delta_{(s)(r)} \frac{h_{\vec{k}}}{d_s} \frac{\text{Re} \left[\sum_{\kappa} Q_{(s)\sigma}^{\kappa}(n, \vec{k}) Q_{(r)\rho}^{\kappa*}(n, \vec{k}) \right]}{\omega^2 + i\epsilon - \omega_{n, \vec{k}}^2}, \quad (6)$$

where $h_{\vec{k}}$ is the number of points in the star of \vec{k} and d_s is the dimension of the representation (s) [compare with Eq. (41) of Ref. 14]. We see that the Green's function is zero unless $(s)=(r)$ and $\mu=\nu$, in which case it is independent of μ . Thus the Green's function has been block-diagonalized by the transformation to the collective coordinates. The transformed matrix consists of 1×1 , 2×2 , 3×3 , and 9×9 blocks for the A_1 , E , T_1 , and $3T_2$ representations, respectively. Furthermore, these matrix elements do not depend on the row or column of the representation, so that these blocks can be further reduced to 1×1 , 1×1 , 1×1 , and 3×3 symmetric blocks, respectively, for a total of nine independent matrix elements. Keeping the zero elements in mind we can simplify the notation by dropping the subscripts μ , ν , and (r) . Furthermore, the Green's function can be explicitly divided into its real and imaginary parts by defining the partial DOS ("spectral density"),

$$D_{(s)\sigma\rho}(\omega^2) = \frac{1}{N} \sum_{n, \vec{k} \in W} \frac{h_{\vec{k}}}{d_s} \text{Re} \left[\sum_{\kappa} Q_{(s)\sigma}^{\kappa}(n, \vec{k}) Q_{(r)\rho}^{\kappa*}(n, \vec{k}) \right] \times \delta(\omega^2 - \omega_{n, \vec{k}}^2), \quad (7)$$

from which Eq. (6) can be expressed as^{14,15}

$$G_{(s)\sigma\rho}^0(\omega^2) = P \int_0^\infty \frac{D_{(s)\sigma\rho}(\bar{\omega}^2)}{\bar{\omega}^2 - \omega^2} d\bar{\omega}^2 - i\pi D_{(s)\sigma\rho}(\omega^2), \quad (8)$$

where P signifies a principle-value integral. Equations (7) and (8) are in a form suitable for computation. The sum over \vec{k} (in the first Brillouin zone) was reduced to a sum over the irreducible wedge ($\frac{1}{48}$ th of the Brillouin zone for the zinc-blende structure) and was performed using the Gilat-Raubenheimer method.^{16,17} The principal-value integral was then computed following Bernholc and Pantelides.¹⁵ The results presented here were computed using 5950 points in the irreducible wedge corresponding to 256 000 points in the entire zone. The computations were all performed as a function of ω^2 , using an interval size of 4.12 meV^2 . This corresponds to an accuracy of about 0.05 meV in the optical branches and 0.5 meV near the bottom of the acoustic branch. The number of points used in the \vec{k} -space summation was consistent with this ω^2 interval size. For plotting purposes the Green's functions were converted to a linear energy scale by

$$\tilde{G}(\omega)d\omega = G(\omega^2)d\omega^2, \quad (9)$$

where \tilde{G} are the functions which will be shown here.

The Green's function for the imperfect crystal in the space of the defect is computed from¹¹

$$G = (1 - G^0 \delta L)^{-1} G^0, \quad (10)$$

where G^0 and δL are, respectively, the Green's-function and defect-perturbation matrices in the 15×15 space of the defect. The diagonal elements of $-\text{Im}G/\pi$ give the LDOS of the imperfect crystal. For representations which have multiple occurrences in the space of the defect, the LDOS for each occurrence provides a measure of the fraction of total kinetic energy in that particular type of motion, and this quantity is used in the following sections to describe the composition of the T_2 defect modes.

C. Defect-perturbation matrix

The defect-perturbation matrix δL is defined by¹¹

$$\delta L = -\omega^2 \Delta M + \Delta \Phi, \quad (11)$$

where ΔM and $\Delta \Phi$ are, respectively, the mass-defect and force-constant-defect matrices. As discussed by Maradudin,¹¹ $\Delta \Phi$ must be invariant under rigid-body translations, rotations, and the symmetry operations of the imperfect crystal. In the present model, assuming the same value of the force constants change ΔA and ΔB for each of the four bonds surrounding the mass defect, the defect-perturbation matrix has the form given by Talwar, Vandevyver, and Zigone (Table 2 of Ref. 12). The $\Delta \Phi$ component of this matrix explicitly satisfies invariance with respect to translations and crystal symmetry operations. To further satisfy rotational invariance it is necessary to assign $\Delta A = \Delta B$ ($A_t = B_t$ in the notation of Ref. 12), or equivalently the change in bond bending must be zero, $\Delta f_2 = 0$. The physical origin of such a constraint is as follows: Bond bending clearly violates rotational invariance for an isolated XY_4 molecule in space since a rotation of the molecule produces a nonzero energy change, and the invariance constraints for such an isolated molecule are identical with those for the "defect molecule" considered here. However, in considering very weakly bonded defects one would like to uniformly reduce both the bond-stretching and bond-bending force constants to zero to produce a defect which experiences zero restoring force (i.e., $\Delta f_1/f_1 = \Delta f_2/f_2 \rightarrow -1$ or equivalently $\Delta A/A = \Delta B/B \rightarrow -1$). In order to arbitrarily vary the bond-bending force constant it is necessary to introduce an additional defect force constant which has the form of a second-nearest-neighbor bond-bending interaction [as defined in Eq. (2a)] among the four atoms surrounding the mass defect. Denoting this force constant by μ , rotational invariance is satisfied by the condition $\mu = -\Delta f_2/4$. The final form of the defect perturbation matrix is given in Appendix B. We note that the constraint of rotational invariance affects our results only through bond-bending interactions which are relatively small for the GaP lattice. In a preliminary report¹⁸ of our results we neglected rotational invariance, and a comparison between those results

and the results to be presented here reveals that the effects of rotational invariance condition are indeed negligible. Nevertheless, rotational invariance is a fundamental property of the system, and in this paper we completely include its effects.

III. RESULTS

A. Bulk phonons

Shown in Fig. 1 are phonon dispersion curves and DOS computed from the two-parameter model described in Sec. II A. The values of the model parameters f_1 and f_2 have been chosen to produce a reasonable fit to the actual phonon energies of GaP, by matching the TA_X and TO_Γ energies. From the dynamical matrix given by Grimm *et al.*⁷ these energies are found to be

$$\omega^2(TO_\Gamma) = \frac{4A}{M} \quad (12a)$$

and

$$\omega^2(TA_X) = \frac{4A}{M} \left\{ \frac{1}{2} - \frac{1}{2} \left[1 - \frac{4M}{m_a + m_b} \left(1 - \frac{B^2}{A^2} \right) \right]^{1/2} \right\}, \quad (12b)$$

where A and B are specified in Eq. (1) and $M = m_a m_b / (m_a + m_b)$ with a denoting Ga and b denoting P. For GaP the actual energies are known to be¹⁹ $E(TA_X) = 13.1$ meV and $E(TO_\Gamma) = 45.4$ meV, from which the values for the force constants are determined to be $f_1 = 6.87$ eV/Å² and $f_2 = 0.525$ eV/Å². Our dispersion curves can be compared with the shell-model results of Yarnell *et al.*²⁰ and the deformable-dipole model results of Kunc.⁸ The major deficiency of the present computation is that the LO branch (near 40 meV) should actually be higher in energy due to electrostatic interactions which have been neglected in our model. This may affect our results for defect modes in this branch, but it should have little effect on the defect modes at other energies.

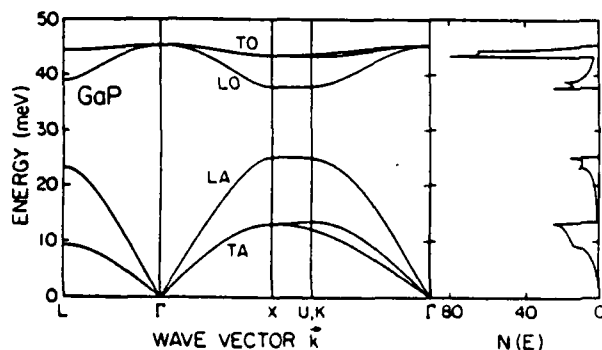


FIG. 1. Phonon dispersion curves and DOS $N(E)$ of GaP computed using the two-parameter valence-force model described in the text. Acoustic (A) and optical (O) branches are labeled according to the polarization of the phonons (T is transverse and L is longitudinal). Some branches may have mixed polarization.

B. Perfect-crystal Green's functions

Shown in Fig. 2 are the elements of the Green's-function matrix for the perfect crystal as computed from Eqs. (6) and (8). These functions are computed using a P site as the origin. We plot $-\text{Im}G^0/\pi$ for the A_1 , E , T_1 , and the diagonal elements of the T_2 representations. Shown on the top of Fig. 2 is the bulk DOS. The Green's-function elements give the partial DOS for each representation. The appearance of the Green's-function elements may be understood by considering the type of atomic motion they represent. For example, the A_1 Green's function is a breathing motion which is made up entirely from longitudinal phonons. With our P-site origin, the A_1 Green's function is very small in the optical branch because the optical modes involve very little motion of the Ga atoms due to the mass difference between Ga and P. The Ga-site Green's function elements can be obtained from the P-site elements by reflecting the $G(\omega^2)$ functions through a mirror plane located at $\omega_{\text{max}}^2/2$, where ω_{max}^2 occurs at the top of the optical branch (e.g., the A_1 Ga-site partial DOS has a small peak in the acoustic branch and a large peak in the optical branch). By summing the partial densities for both a P-site origin and a Ga-site origin we obtain the entire DOS,

$$-\frac{1}{\pi} \text{Im}(\text{Tr}G_P^0) - \frac{1}{\pi} \text{Im}(\text{Tr}G_{Ga}^0) = 5D(\omega^2), \quad (13a)$$

where

$$\text{Tr}G = [G(A_1) + 2G(E) + 3G(T_1) + 3G(T_2^a) + 3G(T_2^b) + 3G(T_2^c)]. \quad (13b)$$

The factor of 5 on the right-hand side of Eq. (13a) arises from the presence of five atoms in the defect cluster. The

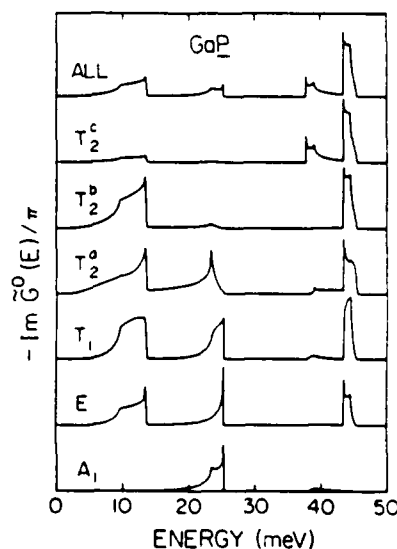


FIG. 2. Imaginary part of the Green's function for the perfect crystal using a P site for the origin in space. At the top is shown the bulk DOS. Elements of the Green's-function matrix shown here are the partial DOS in each of the A_1 , E , T_1 , T_2^a , T_2^b , and T_2^c CC's.

DOS obtained from Eq. (13) can be compared with that directly computed from

$$D(\omega^2) = \frac{1}{N} \sum_{\mathbf{n}, \mathbf{k}} \delta(\omega^2 - \omega_{\mathbf{n}, \mathbf{k}}^2). \quad (14)$$

In our calculations, the $D(\omega^2)$ computed in these two ways agree to an absolute accuracy of 0.004 (for an energy scale corresponding to $\omega_{\max} = 1$), which provides an important check on the computation of the Green's functions.

C. Defect vibrational modes

The vibrational modes of a defect are characterized by a peak in the LDOS. This peak is the center of a band of vibrational modes in which the defect vibrates with significantly greater amplitude than those atoms far removed from it. The defect we are considering consists of an impurity atom substitutional for the P atom. Our results are for oxygen with a mass-defect parameter of

$$\frac{\Delta m}{m} = \frac{m_{\text{O}} - m_{\text{P}}}{m_{\text{P}}} = -0.4834. \quad (15)$$

The springs which connect the impurity to its nearest neighbors are described by bond-stretching f'_1 and bond-bending f'_2 interactions. These interactions are allowed to differ from those of the bulk and they are varied by the same fractional amount. Thus the defect-perturbation matrix depends on only one parameter, $\Delta f/f$, the fractional change in spring constants for the defect relative to the bulk material,

$$\frac{\Delta f}{f} = \frac{f'_1 - f_1}{f_1} = \frac{f'_2 - f_2}{f_2}, \quad (16)$$

where f_1 and f_2 are the bulk spring constants. Negative values of $\Delta f/f$ refer to a weakly bonded defect and positive values refer to a strongly bonded defect. By definition $\Delta f/f \geq -1$. It seems physically unlikely that a substitutional impurity will form bonds which are very much stronger than those of the bulk material. Therefore, we will concentrate our attention on the range $-1 < \Delta f/f < 1$.

For given values of defect spring constants, we compute the LDOS for each type of vibrational mode (A_1 , E , T_1 , and T_2). The LDOS reflects some details of the bulk vibrational modes and also has peaks for each of the defect modes. For defect-perturbation values in the range $-1 < \Delta f/f < 1$ we find defect modes of A_1 and T_2 symmetry only. The A_1 (breathing) mode shown in Fig. 3 is a resonance in the acoustic branch. For $\Delta f/f = 0$ the A_1 LDOS curve at the top of the figure is identical to the A_1 Green's function for the perfect crystal. As $\Delta f/f$ is reduced a resonance mode appears and moves to lower energies. This resonance is rather broad, with a width of about 5 meV. The sum of LDOS for the T_2^x , T_2^y and T_2^z modes is shown in Fig. 4. These modes consist of vibrations of the oxygen atom itself along with some response of the rest of the lattice. For $\Delta f/f = 0$ we obtain a strictly localized mode at 56.3 meV. As $\Delta f/f$ is reduced this T_2 mode falls in energy, entering the optical branch as a

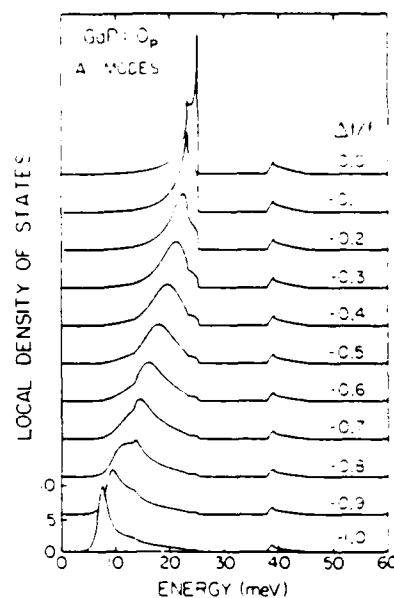


FIG. 3. LDOS of A_1 modes for an O atom on a P site in GaP. Defect force constants $\Delta f/f$ are varied from $\Delta f/f = 0$ (defect springs identical to bulk springs) to $\Delta f/f = -1$ (defect springs to zero strength). Resonance in the acoustic branch appears as a peak in the LDOS. This resonance moves to lower energies as the defect force constant is reduced.

resonance, becoming strictly localized in the acoustic-optical gap, and finally entering the acoustic branch as a rather sharp resonance. As $\Delta f/f \rightarrow -1$, the T_2 mode approaches a δ function at zero energy corresponding to motion of the oxygen atom alone in the absence of any

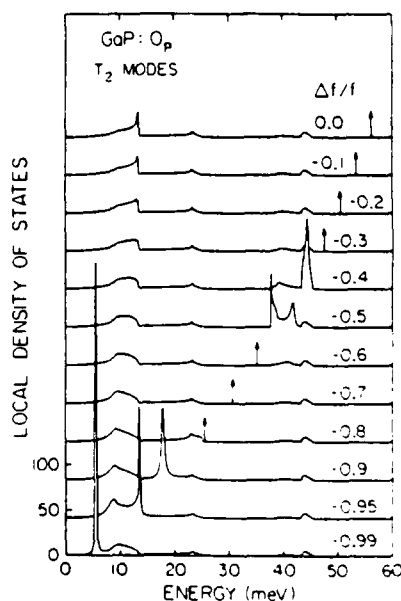


FIG. 4. LDOS of T_2 modes for an O atom on a P site in GaP. For a defect force constant of $\Delta f/f = 0$ a strictly localized mode at 56 meV is shown as a δ function in the LDOS. As $\Delta f/f$ is reduced this mode moves to lower energies, entering the optical branch as a resonance, becoming strictly localized in the acoustic-optical gap, and entering the acoustic branch as a sharp resonance.

restoring force. The T_2 resonances in optical and acoustic branches are relatively sharp with a width of less than 2 meV. The T_2 -defect modes generally consist of at least 80% O (T_2^a) motion. An exception to this is the strictly localized mode in the energy range 25–30 meV which is typically $0.90T_2^a + 0.08T_2^b + 0.02T_2^c$ (presumably this mode is comprised largely of bulk phonons from the very top of the LA branch which include very little P-atom motion).

The results from the LDOS calculations are summarized in Fig. 5. Here we plot the energies of the defect modes versus the defect-spring-constant parameter. On the left-hand side of the figure a bulk DOS is shown for reference. The solid lines in the figure are the Green's-function results. These energies are defined as the location of zeros in the real part of the eigenvalues of the matrix $(1 - G^0 \delta L)$ [Eq. (10)]. For $\Delta f/f < 0$ we see the A_1 and T_2 modes discussed above. For $\Delta f/f > 0$ another T_2 mode consisting of about 70% T_2^b motion appears as a resonance in the acoustic branch. For $-1 < \Delta f/f < 1$, no defect modes of E or T_1 symmetry occur. Physically, this means that E and T_1 vibrations of the defect are strongly coupled to the bulk crystal so that these types of motion are not localized around the defect. The defect perturbation for E modes contains only bond-bending interactions which are relatively weak and produce defect modes only for $\Delta f/f \gg 1$. The defect perturbation for T_1 modes is identically zero as a result of rotational invariance and consequently no T_1 defect modes exist. The defect perturbation for A and T_2 modes contains bond-stretching and mass-defect terms which are relatively large and produce the modes shown here.

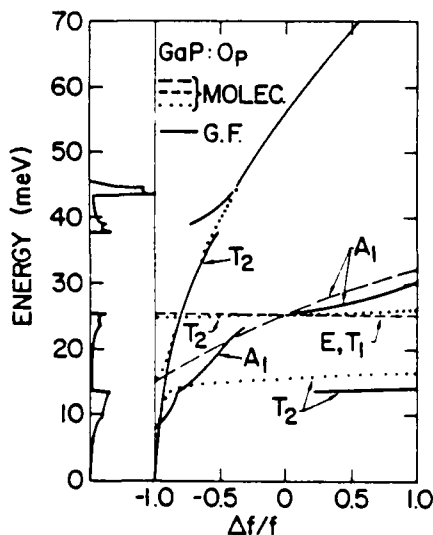


FIG. 5. Defect vibrational modes of oxygen on a P site in GaP. Energy of the modes is plotted vs the defect force constant $\Delta f/f$. Heavy solid lines show the solutions from the Green's-function calculations. Dashed and dotted lines give the vibrational modes of an OGa_4 molecule embedded in an immovable lattice. E and T_1 molecular modes are split by an amount too small to show in the figure. Bulk phonon DOS is shown on the left-hand side of the figure.

The energy of some Green's-function modes are quite close to those calculated from a simple molecular model. In Fig. 5 we show the modes for a OGa_4 molecule imbedded in an immovable lattice according to the formulas given in Appendix C. From the figure it is apparent that the A_1 molecular mode agrees very roughly with the A_1 Green's-function mode. Three T_2 molecular modes exist. Those modes near 25 meV are mainly T_2^a -type (bending motion of the Ga atoms perpendicular to the O—Ga bonds), those modes near 15 meV are mainly T_2^b type (stretching motion of the Ga atoms parallel to the O—Ga bonds), and the modes which vary quadratically with $\Delta f/f$ are mainly T_2^c type (O-atom motion). The modes have mixed nature near the crossing points of the branches. Some of the molecular results agree closely with the Green's-function modes, but other molecular modes appear where there are no Green's-function modes. In the latter case the vibration of the defect is strongly coupled to the bulk modes so that a peak in the LDOS does not appear. This illustrates the major deficiency of the molecular-model results—the number of modes is determined by the size of the cluster. The Green's-function method allows us to couple these modes to the rest of the crystal in order to see if they remain somewhat localized around the defect. The real importance of the molecular-model calculations is that they provide a good check on the Green's function results, since in certain limits the results from both methods agree quite well.

IV. DISCUSSION

The vibrational states of the neutral oxygen defect O^0 are seen in the electron-capture luminescence of Dean and Henry.² In this spectrum the zero-phonon line is forbidden so that the strong one-phonon replicas must involve T_2 phonons.¹⁰ As shown in Fig. 2 of Dean and Henry's work vibrational modes involving oxygen motion are seen at 24.7 and 28.4 meV (resonances in the acoustic branch) and various phonon replicas are also seen in the optical branch. Since oxygen has a smaller mass than phosphorus, it is necessary to considerably reduce the O—Ga force constants relative to the bulk Ga—P force constants to produce such low-energy modes.^{5,6} Comparing the experimental results with the theoretical T_2 modes shown in Fig. 4 we see that it is necessary to reduce the strength of the defect force constants to $\Delta f/f < -0.8$ to produce the resonance in the acoustic branch. In Fig. 6 we show the LDOS for T_2 modes using $\Delta f/f = -0.85$, and mass defects corresponding to ^{16}O and ^{18}O . The theory predicts one T_2 resonant mode centered at 21.9 meV for ^{16}O . Dean and Henry² report a value of -1.6 meV for the $^{16}\text{O} \rightarrow ^{18}\text{O}$ isotope shift of the 24.7 meV peak. As shown in Fig. 6 we calculate a shift of -1.14 meV for this resonance peak, which we consider to be within experimental uncertainty of the observed -1.6 meV considering the limited resolution of the $^{16}\text{O}_{\text{loc}}$ peak in the data.² Thus we identify our computed 21.9-meV resonance with the observed 24.7-meV mode. Our computed isotope shift is 83% of what would be expected for motion of the O atom alone. Alternatively, the LDOS gives the composition of the T_2 resonance mode to be $0.05T_2^a + 0.87T_2^b + 0.87T_2^c$.

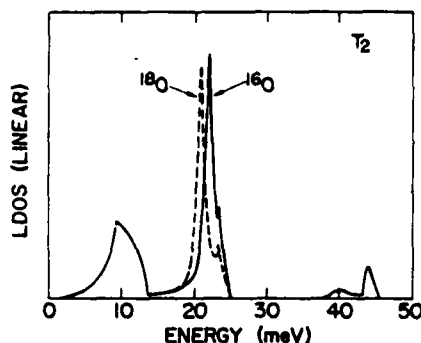


FIG. 6. LDOS for T_2 modes of ^{16}O (solid line) and ^{18}O (dashed line) defects using a defect force constant of $\Delta f/f = -0.85$.

According to our calculations the first-shell Ga atoms always make a significant contribution to the resonance. Motion of the O atom alone is not a normal mode of the system (except for $\Delta f/f = -1$).

The vibrational mode observed² at 28.4 meV is not well described by the present theory. However, we suggest that this feature is partly due to a peak in the bulk T_2 DOS (LA phonons) which adds structure to the LDOS. This feature does not appear in Fig. 6 because of the simplified model used for the bulk phonons, but better models^{8,20} do indeed show a strong peak near 27 meV. In the optical branch the experiments observe a number of vibrational modes. In Fig. 6 we see some small features in the optical branch, but these are associated only with the bulk DOS and are not localized near the defect. However, as discussed above, the LO branch of our theoretical phonon dispersion curves is quite crude and more sophisticated models may produce additional defect modes there.

Phonons of energy 19.5 and 47 meV have been observed for the O^+ defect in the donor-acceptor-pair (DAP) luminescence of Dean, Henry, and Frosch.¹ Morgan¹⁰ argues that these phonons are A_1 -type modes since the zero-phonon transition is allowed. We note that phonons involving colinear motion of the oxygen and acceptor atoms are in fact allowed in the DAP spectra (these modes are T_2 type with respect to the T_d symmetry of the isolated O atom). This fact led us originally to conclude that the 47-meV phonon was a T_2 mode involving resonant O motion.¹⁸ However, calculations show that the intensity of a strictly localized T_2 phonon replica in a DAP spectrum is very weak for distant DAP's. This probably is true for localized resonant modes also. We conclude that the 47-meV mode does not involve localized O motion.

In photoluminescence excitation experiments on the O^0 defect, Monemar and Samuelson³ observed phonons of energy 19 and 48 meV. These energies equal those for the O^+ defect within an experimental uncertainty of about 5%. Alternatively, Henry and Lang²¹ propose a shift of 22% in the phonon energies of the different charge states in order to explain observed nonradiative capture cross sections. These two results are not necessarily inconsistent since the 19- and 48-meV modes may be relatively insensitive to force-constant changes, whereas the

capture-cross-section data include the T_2 modes which are quite dependent on the defect force constants. A good method to determine the difference between O^+ and O^0 force constants would be the observation of the O^+ T_2 mode, predicted by Baraff *et al.*⁶ to lie at 32.4 meV. In any case, considering the accuracy of the computations present here, the difference between O^+ and O^0 force constants is relatively small and we will henceforth use the same force constants ($\Delta f/f = -0.85$ as determined above) for both charge states.

Turning now to the calculation, for $\Delta f/f = -0.85$ we find an A_1 resonance at 12.2 meV, which we identify with the observed 19-meV phonon. In the present model the computed energy of this mode is somewhat low, but results from more complicated models⁹ yield an A_1 phonon energy much closer to that observed. The computed resonance has a width of about 5 meV, which is comparable to the 3-meV lifetime broadening estimated by Monemar and Samuelson.³ The breadth of this resonance indicates that it is not too strongly localized around the defect, so that the mode involves breathing motion of the first Ga shell along with significant contributions from further shells. In the optical branch we find no A_1 resonances for $\Delta f/f \approx -0.85$. There are no A_1 modes here because optical phonons involve mainly P-atom motion (see Sec. III B), and in the present calculation it is very difficult to localize this type of motion since the P atoms are in the second shell around the O atom but the defect force constants extend only to the first shell. Possibly an A_1 mode in the optical branch could be produced by adjusting second-nearest-neighbor O-P bonds or Ga-P back bonds. However, from the present model we conclude that the 47-meV mode does not involve localized breathing motion of the first Ga shell.

In summary, for a defect force constant of $\Delta f/f = -0.85$ our theory finds an A_1 resonance at 12.2 meV and a T_2 resonance at 21.9 meV, which we identify with the observed 19.5- (Ref. 1) and 24.7-meV (Ref. 2) modes, respectively. No other defect modes are predicted by the theory and we conclude that other observed modes are not localized at the O impurity or in the first Ga shell. As discussed above, the identification by Morgan¹⁰ of the observed 47-meV (Refs. 1 and 3) phonon as an A_1 mode localized on P atoms is consistent with our results. Also we argue that the observed 28.4-meV peak (Ref. 2) may be partly due to a peak in the LA-phonon bulk DOS. Similarly, the phonons labeled A-C in the capture luminescence (Ref. 2) may also be due to peaks in the bulk DOS or they may be some type of delocalized vibrational modes of the defect.

V. CONCLUSIONS

In this paper we theoretically analyze the vibrational modes of substitutional oxygen in GaP using nearest-neighbor interactions only. Our theory predicts the presence of basically one mode of A_1 symmetry and one mode of T_2 symmetry which are localized (strictly localized or resonant) around the O impurity. We identify these localized modes with phonons observed in the optical spectra of the O^0 and O^+ defects, and we argue that other pho-

nons observed in these spectra are relatively delocalized. By the term delocalized, we mean a bulk phonon or a defect mode which is not significantly localized at the O impurity or in the first shell of Ga atoms. We should emphasize that the number of localized modes predicted by the present theory is largely determined by the model used for the defect perturbation, i.e., relaxation of nearest-neighbor O—Ga force constants only. More sophisticated defect models do produce additional localized modes, and these modes will be discussed in a forthcoming publication.⁹ However, since the defect perturbation is basically unknown, we feel that even the simple results presented

here provide new insight concerning the nature of the vibrational modes of oxygen in GaP.

ACKNOWLEDGMENTS

The authors thank T. N. Morgan for useful discussions. Valuable computation assistance was provided by C. A. Swarts. One of us (R.M.F.) was supported by a scholarship from the Natural Sciences and Engineering Research Council of Canada. This work was supported in part by the Office of Naval Research under Contract No. N00014-81-K-0305.

APPENDIX A: COLLECTIVE COORDINATES FOR A FIVE-ATOM TETRAHEDRAL CLUSTER

The collective coordinates Q are expressed in terms of the Cartesian coordinates (x, y, z) of each atom. The atoms are numbered 0–4 located along lattice directions (0,0,0), (1,1,1), (−1,−1,1), (−1,1−1), and (1,−1,−1), respectively. The collective coordinates form bases for the irreducible representation of the T_d group as indicated. NF denotes the normalization factor.

	A_1 Q_1	E Q_2 Q_3	T_1 Q_4 Q_5 Q_6	T_2^1 Q_7 Q_8 Q_9	T_2^2 Q_{10} Q_{11} Q_{12}	T_2^3 Q_{13} Q_{14} Q_{15}
x_0	0	0 0	0 0 0	0 0 0	0 0 0	1 0 0
y_0	0	0 0	0 0 0	0 0 0	0 0 0	0 1 0
z_0	0	0 0	0 0 0	0 0 0	0 0 0	0 0 1
x_1	1	−1 1	0 1 −1	2 −1 −1	1 1 1	0 0 0
y_1	1	−1 −1	−1 0 1	−1 2 −1	1 1 1	0 0 0
z_1	1	2 0	1 −1 0	−1 −1 2	1 1 1	0 0 0
x_2	−1	1 −1	0 1 1	2 −1 1	1 1 −1	0 0 0
y_2	−1	1 1	−1 0 −1	−1 2 1	1 1 −1	0 0 0
z_2	1	2 0	−1 1 0	1 1 2	−1 −1 1	0 0 0
x_3	−1	1 −1	0 −1 −1	2 1 −1	1 −1 1	0 0 0
y_3	1	−1 −1	1 0 −1	1 2 1	−1 1 −1	0 0 0
z_3	−1	−2 0	1 1 0	−1 1 2	1 −1 1	0 0 0
x_4	1	−1 1	0 −1 1	2 1 1	1 −1 −1	0 0 0
y_4	−1	1 1	1 0 1	1 2 −1	−1 1 1	0 0 0
z_4	−1	−2 0	−1 −1 0	1 −1 2	−1 1 1	0 0 0
NF	$\sqrt{12}$	$\sqrt{24}$ $\sqrt{8}$	$\sqrt{8}$ $\sqrt{8}$ $\sqrt{8}$	$\sqrt{24}$ $\sqrt{24}$ $\sqrt{24}$	$\sqrt{12}$ $\sqrt{12}$ $\sqrt{12}$	1 1 1

APPENDIX B: ELEMENTS OF THE DEFECT-PERTURBATION MATRIX δL USED FOR THE GREEN'S-FUNCTION COMPUTATIONS

The defect consists of a central O atom surrounded by four identical Ga atoms. The difference between the O—Ga force constants and those of the bulk is denoted Δf_1 for bond-stretching and Δf_2 for bond-bending interactions. The mass difference is denoted by $\Delta m = m_O - m_P$. Bond-bending interaction of strength μ are introduced between the Ga atoms and $\mu = -\Delta f_2/4$ by rotational invariance. The subscripts $a - c$ in the T_2 matrix refer to the collective coordinates listed in Appendix A. We write

$$\begin{aligned} \delta L(A_1) &= \frac{1}{m_{Ga}} \Delta f_1, \quad \delta L(E) = \frac{1}{m_{Ga}} (\Delta f_2 + 3\mu), \quad \delta L(T_1) = \frac{1}{m_{Ga}} (\Delta f_2 + 4\mu), \quad \delta L_{aa}(T_2) = \frac{1}{m_{Ga}} (\Delta f_2 + \frac{2}{3}\mu), \\ \delta L_{bb}(T_2) &= \frac{1}{m_{Ga}} (\Delta f_1 + \frac{4}{3}\mu), \quad \delta L_{cc}(T_2) = \frac{1}{m_P} (\frac{4}{3}\Delta f_1 + \frac{8}{3}\Delta f_2 - \omega^2 \Delta m), \quad \delta L_{ab}(T_2) = \delta L_{ab}(T_2) = -\frac{\sqrt{8}}{3m_{Ga}} \mu, \\ \delta L_{bc}(T_2) &= \delta L_{cb}(T_2) = \left[\frac{4}{3m_{Ga}m_P} \right]^{1/2} \Delta f_1, \quad \delta L_{ac}(T_2) = \delta L_{ca}(T_2) = \left[\frac{8}{3m_{Ga}m_P} \right]^{1/2} \Delta f_2. \end{aligned}$$

APPENDIX C: VIBRATION FREQUENCIES ω OF AN OGa_4 CLUSTER EMBEDDED IN AN IMMOVABLE LATTICE

Nearest-neighbor bond-stretching and bond-bending force constants f'_1 and f'_2 , respectively, refer to O—Ga bonds and f_1 and f_2 refer to those bonds connecting the Ga atoms to the immovable lattice. Second-nearest-neighbor bond-bending interactions of strength μ are introduced between the Ga atoms and $\mu = -(f'_2 - f_2)/4$ by rotational invariance. The subscripts $a - c$ in matrix \underline{C} refer to the collective coordinates listed in Appendix A. We have

$$\begin{aligned}\omega^2(A_1) &= \frac{1}{m_{\text{Ga}}} (f'_1 + \frac{1}{3}f_1 + \frac{8}{3}f_2), \quad \omega^2(E) = \frac{1}{m_{\text{Ga}}} (f'_2 + 3\mu + \frac{4}{3}f_1 + \frac{5}{3}f_2), \quad \omega^2(T_1) = \frac{1}{m_{\text{Ga}}} (f'_2 + 4\mu + \frac{4}{3}f_1 + \frac{5}{3}f_2), \\ \omega^2(T_2) &= \text{eigenvalues of matrix } \underline{C}, \quad C_{11} = \frac{1}{m_{\text{Ga}}} (f'_2 + \frac{2}{3}\mu + \frac{4}{3}f_1 + \frac{5}{3}f_2), \quad C_{22} = \frac{1}{m_{\text{Ga}}} (f'_1 + \frac{4}{3}\mu + \frac{1}{3}f_1 + \frac{8}{3}f_2), \\ C_{33} &= \frac{1}{m_{\text{O}}} (\frac{4}{3}f'_1 + \frac{8}{3}f'_2), \quad C_{12} = C_{21} = -\frac{\sqrt{8}}{3m_{\text{Ga}}} \mu, \quad C_{23} = C_{32} = \left[\frac{4}{3m_{\text{Ga}}m_{\text{O}}} \right]^{1/2} f'_1, \quad C_{13} = C_{31} = \left[\frac{8}{3m_{\text{Ga}}m_{\text{O}}} \right]^{1/2} f'_2.\end{aligned}$$

*Permanent address: IBM Thomas J. Watson Research Center, Yorktown Heights, NY 10598.

¹P. J. Dean, C. H. Henry, and C. J. Frosch, Phys. Rev. **168**, 812 (1968).

²P. J. Dean and C. H. Henry, Phys. Rev. **176**, 928 (1968).

³B. Monemar and L. Samuelson, J. Lumin. **12/13**, 507 (1976); Phys. Rev. B **18**, 809 (1978).

⁴P. J. Dean, Physica **117&118B**, 140 (1983).

⁵R. M. Feenstra and T. C. McGill, Phys. Rev. Lett. **47**, 925 (1981).

⁶G. A. Baraff, E. O. Kane, and M. Schlüter, Phys. Rev. Lett. **47**, 601 (1981); Phys. Rev. B **25**, 548 (1982).

⁷A. Grimm, A. A. Maradudin, I. P. Ipatova, and A. V. Subashiev, J. Phys. Chem. Solids **33**, 775 (1972).

⁸K. Kunc, Phys. Status Solidi B **72**, 229 (1975); Ann. Phys. (Paris) **8**, 319 (1973).

⁹R. J. Hauenstein, T. C. McGill, and R. M. Feenstra (unpublished).

¹⁰T. N. Morgan, Phys. Rev. Lett. **40**, 190 (1968).

¹¹A. A. Maradudin, Rep. Prog. Phys. **28**, 331 (1965); in *Solid State Physics*, edited by F. Seitz and D. Turnbull (Academic,

New York, 1966), Vol. 18, p. 273.

¹²D. N. Talwar, M. Vandevyver, and M. Zigone, J. Phys. C **13**, 3775 (1980).

¹³J. deLaunay, in *Solid State Physics*, edited by F. Seitz and D. Turnbull (Academic, New York, 1956), Vol. 2, p. 210.

¹⁴J. Bernholc, N. O. Lipari, and S. T. Pantelides, Phys. Rev. B **21**, 3545 (1980).

¹⁵J. Bernholc and S. T. Pantelides, Phys. Rev. B **18**, 1780 (1978).

¹⁶G. Gilat and L. J. Raubenheimer, Phys. Rev. **144**, 390 (1966).

¹⁷J. F. Janak, in *Computational Methods in Band Theory*, edited by P. M. Marcus, J. F. Janak, and A. R. Williams (Plenum, New York, 1971), p. 323.

¹⁸R. M. Feenstra and T. C. McGill, Physica **117&118B**, 149 (1983).

¹⁹P. J. Dean, Phys. Rev. **157**, 655 (1967).

²⁰J. L. Yarnell, J. L. Warren, R. G. Wenzel, and P. J. Dean, in *Neutron Inelastic Scattering* (IAEA, Vienna, 1968), Vol. 1, p. 301; see also Fig. 50 of A. S. Barker, Jr. and A. J. Sievers, Rev. Mod. Phys. **47**, Suppl. 2 (1975).

²¹C. H. Henry and D. V. Lang, Phys. Rev. B **15**, 989 (1977).

Vibrational modes of oxygen in GaP including second-nearest-neighbor interactions

R. J. Hauenstein and T. C. McGill

California Institute of Technology, Pasadena, California 91125

R. M. Feenstra

IBM, Thomas J. Watson Research Center, Yorktown Heights, New York 10598

(Received 11 October 1983)

The localized and resonant vibrational modes of a substitutional oxygen defect in GaP have been computed with the use of the Green's-function approach. A 15-parameter version of the deformable-dipole model was used to describe the lattice dynamics of bulk GaP. A defect, consisting of a mass perturbation at the substitutional site and a perturbation among the nearest- and second-nearest-neighbor short-range interactions near the oxygen atom, was considered. The local modes, labeled by symmetry, are presented as a function of the interaction perturbation. Quantitative agreement with experimental results for O^0 and O^+ defects is obtained by weakening the O (-Ga and -P) short-range interactions to 38% of the bulk values while weakening the Ga-P back bonds. With the inclusion of Coulomb effects, this corresponds to an effective O-lattice force constant of 3.5 eV/\AA^2 , which is 25% of the bulk, P-lattice value.

I. INTRODUCTION

The properties of the point defect GaP: O_P in which oxygen substituting for phosphorous in GaP forms a deep donor, have been actively studied, often generating considerable controversy.¹⁻⁶ In particular, numerous optical spectra have been reported. These highly structured spectra contain features due to transitions assisted by local phonons. By calculating the local vibrational modes of the O defect, we can, through comparison with the observed spectra, directly identify mode symmetries and characterize the atomic motion near the defect. We can also determine how the short-range interactions between atoms near the defect site are modified when the defect is introduced. In addition, assumptions of defect-site geometry (T_d symmetry and small local lattice relaxation, in particular) implicit in the local-mode calculation provide consistency checks on the interpretation of experimental results.

In this paper, we use the Green's-function approach to calculate the local phonon modes for oxygen isotopes on a phosphorous site in GaP. This work represents an extension of an earlier Green's-function calculation⁷ in which bulk interactions were limited to nearest-neighbor (NN) interactions. Here, we use the deformable-bond approximation (DBA) of Kunc *et al.*⁸ as the phenomenological description of bulk GaP. This 15-parameter model includes short-range interactions out to second-nearest neighbors (2NN) and long-range Coulomb effects arising from the electrostatic interaction between induced dipoles.⁸ Our defect consists of a mass perturbation at the substitutional site and a perturbation in the short-range interactions among the 17-atom cluster consisting of the O, the four neighboring Ga, and the 12 2NN P atoms. We do not explicitly consider perturbations in the Coulomb interactions since their long range would render the Green's-function approach intractable. As we shall see,

however, the Coulomb portion of the total interaction is relatively small and can be effectively contained in the short-range defect perturbation for sufficiently localized modes.

The DBA and Green's-function theory are briefly described in Sec. II. In that section we also discuss the defect perturbation considered in this work, and we derive an exact expression for the Coulomb contribution to the restoring force resulting from the displacement of a single atom in an infinite lattice. We find the Coulomb portion of the restoring force for a P-site single-atom displacement to be -17.7% of the bulk short-range component. Next, in Sec. III, we present our computed dispersion curves, density of states (DOS), and selected Green's functions for bulk GaP. In Sec. III we also present the results of our local-mode calculations for GaP: O_P . (Here, we shall use "local mode" to refer to both strictly localized and resonant modes, as in Ref. 7.) The interaction perturbation considered consists of varying certain O-Ga, O-P, and Ga-P (back-bond) force constants by the respective fractions, η , η , and 0.12η , of the corresponding bulk short-range values. Energies for local modes of a given symmetry are then presented as a function of the parameter η . The local DOS (LDOS) and "eigenvectors" are presented for selected local modes, and a discussion of the major features and the choice of defect parameters is given.

An extensive comparison to available photoluminescence data is made in Sec. IV. There, we see that the electron-capture luminescence data for the O^0 defect² is well described by our calculations for the value $\eta = -0.62$. In particular, we identify the phonon replicas at 24.7 and 28.4 meV with the peaks in our T_2 LDOS at 25.0 and 28.2 meV, respectively. Both peaks in the LDOS shift under isotopic substitution of ^{18}O for ^{16}O as expected. Our computed A_1 modes at 20.4 and 48.2 meV are observed for the charge states O^+ and O^0 .^{1,3} In all cases we

find substantial improvement in the agreement, both qualitative and quantitative, between calculated and observed values over that predicted by our earlier model.⁷ Finally, the conclusions that can be drawn from this work are summarized in Sec. V.

II. COMPUTATIONAL METHOD

A. Bulk phonons

To describe the lattice dynamics of bulk GaP we have used the DBA. This model is a 15-parameter version of the deformable-dipole model of Kunc *et al.*, and has been shown to provide a good description of several III-V compounds.⁸ The quantities of interest for our calculations are the force-constant matrix Φ and the dynamical matrix D , which is related to Φ by the equation, $D = M^{-1/2} \Phi M^{-1/2}$. In this expression, M is a diagonal matrix whose elements are equal to the masses in the problem. In the DBA, the force-constant matrix has the form

$$\Phi = \Phi^{(SR)} + \Phi^{(el)},$$

$$-\Phi^{(el)} = (Z + N^+)(1 - Bg)^{-1}B(Z + N), \quad (1)$$

where $\Phi^{(SR)}$ and $\Phi^{(el)}$ correspond, respectively, to the short-range and electrostatic terms. The short-range force-constant matrix $\Phi^{(SR)}$ contains the non-Coulombic interactions which in the DBA extend out to 2NN's. As a consequence of the T_d symmetry of GaP, the off-diagonal Cartesian blocks can be shown to have the form⁸

$$\Phi^{(SR)}(\text{Ga}; \text{P}) = \Phi^{(SR)}(\text{P}; \text{Ga}) = \begin{pmatrix} A & B & B \\ B & A & B \\ B & B & A \end{pmatrix}, \quad (2a)$$

$$\Phi^{(SR)}(\text{Ga}; \text{Ga}) = \begin{pmatrix} C_1 & D_1 & E_1 \\ D_1 & C_1 & E_1 \\ -E_1 & -E_1 & F_1 \end{pmatrix}, \quad (2b)$$

and

$$\Phi^{(SR)}(\text{P}; \text{P}) = \begin{pmatrix} C_2 & D_2 & -E_2 \\ D_2 & C_2 & -E_2 \\ E_2 & E_2 & F_2 \end{pmatrix}, \quad (2c)$$

for interactions between NN's [Eq. (2a)] and 2NN's [Eqs. (2b) and (2c)], respectively. These Cartesian blocks must obey the transformation law⁹

$$\Phi_{\alpha\beta}(L, K; L', K') = \sum_{\mu, \nu} S_{\alpha\mu} S_{\beta\nu} \Phi_{\mu\nu}(l, \kappa; l', \kappa'), \quad (3)$$

where S is the point-group operation associated with the space-group transformation which takes the site (l, κ) into the site (l', κ') . In this expression, l, l', L , and L' label the N unit cells in the lattice, κ, κ', K , and K' specify the basis atom, and the remaining indices refer to Cartesian coordinates. Hence, from Eqs. (2), (3), and the translation-invariance condition,⁹

$$\Phi(l, \kappa; l, \kappa) = - \sum_{l', \kappa' \neq l, \kappa} \Phi(l, \kappa; l', \kappa'), \quad (4)$$

$\Phi^{(SR)}$ for the entire lattice is determined. The description of the bulk short-range interaction in terms of these 10 parameters ($A-F_2$) is the most general description allowed by symmetry, and it physically corresponds to both central and noncentral pair interactions.⁸

In addition to purely short-range forces, the DBA force-constant matrix contains a contribution from classical electrostatic interactions. Associated with each lattice site is an effective charge Z . Displacement of a charge from its equilibrium site effectively results in an electric dipole moment at the site. Dipoles may also be induced, either by the motion of neighboring atoms (mechanical polarizability N) or by the electric fields produced by other dipoles (electronic polarizability g). The dipoles, however generated, produce electric fields. These fields exert forces on the charges and mechanically induced dipoles, giving rise to the Coulomb term $\Phi^{(el)}$ of Eq. (1). Five parameters are used to determine $\Phi^{(el)}$, giving a total of 15 for the DBA.⁸ These 15 parameters have been determined for GaP by Kunc *et al.*⁸

B. Green's functions and group-theoretic considerations

The bulk Green's functions are numerically obtained from the eigenvalues and eigenvectors of the Fourier-transformed dynamical matrix in precisely the manner described in Ref. 7. From the bulk Green's functions the standard formalism¹⁰ is used to obtain the local modes as before.⁷ The major difference in the present work lies in the spatial extent of the defect considered. Here, the defect affects 17 atoms and, hence, 51 Cartesian coordinates. Thus, we are required to evaluate a 51×51 block of the bulk Green's-function matrix.¹⁰

We shall consider substitutional defects which retain the full point-group symmetry (T_d) of the lattice. Accordingly, it is natural and convenient to express the Green's-function matrix in a basis of "collective coordinates" which transform according to the irreducible representations of T_d . It can be readily shown that the 51-dimensional reducible representation Γ of T_d given in terms of Cartesian coordinates can be reduced to

$$\Gamma = 3A_1 \oplus A_2 \oplus 4E \oplus 5T_1 \oplus 8T_2. \quad (5)$$

The collective coordinates Q transforming according to the irreducible representations (A_1-T_2), are related to the original Cartesian coordinates by an orthogonal transformation. The collective coordinates have already been determined for the five-atom cluster.⁷ The additional collective coordinates needed for the 12-atom, 2NN shell are given in the Appendix.

The advantage of the collective-coordinate transformation is that matrices reflecting the T_d symmetry are block-diagonalized in the form^{7,9}

$$G_{\mu\nu, \sigma\rho}^{(s)(r)} = \delta_{(s)(r)} \delta_{\mu\nu} G_{\sigma\rho}^{(s)}, \quad (6)$$

where (s) and (r) label the irreducible representation. The block diagonalization allows us to consider each irreducible representation separately, providing a classification

scheme for the defect vibrational motion according to symmetry. For a given irreducible representation, μ and ν label the dimension, and σ and ρ label the occurrences (e.g., $\mu=1,2,3$ and $\sigma=1, \dots, 8$ for T_2). The form of the block diagonalization also restricts the number of independent matrix elements on the basis of symmetry. With the use of Eq. (6), the number of independent Green's-function matrix elements is reduced to 68.

C. Defect perturbation

The defect perturbation considered in this work consists of the mass substitution $m_P \rightarrow m_O$ at the defect site and a perturbation of the short-range force constants among the substituent and its NN's and 2NN's. We wish to consider a general force-constant perturbation $\delta\Phi$ having the block form of Eq. (2) and consistent with T_d symmetry. Let us label the O-Ga perturbation parameters δA and δB , the O-P parameters $\delta C, \dots, \delta F$, the Ga-P NN back-bond parameters $\delta A'$ and $\delta B'$, the intra-Ga-shell 2NN parameters $\delta C', \dots, \delta F'$, and the intra-P-shell 2NN parameters $\delta C'', \dots, \delta F''$. Now, not all these force-constant parameters may be chosen independently. Applying the infinitesimal-rotation-invariance condition,⁹ we find that

$$\delta E = \delta E' = \delta E'' = 0, \quad (7a)$$

$$\delta A' - \delta B' = 0, \quad (7b)$$

$$\delta A - \delta B = -2[(\delta C' - \delta D') + \delta F'], \quad (7c)$$

$$\delta F = -2(\delta C'' - \delta D''), \quad (7d)$$

$$2\delta F'' = -(\delta C - \delta D). \quad (7e)$$

The linear combinations of the form $\delta A - \delta B$ represent NN bond-bending spring constants.⁷ Similarly, $\delta C - \delta D$, δF , and the corresponding primed expressions may be viewed as *anisotropic* bond-bending springs between 2NN pairs, while the parameters δE correspond to a more complicated pair interaction. Essentially, Eqs. (7) impose constraints on the noncentral pair interactions possible within an *isolated* cluster having the geometry of our 17-atom defect. The results up to this point (given our above assumptions) are general, leaving nine free quantities to specify $\delta\Phi$.

We are now ready to parametrize the interaction perturbation. To reduce the number of free parameters, we assume the same fractional variation among *independent* O-Ga, O-P, and Ga-P parameters, giving

$$\delta A/A = \delta B/B = \eta_{O,Ga}, \quad (8a)$$

$$\delta C/C_2 = \delta D/D_2 = \delta F/F_2 = \eta_{O,P}, \quad (8b)$$

$$\delta A'/A = \eta_{Ga,P}. \quad (8c)$$

If we make the analogous assumptions, $\delta C'/C_1 = \delta D'/D_1 = \delta F'/F_1$ and $\delta C''/C_2 = \delta D''/D_2$, we see from Eqs. (7) that the interaction perturbation $\delta\Phi$ is completely specified in terms of the η 's. In this way, we specify directly the NN ($\eta_{O,Ga}$), the adjustable part of the 2NN ($\eta_{O,P}$), and the bond-stretching part, $\delta A' + 2\delta B' = 3\delta A'$, of the back-bond interactions ($\eta_{Ga,P}$). Other interactions within the cluster are then modified au-

tomatically according to rotation invariance.

The defect-perturbation matrix is now

$$\delta L = M^{-1/2} \delta \Phi M^{-1/2} - \omega^2 M^{-1} \delta M,$$

where δM contains the on-site mass perturbation. (Note that we have put the explicit mass dependence in δL rather than \underline{G}^0 , as in Ref. 7.) We numerically construct δL in Cartesian form, using Eqs. (2)–(4), (7), and (8), and then apply the transformation to collective coordinates. The local modes are given by the frequencies ω which solve¹⁰

$$\text{Re det}[1 - \underline{G}^0(\omega^2) \delta L(\omega^2)] = 0. \quad (9)$$

We solve such a determinantal equation for each irreducible representation. A useful quantity for characterizing the relative amount of motion of a certain symmetry type and at a particular frequency is the LDOS. The LDOS of the perturbed crystal is given by the diagonal elements of $-\text{Im} \underline{G}/\pi$, where the perturbed crystal Green's function is given by¹⁰

$$\underline{G} = (1 - \underline{G}^0 \delta L)^{-1} \underline{G}^0. \quad (10)$$

Strong resonant modes show up ideally as Lorentzian peaks in the LDOS while strictly localized modes appear as δ functions.⁷ For representations which have multiple occurrences in the space of the defect, the LDOS for each occurrence provides a measure of the fraction of total kinetic energy in that particular type of motion, and this quantity is used in the following sections to describe the composition of defect modes.

D. Restoring force for one-atom displacements

In the discussion to follow, it will be useful to know the effective spring constant acting on the O atom under a unit displacement from equilibrium. This spring constant is given by $k^{(\text{eff})} = k^{(\text{SR})} + k^{(\text{el})}$, where

$$k^{(\text{SR})} = -4[(A + \delta A) + 2(C_2 + \delta C) + (F_2 + \delta F)] \quad (11)$$

denotes the modified short-range part, and $k^{(\text{el})}$ is the bulk P-site Coulomb component. We wish to compute $k^{(\text{el})}$. In the notation of Maradudin,⁹ we have for the unit displacement $u_\beta(l', \kappa') = \delta_{\alpha\beta} \delta_{ll'} \delta_{\kappa\kappa'}$,

$$\begin{aligned} F_\alpha(l, \kappa) &= - \sum_{\beta, l', \kappa'} \Phi_{\alpha\beta}(l, \kappa; l', \kappa') \delta_{\alpha\beta} \delta_{ll'} \delta_{\kappa\kappa'} \\ &= - \Phi_{\alpha\alpha}(l, \kappa; l, \kappa), \end{aligned} \quad (12)$$

where $\Phi_{\alpha\alpha}(l, \kappa; l, \kappa) = k^{(\text{el})}$ for $\Phi = \Phi^{(\text{el})}$. Now, using the identity

$$\delta_{ll'} = \frac{1}{N} \sum_{\vec{k}} \exp\{-i\vec{k} \cdot [\vec{x}(l, \kappa) - \vec{x}(l', \kappa)]\} \quad (13)$$

in Eq. (12) gives

$$\begin{aligned} F_\alpha(l, \kappa) &= - \frac{1}{N} \sum_{\vec{k}} \left[\sum_{l'} \Phi_{\alpha\alpha}(l, \kappa; l', \kappa) \right. \\ &\quad \times \exp\{-i\vec{k} \cdot [\vec{x}(l, \kappa) - \vec{x}(l', \kappa)]\} \Big] \\ &= - \frac{1}{N} \sum_{\vec{k}} \hat{\Phi}_{\alpha\alpha}(\kappa, \vec{k}), \end{aligned} \quad (14)$$

where the inner sum has been identified as the Fourier-transformed force-constant matrix. Recognizing that our $\hat{\Phi}(\kappa, \kappa | \bar{k})$ transforms as $T_2 \otimes T_2$, we can restrict the summation over \bar{k} in Eq. (14) to the irreducible wedge W of the first Brillouin zone as in Ref. 7, obtaining finally

$$k^{(el)} = \frac{1}{N} \sum_{\bar{k} \in W} h_{\bar{k}} \sum_{\beta=1}^3 \text{Re}[\hat{\Phi}_{\beta\beta}^{(el)}(\kappa, \kappa | \bar{k})]. \quad (15)$$

This sum was evaluated numerically by a method similar to the numerical computation of $\text{Im} \mathcal{G}^0$ in this and in our previous work.⁷ The result is $k^{(el)} = -0.177k^{(SR)}$ for the bulk P site.

III. RESULTS

A. Bulk phonons

In Fig. 1 we show the bulk dispersion curves and bulk DOS for GaP as computed from the DBA. The DBA results constitute a substantial quantitative improvement over those of the two-parameter model used previously.⁷ The calculated LO_T and TO_T energies, 50.0 and 45.3 meV, respectively, are split due to Coulomb effects and are in agreement with measured values.⁸ The calculated TA_X energy is 12.8 meV compared with the actual value, 13.1 meV.¹¹ The bulk DOS presented here is highly structured compared with that of the two-parameter model.⁷ As we shall see, this structure gives rise to local-mode behavior not seen in the simpler model. In the units shown in the figure, the computed area under the bulk-DOS curve is 6.0004, compared to the exact theoretical value, 6.

B. Bulk Green's functions

We have computed the bulk Green's-function matrix \mathcal{G}^0 for both a P-centered and a Ga-centered 17-atom cluster. The method of computation is described in Ref. 7. The Green's functions were calculated as functions of $(\hbar\omega)^2$ at intervals of 2.5 meV² and then converted to functions of $E = \hbar\omega$ [see Eq. (9) of Ref. 7]. This corresponds to a resolution in E of about 0.5 meV near $E = 0$ and 0.025 meV at

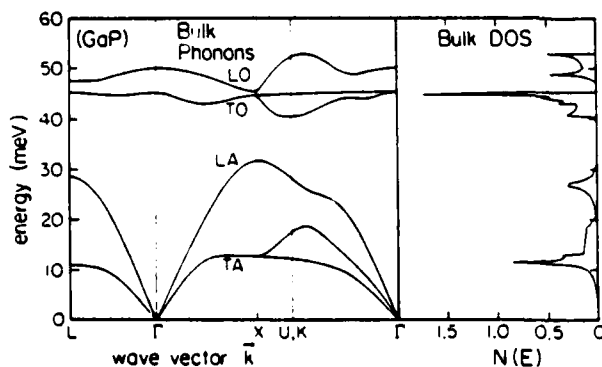


FIG. 1. Bulk-phonon dispersion curves and DOS for GaP calculated from the DBA. The calculated LO_T, TO_T, and TA_X energies are 50, 45.3, and 12.8 meV, respectively. The peaks in the bulk DOS lie at 11.3, 27, 44.8, 48.8, and 52.9 meV. In the units shown, the DOS integrates to 6.0004, compared with the exact value, 6.

$E = 50$ meV. There are 68 bulk Green's functions each for both the P- and Ga-centered clusters—too many to display individually. Instead, for each irreducible representation (s), we sum the diagonal matrix elements and present $\mathcal{D}^{(s)}(E)$ vs E in Fig. 2, where

$$\mathcal{D}^{(s)}(E) \equiv -\frac{1}{\pi} \text{Tr} \text{Im}[\mathcal{G}^{0(s)}(E)]. \quad (16)$$

The quantity $\mathcal{D}^{(s)}(E)$ is the partial DOS (Ref. 7) for the representation (s) and is proportional to the mean-squared amplitude of modes associated with (s)-type motion in the 17-atom cluster at energy E . In particular, the A_2 mode consists of 2NN motion only. From Fig. 2 we see that the P-centered, A_2 partial DOS has a large amplitude in the TO and small amplitude in the TA phonon branches, while the opposite is true for the Ga-centered DOS. This is because the P atoms undergo larger displacements in optical modes than do the heavier Ga atoms. For the discussion to follow, the important symmetries are A_1 and T_2 . A_1 modes consist of some combination of the following: "breathing" motion of the NN shell, 2NN breathing, and a third, more complicated 2NN motion. T_2 modes consist of defect-site motion along with collective motions within the NN and the 2NN shells. Only T_2 modes can involve defect-site motion. (See the Appendixes here and in Ref. 7 for a complete listing of the collective coordi-

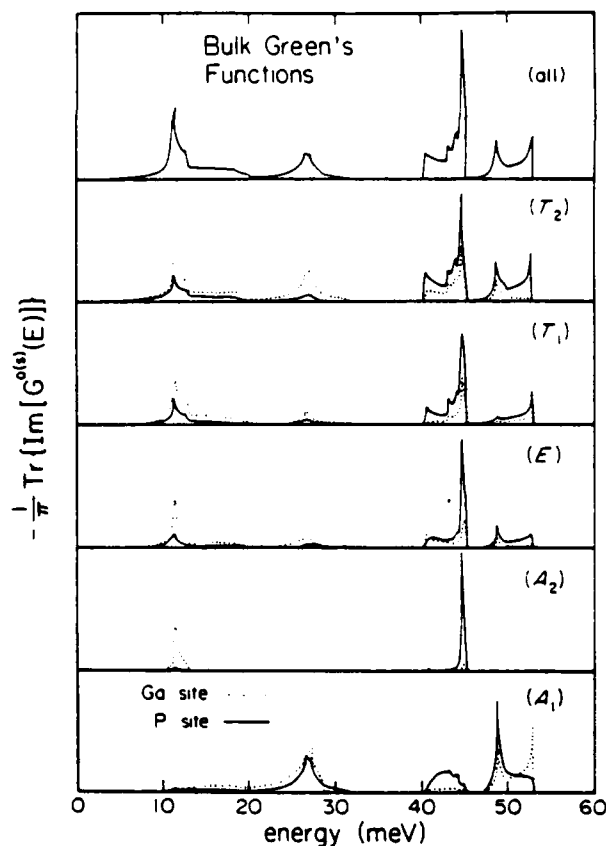


FIG. 2. Partial DOS of bulk GaP for the representations, A_1 – T_2 . Green's functions for P- and Ga-centered clusters are shown. The A_2 partial DOS involves 2NN motion only and for the P-centered (Ga-centered) cluster is larger at optical (acoustic) frequencies.

nates of the 17-atom cluster.)

Figure 2 gives the decomposition of the bulk DOS into the various representations of T_d appropriate for a point defect. The bulk DOS can be recovered from the various partial densities by performing the sum

$$\sum_{(s)=A_1}^{T_2} d_{(s)} [\mathcal{D}_P^{(s)}(E) + \mathcal{D}_{Ga}^{(s)}(E)] = 17N(E), \quad (17)$$

where $d_{(s)}$ is the dimensionality of the representation (s) . The renormalization factor of 17 on the right-hand side of Eq. (17) occurs because, in summing over both P- and Ga-centered clusters, the two-atom basis of GaP is included 17 times.

C. Local modes

Let us examine the local phonon modes of GaP:O_P as a function of the interaction perturbation. In Sec. IIC we have parametrized the interaction perturbation for GaP:O_P in terms of $\eta_{O,Ga}$, $\eta_{O,P}$, and $\eta_{Ga,P}$. Now, we feel physically motivated to require a further constraint between $\eta_{O,Ga}$ and $\eta_{O,P}$. It is natural to expect the O-P interaction to vanish when the O-Ga interaction vanishes, and the O-P interaction to have the bulk (P-P) value when the O-Ga interaction has the bulk (P-Ga) value. In this way we are led to consider defects for which $\eta_{O,Ga} = \eta_{O,P} = \eta$. In contrast, we expect the relation between the back bonds ($\eta_{Ga,P}$) and our newly defined η to depend on details of the defect chemistry well beyond the scope of this paper. In practice, we have found that the effect of the parameter $\eta_{Ga,P}$ is to "turn on" certain 2NN-shell local modes while not appreciably affecting those low-shell modes which have a strong dependence on η . Therefore, for the purpose of presentation, we choose (see Sec. IV) $\eta_{Ga,P} = 0.12\eta$ and present our results as a function of the single parameter, η .

The local modes of GaP:O_P as a function of the perturbing force-constant parameter η are shown in Fig. 3. Only A_1 and T_2 modes satisfying Eq. (9) are shown here. Modes of A_2 , E , and T_1 symmetry also occur, but are omitted for clarity. η ranges from -1 , corresponding to removal of the short-range O-Ga and O-P interactions, through 0, where all interactions have their bulk values, to $+1$. The effective O-site restoring force, $k^{(eff)} = (1 + \eta - 0.177)/(1 - 0.177)$, normalized to the bulk P-site value, is indicated along the top of the figure while the bulk DOS adjoins on the left. Note that the shaded region below the value $k^{(eff)} = 0$ is unphysical.

The important features of Fig. 3 are the steep T_2 branch in the energy range near 12–40 meV, the lowest-lying T_2 branches (around 10 meV), the low-energy A_1 branch (20–35 meV), and the high-energy A_1 branch (45–55 meV). The steep T_2 branch was seen in our earlier model⁷ and consists mainly of O-atom motion. Also seen in our earlier work was the low-energy A_1 branch. In the present work, this A_1 branch, consisting of over 95% NN breathing, has been pulled up to higher energies ($\eta < 0$) in better agreement with experiment, as we shall see below. Two significant features appear in the present work not obtained previously. One is the high-energy A_1

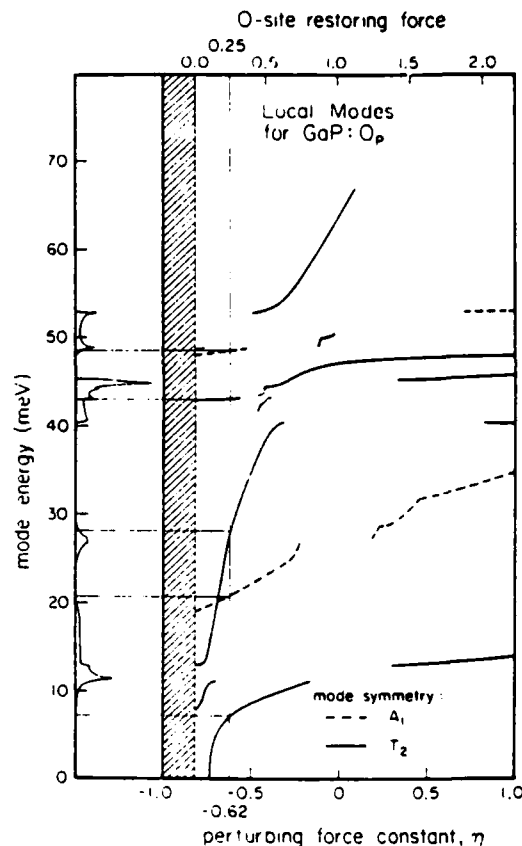


FIG. 3. A_1 and T_2 local-mode energies for GaP:O_P as a function of the short-range force-constant perturbation η discussed in the text. For $\eta = -0.62$ the A_1 -mode energies are 20.4 and 48.2 meV and the T_2 -mode energies are 7.3, 28.2, and 43.1 meV. The shaded region is unphysical. The DOS for bulk GaP adjoins on the left.

branch, which appears only upon perturbation of the Ga-P back-bond force constants and involves mostly 2NN-breathing motion. The other is the low-energy T_2 branch. This T_2 branch is primarily composed of Ga-shell, bond-stretching motion ($E \geq 6$ meV) and seems to appear for $\eta < 0$ only when the bulk model includes 2NN interactions.

In Sec. IV we shall see that the O⁰ defect is well described by the perturbation $\eta = -0.62$. This corresponds to a $k^{(eff)}$ of 25% of the bulk value. The local-mode energies at $\eta = -0.62$ are indicated in the caption of Fig. 3. Next, in Fig. 4, we compare the A_1 bulk and defect partial DOS for $\eta = -0.62$. These are decomposed into their Ga- and P-shell parts, showing the relative energy of motion associated with each shell at a given mode "energy," $E = \hbar\omega$. From the top curve in Fig. 4 we see resonant modes at 20.4 and 48.2 meV. The 20.4-meV mode is a rather broad resonance of width ~ 5 meV and involves mainly NN Ga motion (96%) as mentioned above. The resonant mode at 48.2 meV is sharper (~ 0.5 meV) and consists of motion (97%) of the less massive P atoms. It is evident from the figure that both resonant modes occur at frequencies appreciably different from the bulk peaks, and hence are characteristic of the defect. In contrast, local modes confined near singular features in

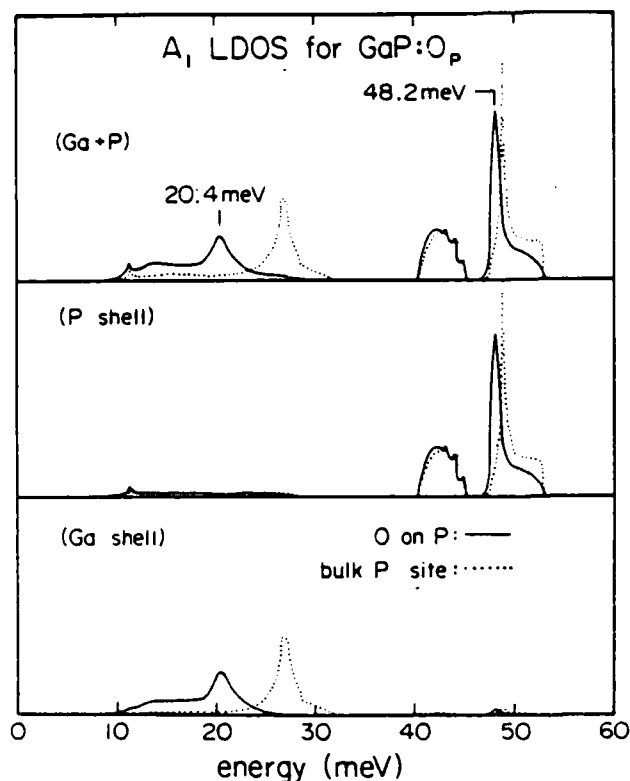


FIG. 4. A_1 LDOS for GaP:O_p decomposed into Ga- and P-shell components. The corresponding bulk partial DOS's are included for comparison. The 20.4-meV resonance involves mostly Ga-shell motion, while the resonance at 48.2 meV consists mainly of P-shell motion. All curves have the same scale.

the bulk partial DOS may also, in general, occur. Such modes evidently couple strongly to bulk modes and are thereby more "bulklike," i.e., more spatially delocalized in character.

We show the T_2 LDOS for GaP:O_p at $\eta = -0.62$ in Fig. 5, once again decomposed into contributions from O, Ga, and P shells. The mode energies which solve Eq. (9) are indicated on the top curve. Twin resonance peaks at 25.0 and 28.2 meV are seen in the O-site LDOS, occurring just above and just below the 27-meV LA peak in the bulk DOS. The 28.2-meV mode consists of 86% O-, 8% Ga-, and 6% P-shell motion, and the 25.0-meV mode consists of 70% O-, 20% Ga-, and 10% P-shell motion, within the 17-atom cluster. We note that at $\eta = -0.62$ only the mode at 28.2 meV is a solution of Eq. (9). The twin-peak structure appears to be the result of coupling between isolated-defect and nearby bulk LA-phonon modes. The 27-meV LA peak in the bulk DOS involves very little P-sublattice motion. Thus, a mode involving large O motion cannot exist at 27 meV, and when $\eta \rightarrow -0.62$ the O mode splits into two modes. Both O-site peaks occur at energies different from bulk peaks and are well localized near the O atom, and upon the substitution of ^{18}O for ^{16}O , both peak positions undergo a shift in energy. The 25.0- and 28.2-meV resonances are, therefore, local rather than bulklike in character. In contrast, the weak mode at 43.1 meV is pinned to a van Hove singularity in the bulk DOS (see

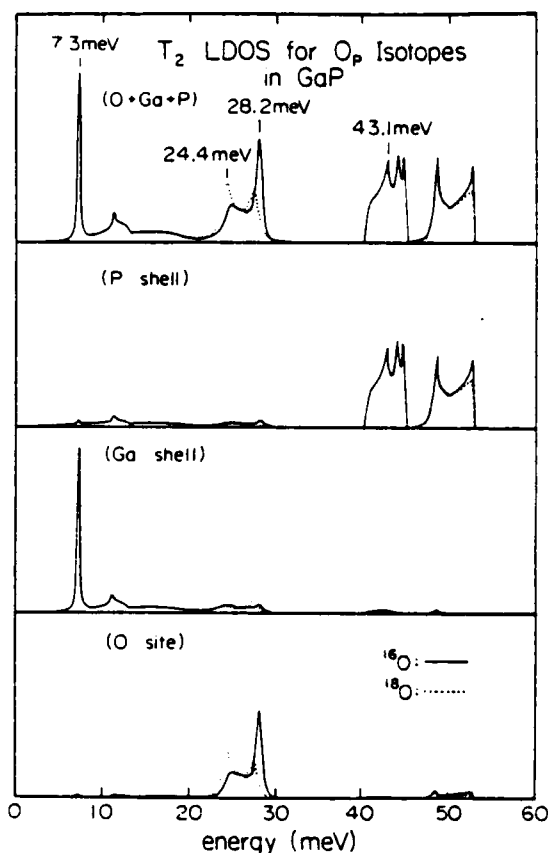


FIG. 5. T_2 LDOS of Ga:O_p for isotopes ^{16}O and ^{18}O decomposed into O-atom, NN-shell, and 2NN-shell parts. The twin resonances centered near 25 meV primarily involve O-atom motion and undergo isotope shifts. Other resonant modes occur at 7.3 meV (Ga shell) and 43.1 meV (bulklike P shell). All curves have the same scale.

Fig. 3) and is evidently somewhat more bulklike. Finally, the sharp resonance at 7.3 meV primarily involves Ga-shell motion (94%) along with small P (5%) and O (1%) contributions.

IV. DISCUSSION

A. Intensity of phonon replicas

The intensity of phonon-assisted optical transitions at defects have been thoroughly discussed by Rebane.¹² Selection rules for determining which transitions are allowed are similar to those used for molecules, as discussed by Herzberg.¹³ Allowed transitions are those for which the dipole matrix element

$$\langle \Psi_m(r, R) \Phi_m(R) | D_e(r) | \Psi_l(r, R) \Phi_l(R) \rangle$$

is nonzero. Here, Ψ is the electronic wave function, Φ is the vibrational wave function, l and m label electronic states, i and j label vibrational states, r is the set of all electron coordinates, R is the set of all nuclear coordinates, and $D_e(r) = -e \sum_i r_i$ is the electronic dipole moment operator. In place of the nuclear coordinates R , we introduce new coordinates Q_l , which are the normal coordinates.

dinates of the vibrational problem. These normal coordinates may be chosen to form bases for irreducible representations $\Gamma(Q_i)$ of the symmetry group of the imperfect crystal, where $\Gamma(x)$ refers to the representation according to which x transforms. We assume that the same set of normal coordinates may be used for both the initial and final electronic states (though the equilibrium values of these coordinates will depend on the electronic state). The total vibrational wave function can now be written as

$$\Phi_{|i_s|} = \prod_i \phi_{i_s}(Q_i), \quad (18)$$

where i_s labels the occupation of the s th normal coordinate. The harmonic-oscillator functions ϕ are even with respect to their arguments for even occupation, and odd for odd occupation. By inspection, in the vibrational ground state ($i_s = 0$ for all s) the wave function $\Phi_{|i_s|}$ is totally symmetric. For multiple one-phonon occupation, Φ transforms as $\prod_{i_s=1} \Gamma(Q_i)$, where the product runs over all s such that $i_s = 1$.

As an example of the above discussion, consider a defect with T_d symmetry, in which case the dipole moment transforms as T_2 . An $A_1 \rightarrow A_1$ electronic transition is forbidden, but if one T_2 phonon is involved, the dipole matrix element transforms as

$$A_1 \otimes A_1 \otimes T_2 \otimes A_1 \otimes T_2 = A_1 \otimes E \otimes T_1 \otimes T_2,$$

which is allowed. Similarly, an $A_1 \rightarrow T_2$ electronic transition is allowed, and participation of a single A_1 phonon or a single T_2 phonon is also allowed since

$$A_1 \otimes A_1 \otimes T_2 \otimes T_2 \otimes A_1 \text{ and } A_1 \otimes A_1 \otimes T_2 \otimes T_2 \otimes T_2$$

both contain A_1 . The intensity of phonon replicas is governed by the Franck-Condon principle.^{12,13} Essential-

ly, this principle states that the phonon replicas which will be observed in a transition are those which describe the change in equilibrium position of the atoms between the initial and final states. In other words, if the atoms move along some coordinate Q between their initial and final states, normal modes of the type Q will be strongly excited in the transition.

We can use this principle to demonstrate that "antisymmetric," i.e., not totally symmetric, phonons cannot be strongly excited. If some antisymmetric vibrational mode is strongly excited, this necessarily leads to a change in the symmetry of the system, and in the new symmetry group the vibrational mode is totally symmetric. However, for weak excitation of the antisymmetric vibrations, this change in symmetry can be neglected. Thus, in electronically allowed transitions, totally symmetric vibrations will predominate, and in electronically forbidden transitions, the occupation of the dominant antisymmetric modes changes by one.

B. Comparison of theory and experiment

In Table I we compare our theoretical results with the phonon energies observed in the optical spectra of the O^+ and O^0 defects. The apparent agreement between theory and experiment is achieved partly by matching unknown theoretical parameters with experiment, and partly by the predictive powers of the theory itself. If we view the bulk phonon dispersion curves as input to the theory, then the only unknown is the interaction perturbation within the 17-atom cluster. We have parametrized the interaction perturbation [Eqs. (8)] in Sec. IIC and have invoked the further restriction, $\eta_{O,Ga} = \eta_{O,P} = \eta$ in Sec. IIIC, so that the total number of unknown parameters is two. We determine values for these parameters by matching the en-

TABLE I. Energies (meV) of the phonons associated with the O^0 and O^+ defect in GaP. $^{16}O \rightarrow ^{18}O$ isotope shifts (meV) are given in parentheses following the energies. Tentative identifications are indicated by "?."

Label	Expt.	Theory	Identification
Zn-O	6.0 ^a	7.3	defect (T_2 , Ga shell)
TA	13.1 ^b	11.5	bulk (TA)
a_1 (Ga)	19.5, ^c 19 ^d	20.4	defect (A_1 , Ga shell)
loc	24.7(-1.6) ^b	25.0(-0.6)	defect (T_2 , O atom)
loc'	28.4(-0.5) ^b	28.2(-0.7)	defect (T_2 , O atom)
A	43.0 ^b	43.1	defect (T_2 , P shell)?
TO	44.8 ^b	44.8	bulk (TO)
e(P)	...	45.3	defect (E, P shell)
t_1 (P)	...	45.4	defect (T_1 , P shell)
a_2 (P)	...	45.8	defect (A_2 , P shell)
B	46.1, ^b 46.4, ^c 46.5 ^e	48.8	defect (T_2 , P shell)?
a_1 (P)	47.5, ^b 47, ^f 48 ^d	48.2	defect (A_1 , P shell)
C	48.7, ^b 48.8 ^c	48.8	bulk (LO)
LO _r	49.8 ^b	50.0	bulk (LO _r)

^a Reference 17.

^b Reference 2, capture-luminescence spectrum.

^c Reference 2, luminescence-excitation spectrum.

^d Reference 3.

^e Reference 14.

^f Reference 1.

ergies of theoretical modes with those observed. The theory then predicts a number of other vibrational modes not involved in the matching process with which we identify observed phonons. In this way we determine the symmetry and character of almost all of the phonon modes associated with the O^+ and O^0 defects. Strictly speaking, all of the phonons observed in the optical spectra involve some component of defect motion (i.e., O-atom, nearest Ga-shell, or nearest P-shell motion). However, certain phonons involve much more defect motion than others, and it is useful to separate the modes into those which are associated largely with the defect and those which are bulklike. In Table I we have classified the modes as such. The theoretical defect-mode energies are taken from peaks in the LDOS, and the theoretical bulk phonon energies are taken from peaks in the bulk DOS or critical points in the dispersion curves.

A set of very interesting phonon sidebands associated with the neutral oxygen defect O^0 occur in the capture luminescence of Dean and Henry.² Here, intense phonon resonances near 25 meV are observed to involve significant O motion since they shift under the isotopic substitution, $^{16}O \rightarrow ^{18}O$ and must therefore be T_2 modes. Since the O mass is less than that of P, these low-energy resonances imply reduced O-neighbor force constants relative to the bulk force constants. This force-constant reduction was first estimated by Feenstra and McGill¹⁴ to be 30%, and later estimated by Baraff, Kane, and Schlüter¹⁵ to be 20%; both estimates were based on simple molecular-type vibrational models. Subsequent NN Green's-function results⁷ yield an estimate of 15%. In the present model, if we assume the same fractional reduction for O-Ga and O-P force constants, the best value for the purely short-range force-constant reduction is $\eta = -0.62$. After including Coulomb effects between the O atom and the rest of the lattice, this corresponds to a total effective force constant ($k^{(eff)}$) of 3.5 eV/\AA^2 , which is 25% of the bulk, P-site value. We emphasize, though, that $k^{(eff)}$ includes long-range Coulomb effects from the entire lattice and must not be viewed simply as an equivalent short-range force constant. Our LDOS for T_2 modes, summed over the O atom, Ga shell, and P shell, is shown in Fig. 5. The theoretical peak energies and isotope shifts listed in Table I compare reasonably well with experiment.

Having determined the O-neighbor force constants, the theory predicts an A_1 mode at 20.4 meV. We identify this mode with the observed 19-meV phonon listed in Table I. As discussed by Morgan⁴ and also in Sec. IV A, the observed intensities of this 19-meV mode and the prominent 47-meV mode indicate that these modes have A_1 symmetry. To produce a defect mode of A_1 symmetry near 47 meV, it is necessary to reduce the back-bond Ga-P force constants from their bulk values. We arbitrarily choose to reduce the Ga-P force constants by 12% of the O-neighbor reduction, resulting in $\eta_{Ga,P} = -0.0744$ for the Ga-P interactions and yielding an A_1 mode at 48.2 meV. Further reductions in the Ga-P force constants reduce the energy of this mode, bringing it closer to the observed value. However, considering the uncertainties associated with our calculated optical phonons, we feel that an accurate determination of these back-bond Ga-P interactions is

outside the range of our theory. Suffice it to say that our computations do yield an A_1 mode in the optical branch and that the back-bond Ga-P interactions are reduced from their bulk values.

A number of phonon replicas in the optical branch are seen in the optical spectra of Dean and Henry.² We identify the symmetry and nature of these phonons as indicated in Table I. Some of these optical-phonon replicas are weak, and considering the uncertainty of our optical-phonon computations, those identifications we feel should be regarded as tentative are marked by "?." The $a_1(P)$ phonon has been discussed above. The phonon labeled B we take to be a defect mode since its energy falls well away from peaks in the bulk DOS. This phonon is observed in capture-luminescence and luminescence-excitation spectra,² and is also seen in the near-neighbor ($m=4$ and 5) Zn-O pair spectrum¹⁴ (labeled O in that spectrum). Considering the proximity of the donor-acceptor impurities in the latter case, it seems that this 46.5-meV mode corresponds to atomic motion which is directed along the donor-acceptor axis, i.e., a T_2 mode with respect to the T_d symmetry of an isolated O impurity. The 46.1-meV B phonon in the capture-luminescence spectrum most likely has T_2 symmetry,⁴ although the 46.4-meV mode seen in luminescence-excitation spectra could transform as either A_1 or T_2 , as discussed in Sec. IV A. For now, we group all three of these modes together with the label B in Table I, and we tentatively identify them with a computed T_2 resonance at 48.8 meV which is strongly tied to a LO peak in the bulk DOS (see Figs. 3 and 5).

Another T_2 defect mode occurs in the theory at 43.1 meV, and this mode we tentatively associate with the observed 43.0-meV phonon labeled A . The 49.8-meV phonon identified by Dean and Henry as LO_T is in agreement with our computed 50.0-meV LO_T -phonon energy. The mode labeled C we associate with the prominent peak in the bulk DOS occurring at 48.8 meV, while we associate the observed 44.8-meV mode with the very prominent TO peak in the bulk DOS occurring at 44.8 meV. In both of these cases, the peaks in the bulk DOS do not correspond to phonons at or near critical points in the Brillouin zone, but rather are associated with phonons in the interior of the zone. Finally, with regard to defect modes in the optical branch, we note that the present theory neglects defect-induced electrostatic interactions, and such effects are known to cause vibrational modes split off from the LO branch.¹⁶

We now come to the entry in Table I labeled Zn-O. This 6.0-meV mode is just barely resolved in the NN Zn-O pair spectrum of Henry, Dean, and Cuthbert¹⁷ (a related mode¹⁴ is seen at 9.2 meV for 2NN Zn-O pairs). Although the computational results presented here apply to the isolated O defect, simply replacing a NN Ga with a Zn atom changes the phonon energies by less than 0.1 meV since Ga and Zn have almost the same mass. Further force-constant variations of the Zn-O, Zn-P, or Zn-Ga interactions could affect the mode energies, but we assume that these variations are not significant. The presence of the Zn atom will, however, drastically affect the selection rules for observing phonons. In particular, all

modes which are T_2 for isolated O are now split to $A_1 \oplus E$, and strong phonon replicas of the allowed electronic transition transform as A_1 . Thus, the low-energy T_2 mode in Fig. 5 should appear in the Zn-O spectrum, and we identify it with the observed 6.0-meV mode. The theoretical "eigenvector" for this mode is shown in Fig. 6. We plot the displacement eigenvector, $u = M^{-1/2}\xi$, satisfying the eigenvalue equation

$$[1 - G^0(\omega^2)\delta L(\omega^2)]\xi = \lambda(\omega^2)\xi \quad (19)$$

at the resonant frequency, $\hbar\omega = 7.3$ meV, for which $\text{Re}\lambda = 0$.¹⁸ Now, the actual defect normal mode, given by $(1 - G^0\delta L)\xi = 0$, requires a complex value of ω for its solution. However, since $\text{Im}\lambda$ is proportional to the resonance width, we expect, for the very sharp 7.3-meV mode, that ω is near the real axis so that Eq. (19) gives a reasonable representation of the atomic motion in this case. It has been argued that this particular resonant mode plays an essential role in the dissociation of Zn-O pairs.¹⁴ In particular, the atomic motions which occur during the early stages of the dissociation may be as shown in Fig. 6. It is seen that the amplitude of Zn-atom motion is roughly 3 times that of oxygen. Thus, we conclude that in the pair dissociation it is the Zn atom which jumps to an interstitial site and diffuses away.

The vibrational modes of NN Cd-O pairs have been observed in optical spectra,^{17,19,20} and can be qualitatively understood on the basis of our calculations. The Cd-O modes will be similar to the Zn-O modes, except that those vibrations involving significant Cd motion will be shifted down in energy. Replicas of the electronically allowed A line should have A_1 symmetry for the point group C_{3v} , i.e., the A_1 modes and the A_1 component of the T_2 modes for isolated oxygen.¹⁹ In emission, Henry, Dean, Thomas, and Hopfield observe local modes at 7.0, 47.3, and 49.7 meV.²⁰ The 7.0-meV mode is similar to the 6.0-meV Zn-O mode discussed above. Thus, this mode involves mainly Cd motion in agreement with the observed

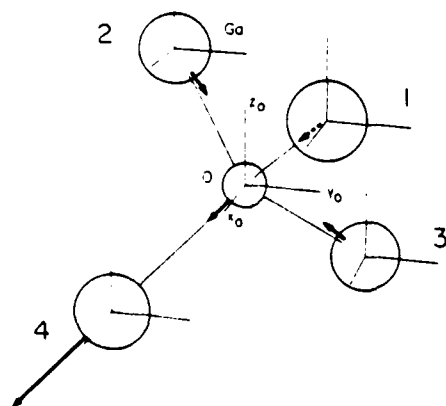


FIG. 6. "Eigenvector" for the 7.3-meV T_2 mode. The atomic displacements are indicated for the O and its four Ga neighbors. The $Ga_{(4)}$ and O displacements (in the ratio 3.4:1) both lie along the bond direction. The eigenvector has C_{3v} symmetry relative to the O-Ga₍₄₎ bond. With Zn in place of the Ga₍₄₎ atom, this is the predominant motion involved in the dissociation of Zn-O pairs (see text).

isotope shift.¹⁷ The optical resonances at 47.3 and 49.7 meV are probably associated with the defect B and $a_1(P)$ modes, thus involving mainly P-shell motion. From the intensities of the observed phonon replicas we conclude that in the optical transition the major atomic motion is that of the Cd atom moving relative to the almost stationary O atom. A number of Γ_3 phonons are reported²⁰ which produce replicas of the forbidden B line. Theoretically, we expect these to arise from the E modes and the E components of the T_1 and T_2 modes for isolated oxygen. As shown in Table I we do compute various E and T_1 modes. All these modes are very sharp (width of ~ 0.1 meV) and are tied to singularities in the bulk DOS. These modes could account for some of the observed Γ_3 modes, and the E components of the T_2 mode at 43.1 meV may also contribute. Our optical-phonon energies really are not accurate enough to make a definitive identification of these observed Γ_3 phonons.

Let us consider what our calculations tell us about the nature of the oxygen defect. In particular, two opposing models^{21,22} presently exist for this defect, and it is desirable to try to choose between them based on our results. First, the defect we are considering in our calculations is only a model, without the same detailed properties of the actual oxygen defect although their general properties should be similar. The most important result from our calculations is the O-lattice effective force constant, 3.5 eV/Å². This number is accurate to within, perhaps, 10%, and so provides a test of the opposing models. Unfortunately, it is very difficult to accurately obtain the defect force constant from the existing theoretical models. To date, Baraff *et al.*¹⁵ have attempted such a calculation for the classical model^{6,22} and have obtained an O-Ga stretching constant of 4.4 eV/Å², corresponding to an effective force constant of $4(4.4)/3 = 5.9$ eV/Å², a result which is somewhat too large. Nobody has yet attempted a similar computation for the weak-bonding model,²¹ although the computed bond strength should be significantly different for the two models as they contain different numbers of bonding and antibonding electrons.²³ Morgan has recently argued that the observed structure near 25 meV in the O⁰ phonon sidebands is due to a dynamic Jahn-Teller distortion of the O⁰ defect.²³ Although such a distortion could occur, our calculations demonstrate that it is not necessary to invoke this mechanism in order to account for the observed structure. With one free parameter (η), we have obtained quantitative agreement between experiment and theory for those phonon energies, isotope shifts, and intensities.

One basis for the weak-bonding model²¹ is the 19-meV $a_1(Ga)$ phonon, present in donor-acceptor-pair (DAP) spectra,^{1,3} but apparently absent in photoluminescence-excitation (PLE) spectra.² According to our calculations, this mode is rather broad as seen in the Ga-shell A_1 LDOS for O on a P site, shown in Fig. 4. Clearly, this resonance is distributed throughout the acoustic branch, so let us take its "width" to be 5 meV. This width has no consequence in the DAP spectrum due to the greater-than-10-meV broadening caused by a distribution of pair separations. But in the PLE spectrum, the no-phonon line is relatively sharp, so that the ratio of peak heights be-

tween an $a_1(\text{Ga})$ -phonon—assisted line and a no-phonon line is significantly reduced from the DAP spectrum. Additional broadening for the phonon-assisted line is also possible; the 20.4-meV Ga-shell peak in the A_1 LDOS for O on a P site shown in Fig. 4 represents mainly NN Ga motion. Motion of further-lying Ga shells will be concentrated at energies closer to 27 meV, and the actual phonon sideband probably involves some combination of these motions. We feel that a calculation of these broadening effects would be useful in order to quantify the apparent "anomaly."²¹

V. CONCLUSION

The major results of this paper are concerned with the existence of defect vibrational modes, including both strictly localized and resonant modes. It is impossible to determine the number of such modes by group theory alone since the existence of a mode is determined by a quantitative parameter: the degree of localization around the defect. Thus, it is necessary to undertake a computation of the vibrational modes of a defect. The theory we use for this purpose is a phenomenological one in which the force constants of the perfect lattice and those of the defect are all chosen to match experiment. Bulk phonons are described by a 15-parameter model which includes NN and 2NN plus electrostatic interactions. A defect is then introduced by perturbing the mass of an atom and perturbing its NN and 2NN force constants. A Green's-function technique is used to evaluate the LDOS near the defect, and thereby determine the presence of defect modes.

Our theoretical results are compared with experiment for the GaP:O_P defect. We use a two-parameter description of the short-range interaction perturbation near the O site. By a suitable choice of these two defect force constants we have obtained quantitative agreement with observed phonon modes involving O⁺ and O⁰ defects. For O-neighbor (i.e., O-Ga and O-P) and Ga-P (back-bond) short-range defect force constants at 38% and 93% of their respective bulk values, our calculations predict two A_1 modes and two T_2 modes which are reasonably localized at or near the defect, and also, other modes which are more bulklike in nature. We summarize the character of the four most localized modes as follows.

(1) *O-atom T_2 mode.* This mode involves mainly O-atom motion, and this motion is localized near the defect for practically any value of the defect force constants. To match the observed phonon energies near 25 meV, our choice of defect force constants correspond to an O-lattice effective force constant (taking all long-range and short-range interactions into account) of 3.5 eV/Å², which is 25% of the bulk, P-lattice value. This force constant may be compared with that obtained by assuming that the observed phonon is completely localized on the oxygen impurity, $(25 \text{ meV}/\hbar)^2 m_{\text{O}} = 2.4 \text{ eV}/\text{Å}^2$. Our calculations demonstrate that the observed two-peak structure in this resonant mode is due to coupling with LA bulk phonons.

(2) *Ga-shell T_2 mode.* This mode involves mainly vectorlike motion of the shell of Ga atoms surrounding the O impurity. The mode originates from the TA peak in

bulk-phonon DOS, and is significantly localized around the defect for values of the O-neighbor force constants which are about 80% or less of the bulk values. Experimentally, this mode is not seen in spectra involving isolated O impurities, but is seen when a Zn or Cd atom is located near the O atom, thereby lowering the symmetry of the system.

(3) *Ga-shell A_1 mode.* This mode is a breathing motion of the Ga shell. The mode originates at the peak in the LA bulk-phonon DOS and is localized for values of the O-neighbor force constants which are about 80% or less of the bulk values. This resonant mode is relatively broad with a width of about 5 meV (in agreement with experiment).

(4) *P-shell A_1 mode.* This mode mainly involves breathing motion of the P shell (2NN's) surrounding the O atom. The mode originates at the LO peak in the bulk DOS, and appears when the Ga-P back-bond interactions are reduced to 95% or less of the bulk values.

For all of the four defect modes discussed above, we feel that our theoretical description is fairly close to experiment in terms of energies and eigenvectors. We have demonstrated that the O⁺ and O⁰ defects are weakly bound in GaP, as expected, and that the Ga-P back bonds appear to be weakened. Our predicted two-peak, O-atom T_2 mode shows that the experimental results for the O⁰ defect are consistent with a T_d -symmetric geometry. Finally, our calculations identify the predominant atomic motion involved in the dissociation of Zn-O pairs in GaP.

ACKNOWLEDGMENTS

We gratefully acknowledge the support of the Office of Naval Research under Contract No. N00014-81K-0305. One of us (R.M.F.) has profited from the insights of T. N. Morgan.

APPENDIX

We have determined the collective coordinates Q for the 12-atom, 2NN shell seen by a substitutional defect in a zinc-blende lattice. The collective coordinates form bases for the irreducible representations of the symmetry group of the 2NN shell, namely O_h . The equilibrium positions of the 12 atoms in the 2NN shell are given (in units of $a_0/2$) by

$$\begin{aligned}\bar{\mathbf{r}}_1 &= -\bar{\mathbf{r}}_7 = (0, 1, 1), & \bar{\mathbf{r}}_2 &= -\bar{\mathbf{r}}_8 = (1, 0, 1), \\ \bar{\mathbf{r}}_3 &= -\bar{\mathbf{r}}_9 = (1, 1, 0), & \bar{\mathbf{r}}_4 &= -\bar{\mathbf{r}}_{10} = (-1, 1, 0), \\ \bar{\mathbf{r}}_5 &= -\bar{\mathbf{r}}_{11} = (0, -1, 1), & \bar{\mathbf{r}}_6 &= -\bar{\mathbf{r}}_{12} = (1, 0, -1),\end{aligned}\quad (\text{A1})$$

where a_0 is the edge length of the conventional unit cell. The 36 collective coordinates Q are related by an orthogonal transformation to the 36 Cartesian displacements, (x_i, y_i, z_i) , of atom i from equilibrium, where $i = 1, \dots, 12$. The explicit form of this orthogonal transformation is given in Table II. In this work, the

TABLE II. 36 collective coordinates Q for the 12-atom, 2NN shell. The (unnormalized) components associated with the atoms $i = 1, \dots, 6$ are given explicitly. The components associated with the remaining atoms ($i = 7, \dots, 12$) are obtained by multiplying the entire row of coefficients by the sign indicated. The irreducible representation of the T_d group according to which the collective coordinates transform are also indicated.

Q	(s)	x_1	y_1	z_1	x_2	y_2	z_2	x_3	y_3	z_3	x_4	y_4	z_4	x_5	y_5	z_5	x_6	y_6	z_6	(+ or -)
Q_1	A_1	0	1	1	1	0	1	1	1	0	$\bar{1}$	1	0	0	$\bar{1}$	1	1	0	$\bar{1}$	-
Q_2	A_1	1	0	0	0	1	0	0	0	1	0	0	$\bar{1}$	$\bar{1}$	0	0	0	$\bar{1}$	0	+
Q_3	A_2	0	$\bar{1}$	1	1	0	$\bar{1}$	$\bar{1}$	1	0	1	1	0	0	1	1	1	0	1	-
Q_4	E	0	1	1	1	0	1	$\bar{2}$	$\bar{2}$	0	2	$\bar{2}$	0	0	$\bar{1}$	1	1	0	$\bar{1}$	-
Q_5	E	0	$\bar{1}$	$\bar{1}$	1	0	1	0	0	0	0	0	0	0	1	$\bar{1}$	1	0	$\bar{1}$	-
Q_6	E	0	$\bar{1}$	1	$\bar{1}$	0	1	0	0	0	0	0	0	0	1	1	$\bar{1}$	0	$\bar{1}$	-
Q_7	E	0	$\bar{1}$	1	1	0	$\bar{1}$	2	$\bar{2}$	0	$\bar{2}$	$\bar{2}$	0	0	1	1	1	0	1	-
Q_8	E	1	0	0	0	1	0	0	0	$\bar{2}$	0	0	2	$\bar{1}$	0	0	0	$\bar{1}$	0	+
Q_9	E	$\bar{1}$	0	0	0	1	0	0	0	0	0	0	0	1	0	0	0	$\bar{1}$	0	+
Q_{10}	T_1	0	0	0	0	$\bar{1}$	0	0	0	1	0	0	1	0	0	0	0	1	0	-
Q_{11}	T_1	1	0	0	0	0	0	0	0	$\bar{1}$	0	0	1	1	0	0	0	0	0	-
Q_{12}	T_1	$\bar{1}$	0	0	0	1	0	0	0	0	0	0	0	1	0	0	0	1	0	-
Q_{13}	T_1	0	$\bar{1}$	1	0	0	0	0	0	0	0	0	0	0	$\bar{1}$	$\bar{1}$	0	0	0	-
Q_{14}	T_1	0	0	0	1	0	$\bar{1}$	0	0	0	0	0	0	0	0	0	$\bar{1}$	0	$\bar{1}$	-
Q_{15}	T_1	0	0	0	0	0	0	$\bar{1}$	1	0	$\bar{1}$	$\bar{1}$	0	0	0	0	0	0	0	-
Q_{16}	T_1	0	0	0	1	0	$\bar{1}$	$\bar{1}$	1	0	$\bar{1}$	$\bar{1}$	0	0	0	0	1	0	1	+
Q_{17}	T_1	0	$\bar{1}$	1	0	0	0	$\bar{1}$	1	0	1	1	0	0	$\bar{1}$	$\bar{1}$	0	0	0	+
Q_{18}	T_1	0	$\bar{1}$	1	1	0	$\bar{1}$	0	0	0	0	0	0	0	1	1	$\bar{1}$	0	$\bar{1}$	+
Q_{19}	T_1	0	0	0	$\bar{1}$	0	$\bar{1}$	1	1	0	1	$\bar{1}$	0	0	0	0	$\bar{1}$	0	1	+
Q_{20}	T_1	0	1	1	0	0	0	$\bar{1}$	$\bar{1}$	0	1	$\bar{1}$	0	0	1	$\bar{1}$	0	0	0	+
Q_{21}	T_1	0	$\bar{1}$	$\bar{1}$	1	0	1	0	0	0	0	0	0	0	1	$\bar{1}$	$\bar{1}$	0	1	+
Q_{22}	T_2	0	0	0	1	0	1	1	1	0	1	$\bar{1}$	0	0	0	0	1	0	$\bar{1}$	+
Q_{23}	T_2	0	1	1	0	0	0	1	1	0	$\bar{1}$	1	0	0	1	$\bar{1}$	0	0	0	+
Q_{24}	T_2	0	1	1	1	0	1	0	0	0	0	0	0	0	$\bar{1}$	1	$\bar{1}$	0	1	+
Q_{25}	T_2	1	0	0	0	0	0	0	0	0	0	0	0	1	0	0	0	0	0	+
Q_{26}	T_2	0	0	0	0	1	0	0	0	0	0	0	0	0	0	0	0	1	0	+
Q_{27}	T_2	0	0	0	0	0	0	0	0	1	0	0	1	0	0	0	0	0	0	+
Q_{28}	T_2	0	0	0	1	0	$\bar{1}$	1	$\bar{1}$	0	1	1	0	0	0	0	1	0	1	+
Q_{29}	T_2	0	1	$\bar{1}$	0	0	0	$\bar{1}$	1	0	1	1	0	0	1	1	0	0	0	+
Q_{30}	T_2	0	$\bar{1}$	1	$\bar{1}$	0	1	0	0	0	0	0	0	0	1	1	1	0	1	+
Q_{31}	T_2	0	0	0	0	$\bar{1}$	0	0	0	$\bar{1}$	0	0	$\bar{1}$	0	0	0	0	1	0	-
Q_{32}	T_2	$\bar{1}$	0	0	0	0	0	0	0	$\bar{1}$	0	0	1	$\bar{1}$	0	0	0	0	0	-
Q_{33}	T_2	$\bar{1}$	0	0	0	$\bar{1}$	0	0	0	0	0	0	0	1	0	0	0	$\bar{1}$	0	-
Q_{34}	T_2	0	1	1	0	0	0	0	0	0	0	0	0	0	1	$\bar{1}$	0	0	0	-
Q_{35}	T_2	0	0	0	1	0	1	0	0	0	0	0	0	0	0	0	$\bar{1}$	0	1	-
Q_{36}	T_2	0	0	0	0	0	0	1	1	0	1	$\bar{1}$	0	0	0	0	0	0	0	-

symmetry of the defect is T_d . Accordingly, the collective coordinates presented here form bases for the irreducible representations of the T_d as well as the O_h point groups. The T_d representations associated with various Q 's are indicated in Table II. The corresponding O_h representations

may be obtained from Table II with the substitutions, $A_1^- \rightarrow A_{1g}$, $A_1^+ \rightarrow A_{2u}$, $A_2^- \rightarrow A_{2g}$, $E^- \rightarrow E_g$, $E^+ \rightarrow E_u$, $T_1^- \rightarrow T_{1g}$, $T_1^+ \rightarrow T_{2u}$, $T_2^- \rightarrow T_{2g}$, and $T_2^+ \rightarrow T_{1u}$, where the plus or minus sign superscript refers to the rightmost column entry in the table.

¹P. J. Dean, C. H. Henry, and C. J. Frosch, Phys. Rev. **168**, 812 (1968).

²P. J. Dean and C. H. Henry, Phys. Rev. **176**, 928 (1968).

³B. Monemar and L. Samuelson, J. Lumin. **12-13**, 507 (1976); Phys. Rev. B **18**, 809 (1978).

⁴T. N. Morgan, Phys. Rev. Lett. **40**, 190 (1968).

⁵G. A. Baraff, E. O. Kane, and M. Schlüter, Phys. Rev. Lett. **47**, 601 (1981).

⁶P. J. Dean, Physica **178&118B**, 140 (1983).

⁷R. M. Feenstra, R. J. Hauenstein, and T. C. McGill, Phys. Rev. B **28**, 5793 (1983).

⁸K. Kunc and M. Balkanski, Phys. Rev. B **12**, 4346 (1975); K. Kunc, M. Balkanski, and M. A. Nusimovici, Phys. Status Solidi B **71**, 341 (1975); **72**, 229 (1975); **72**, 249 (1975).

⁹A. A. Maradudin, E. W. Montroll, G. H. Weiss, and I. P. Ipatova, in *Solid State Physics*, 2nd ed., edited by H. Ehrenreich, F. Seitz, and D. Turnbull (Academic, New York, 1971), Suppl. 3, Chap. 2.

¹⁰In *Solid State Physics*, Ref. 9, Chap. 8.

¹¹P. J. Dean, Phys. Rev. **157**, 655 (1967).

¹²K. K. Rebane, *Impurity Spectra of Solids* (Plenum, New York, 1970).

- ¹³G. Herzberg, *Molecular Spectra and Molecular Structure* (Van Nostrand and Reinhold, New York, 1966), Vol. III.
- ¹⁴R. M. Feenstra and T. C. McGill, *Phys. Rev. Lett.* **47**, 925 (1981).
- ¹⁵G. Baraff, E. O. Kane, and M. Schlüter, *Phys. Rev. B* **25**, 548 (1982).
- ¹⁶P. J. Dean, D. D. Manchon, Jr., and J. J. Hopfield, *Phys. Rev. Lett.* **25**, 1027 (1970).
- ¹⁷C. H. Henry, P. J. Dean, and J. D. Cuthbert, *Phys. Rev.* **166**, 754 (1968).
- ¹⁸The condition, $\text{Re}\lambda=0$, is an alternative to Eq. (9) for identifying resonant modes. (See *Solid State Physics*, Ref. 9, pp. 386ff.)
- ¹⁹T. N. Morgan, B. Welber, and R. N. Bhargava, *Phys. Rev.* **166**, 751 (1968).
- ²⁰C. H. Henry, P. J. Dean, D. G. Thomas, and J. J. Hopfield, in *Localized Excitations in Solids*, edited by R. F. Wallis (Plenum, New York, 1968), p. 267.
- ²¹T. N. Morgan, *Phys. Rev. Lett.* **49**, 173 (1982); *Physica* **117&118B**, 146 (1983).
- ²²P. J. Dean, M. S. Skolnick, Ch. Uihlein, and D. C. Herbert, *J. Phys. C* **16**, 2017 (1983).
- ²³T. N. Morgan, *Phys. Rev. B* **28**, 6107 (1983).

END

FILMED

1-86

DTIC